SEMI-EMPIRICAL STUDIES OF SOLAR SUPERGRANULATION AND RELATED PHENOMENA

by

PETER EDWARD WILLIAMS

Presented to the Faculty of the Graduate School of

The University of Texas at Arlington in Partial Fulfillment

of the Requirements

for the Degree of

DOCTOR OF PHILOSOPHY

THE UNIVERSITY OF TEXAS AT ARLINGTON

August 2008

I dedicate this PhD dissertation to my father, Gwilym David Williams, my mother, Margaret Elaine Williams and my brother, David Mark Williams.

ACKNOWLEDGEMENTS

The submission of this dissertation signifies an important benchmark in my career. It is a clear definition of exiting the academic process and entering a new phase of professional research. I wish to use this page to acknowledge those who have assisted my development into a professional scientist from the early stages of my undergraduate studies to the culmination of my PhD.

I wish to thank my academic advisor Dr. Manfred Cuntz who has been a very valuable mentor and has kept my focus and on track during my studies. My extreme gratitude goes to Dr. David Hathaway who provided me with a research program and, with Dr. Cuntz, secured funding. I am grateful to my PhD committee for all their comments on the dissertation and extend my gratuity to all the faculty, staff and students at UTA Physics whose assistance has been priceless. I'd like to further extend my gratitude to those with whom I have been involved prior to my PhD studies for providing me with a solid grounding to further my career.

I wish to thank my family who have provided continuous gravity not only during my current studies, but for all those prior. I further extend my gratitude to friends on both sides of the Atlantic, they are too numerous to name individually, but they should know exactly who they are

July 1, 2008

ABSTRACT

SEMI-EMPIRICAL STUDIES OF SOLAR SUPERGRANULATION
AND RELATED PHENOMENA

PETER EDWARD WILLIAMS, Ph.D.
The University of Texas at Arlington, 2008

Supervising Professor: Manfred Cuntz

In recent years, solar observations have moved from ground-based telescopes to observatories on Earth orbiting satellites, such as SOHO. They provide us with a clear and uninterrupted view of the solar disk. One instrument upon SOHO, the Michelson Doppler Imager (MDI), has proved fruitful in providing not only important information of the solar photosphere but, in combination with helioseismic methods, a method for probing the solar interior.

This dissertation discusses current investigations by myself and my collaborators into surface manifestations of convection phenomena, using Doppler velocity data from MDI and produced from computer simulations. The Doppler data reveal convection cells much larger than the granulation seen easily by optical telescopes. These supergranules' originate deeper within the convection layer than the granules and, like their smaller counterparts, are heavily influential in structuring the magnetic field and subsequently play an important role in controlling aspects of the solar activity cycle.

My work presented in this dissertation shows that the supergranulation pattern seems to rotate faster than the surface plasma. It has been suggested that the pattern is driven by wave-like phenomena, but instead we find the reason is a geometric effect with respect to the observer. We further find that supergranules are also responsible for

observed corrugation features on the solar surface, which previously had been interpreted as Rossby wave hills.

We extend our convection spectrum and Doppler map production simulations to include axisymmetric flows such as differential rotation, which contribute to the evolution of the velocity field. These models assist in understanding how such large-scale surface flows influence the surface motions of supergranules.

Lastly, I describe the construction of a numerical experiment to study the influence of a 'giant-cell' velocity field on the supergranule pattern. Such non-axisymmetric flows would further contribute to supergranule advection and the results of such experiments may assist in the observation of these hitherto elusive 'giant-cells'.

TABLE OF CONTENTS

LIST OF FIGURES

LIST OF TABLES

CHAPTER 1

INTRODUCTION

1.1 Introduction

The role and importance of the Sun and its current characteristics cannot be underestimated, no matter how obvious. Without this sole energy source, life would simply not have evolved. However, in recent years, more subtle properties of the Sun have become important, notably those that effect electrical devices and modes of communication on Earth. With satellite technology now common, it is prudent to understand the connection between the Sun and us and to what extent solar photospheric phenomena have terrestrial implications.

1.2 Lifecycle of the Sun

In the context of stellar evolution, the Sun is currently a relatively stable star [1]. But its past [2] has not been so stable, nor will its future [3], [4]. To place its current state in an overall evolutionary context, what follows is the assumed life-cycle of our star.

The Sun began its life as a cloud of gas and dust condensing toward a common point due to the effects of its own gravity [2]. The main core of the cloud continued collapsing while sporadic clumps formed at various distances away, forming what would become the planets. As the cloud core condensed further, more matter would gravitationally fall into it increasing the core mass [4]. The gravitational energy from in-falling mass is transferred to thermal kinetic energy emitting in microwave and infrared radiation as the dense cloud now becomes a protostar [4], [2]. The protostar continues to collapse as the internal pressure is not strong enough to support it. With increasing pressure, the temperature within the core of the protostar also increases [4]. With an increasing temperature, the internal particles (mainly hydrogen nuclei, i.e. protons, and electrons)

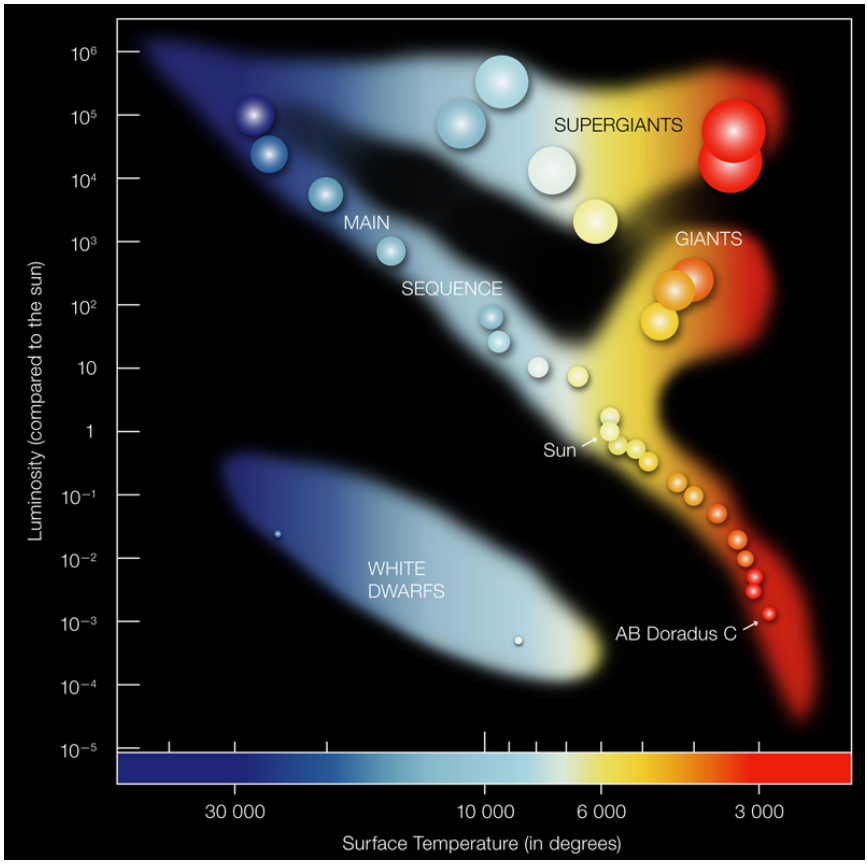

Figure 1.1. Hertzsprung-Russell diagram [7].

gain energy and at a certain temperature they become energetic enough to overcome their respective Coulomb barriers and fuse [3]. This nuclear fusion emits excess energy in the form of photons and this collective process in the stellar core provides the internal pressure necessary to halt the gravitational collapse [5]. The star, now in almost perfect hydrostatic equilibrium, is now called a main-sequence star due to its position on the Hertzsprung-Russell diagram (Fig. 1.1) that illustrates stellar distribution as functions of temperature (that is related to its visual color) and luminosity [6].

The main-sequence state of the Sun, after around 4 billion years of evolution, is how we find it and its overall stability is likely to last for sometime to come [8], [9]. In another 5 billion years or so, the hydrogen within the very center of the core will become exhausted. After another 1.5 billion years, the core will contract, as fusion no longer occurs within, while hydrogen still burns in a surrounding thick shell [4]. The

contracting core also means that the shell contracts, thus becoming hotter and burning hydrogen more rapidly. The extra energy released causes a sudden expansion of the solar surface at which the Sun becomes a red giant[4]. The core contracts, reaching the density of election-degeneracy and the temperature also increases, passing 10^8 K at which helium begins to fuse producing a violent 'helium flash' [4] which produces enough energy to expand the core away from it degenerate density. After another 0.1 billion years, the helium fuel in the core is exhausted and once again begins to shrink, also reducing the density of the material around it. This prompts helium in the shell around the core to ignite (producing another 'helium flash'), while hydrogen around that shell becomes hot enough to fuse [10]. The result is double-shell burning. The carbon-oxygen core contracts to electron-degenerate densities as no fusion reacts operate to sustain it [3]. The violent onsets of shell burning prompt high rates of mass-loss from the Sun's envelope [11]. What remains is a remnant core of a white dwarf star and the expanding, ejected envelope that forms a planetary nebula (PN) [4]. However, it has been suggested [9] that the solar PN will not be of the near-spherically symmetric shape of typical PNs, but will instead have a more bi-polar symmetry. This central remnant will subsequently cool and fade. The Sun will not end its life with a bang, but with a whimper.

1.3 Solar Properties and Structure

Table 1.1 lists some of the important properties of the Sun. To bring some of these parameters into an everyday context, 1.3 million Earths would fit inside the Sun, the core temperature is hotter than any Earth bound nuclear explosion and to produce the observed luminosity, the energy emitted corresponds to a mass loss of 4 million tons per second [6].

As can be seen in Fig. 1.2 the internal structure of the Sun can be divided into three sections: the core, the radiative zone and the convection zone [11]. It is within the core ($R < 0.2\ R_\odot$) that the conversion of hydrogen nuclei into helium nuclei is an ongoing process [5]. At temperatures within, the dominant process of nuclear fusion is

Table 1.1. Solar attributes [6]

Attribute	Value
Mean Distance from Earth	1.496×10^8 km
Mass	1.99×10^{30} kg
Equatorial diameter	1.39×10^6 km
Mean density	1.41 g cm^{-3}
Central density	150 g cm^{-3}
Surface gravity	273 m s^{-1} (27.9 g_E)
Luminosity	3.8×10^{26} W
Spectral Class	G2V
Effective (Photospheric) Temperature	5800 K
Central Temperature	$\sim 1.5 \times 10^7$ K

the proton-proton chain which combines four hydrogen nuclei to form a single helium nucleus [3].

This energy, in the form of photons, then begin its progress toward the solar surface where it is emitted as radiation. At the speed of light, this would seem a short process. However, considering the high density within the Sun, the photon only travels a very short distance before becoming absorbed by a particle [13]. Within the confines of the radiation zone ($0.2\ R_\odot < R < 0.7\ R_\odot$) the dominant energy transfer process is via radiation. A photon, traveling at the speed of light, undergoes many absorptions and emissions as it randomly walks outward from the core - an underlying radial radiative pressure provides the means of its general surface-bound trajectory [11]. The traversal of a single photon through this radiative zone is estimated at between 10,000 - 100,000 years [3]. From helioseismic measurements [14], it is found that the radiative zone largely rotates uniformly similar to a solid body . This is quite unlike the region directly above which is next for the photons journey, the convective zone ($R > 0.7\ R_\odot$). This region is found to rotate differentially with latitude and depth and with the solid body rotation of the underlying radiative zone [14], a tachocline is formed at their boundary defining a sharp shear in rotation rates. In the convection zone, the predominant method of

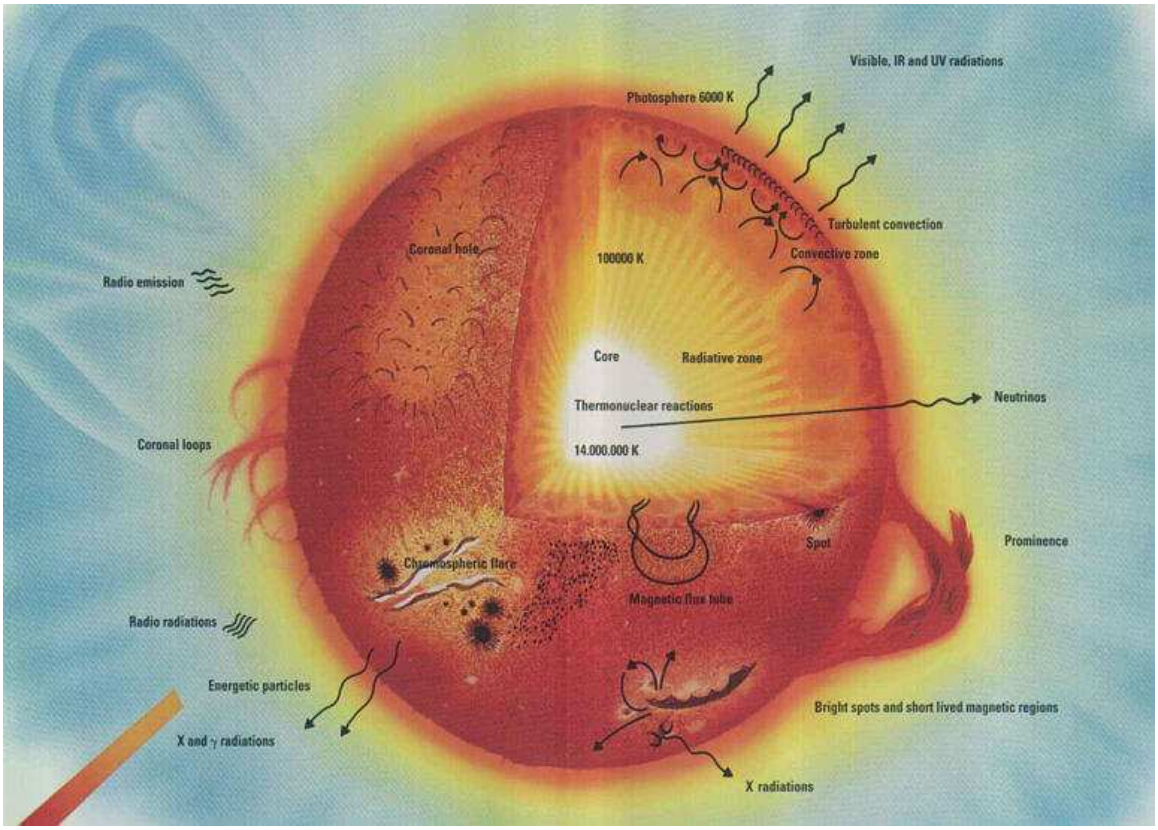

Figure 1.2. A schematic showing the internal structure of the Sun and the layers of its external atmosphere [12].

radiation transfer is convective in nature. This region, which is of primary importance for the presented studied, will be discussed in more detail in Section 1.4.

At what is the upper boundary of the convection zone, the density of material and, consequently, the opacity drops so that the medium once more becomes transparent to radiation [11], [15]. The energy is carried off to space by photons. It is these photons that we observe photosphere, defining the surface of the Sun. At this surface, the tops of the cells which carry energy outward are visible and are discussed in the next section. Also very prominent are features called sunspots (Fig. 1.3 (left)) that observationally appear dark due to their lower temperature ($\sim$ 4000 K) relative to the surrounding gas [15]. These are related to the Sun's global magnetic field which waxes and wanes over an 11-year cycle (Fig. 1.3 (right)), with the field switching polarity at the beginning of each [16], [17], [18]. The mechanism driving this cycle, coined the solar dynamo, which

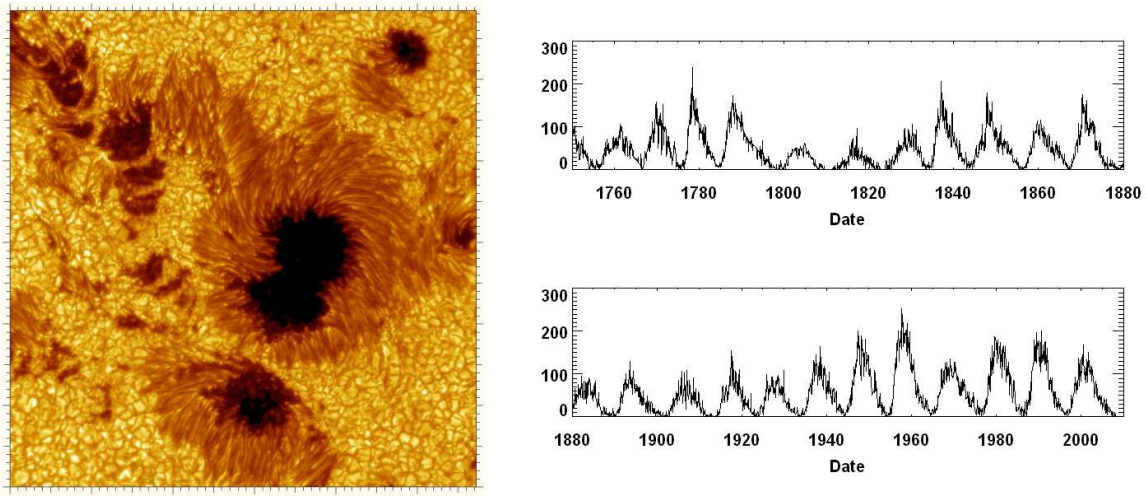

Figure 1.3. (Left) Picture of a sunspot showing the dark umbra area of strong magnetic field and the weaker field producing the lighter penumbra (Credit: Royal Swedish Academy of Sciences). (Right) Fluctuation of the number of sunspots visible on the solar disk over time, constituting the waxing and waning of the solar cycle (Credit: David Hathaway NASA MSFC).

incorporates the flows of differential rotation and localized convection to perpetuate and regenerate the magnetic fields, has undergone intensive research since its early models [19], [20] and have advanced to the stage where they are beginning to make predictions using existing solar cycle data about subsequent cycles [21], [22], [23].

In the chromosphere, the thin layer (about 10,000 km thick [3]) directly above the photosphere, magnetic features such as plages, spicules and filaments are visible (Fig. 1.4 left). A thin transition region [15] above the chromosphere is also notable for exhibiting very sharp negative density and positive temperature gradients (Fig. 1.4 right) which results in the chromospheric region only being seen optically when the photosphere is blocked, for example during a total solar eclipse.

In a similar nature to the chromosphere, the solar corona also requires optical observations be made during an eclipse [11]. However, unlike the chromosphere it has a very large spatial extent (Fig. 1.5) and its size varies depending at what point the Sun is at within its activity cycle [11]. The temperature gradient within the corona is less dramatic than within the transition zone, but is still firmly positive with temperatures

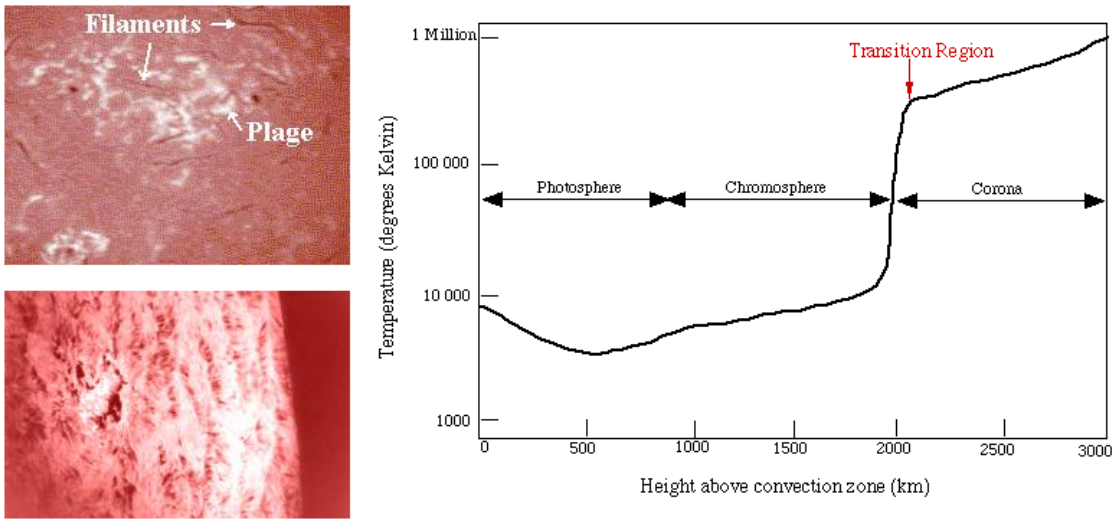

Figure 1.4. (Left) Chromospheric features observed in H-alpha [24], plages and filaments (top); spicules (bottom). (Right) Temperature profile above the solar photosphere. Note the sudden increase within the transition region that results in the high temperatures of the corona (Credit: M.B. Larsen).

reaching as high as 1–2 $\times$ 10^6 K even during quiet periods of the Sun's activity [15]. Coronal emission extends across the radiation spectrum due to the many process occurring within. One such interesting phenomenon are the coronal holes visible via X-ray emission which are caused by open field lines extend out into space as opposed to looping back towards the Sun[15].

These open field lines are considered to be the main driving mechanism of the solar wind [25] in which plasma particles are accelerated and driven out into the interplanetary reaches of the solar system and further [26]. The Earth is under constant bombardment by the solar wind, although the Earth's surface and immediate surroundings are protected by its magnetic field [27] which deflects the charged plasma particles. Such an interaction is visible to Earth observers as aurora [28] where some charged particles travel down the field lines to the Earth's polar regions and interact with the atmosphere.

With technology no longer being Earth-bound, it is of interest to understand the nature of the solar wind and the mechanisms driving it all the way back to the processes generating the systems of solar magnetic fields.

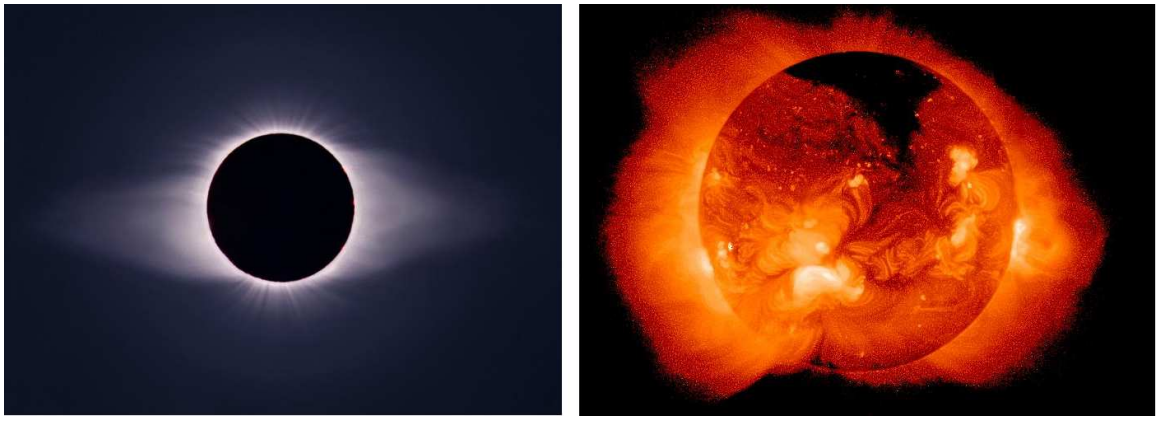

Figure 1.5. White-light (left - Credit: Fred Espenak) and X-ray (right - Credit: Yohkoh/SXT) images of the solar corona.

1.4 Solar Convection Zone

With temperatures decreasing radially outward through the radiative zone, at a certain radius the interior becomes cool enough to allow recombination of the nuclei and electron plasma to form atoms [11]. This drastically increases the opacity of material to a point where radiation is no longer an efficient process of energy transfer and convective processes take over.

The condition for convection is set by the Schwarzschild criterion [5] ,[15] that determines that for a rising gas element that is cooling adiabatically as it rises, if the ambient temperature gradient mean that the higher density surroundings cool faster than the gas element can cool, then the element will continue to remain buoyant and convective instability occurs [11].

The gas is heated from below by photons transporting energy from the underlying radiative zone and rises through the ambient medium. As it reaches the surface, energy is radiated away and the gas cools. On cooling, its density increases to that higher than the ambient surroundings and the gas falls [11]. So, in a similar manner to an 'air in a room analogy', a convection cycle is set up. However, in the Sun, many cyclic convection cells are set up and are not stable. Some may last for an hour, some for a few days [15].

Without being able to directly look into the convection zone, scales and behavior of convection cells can be interpreted from their surface manifestations [15]. It is found that convection cells can be segregated into disparate components, each having their own characteristics and are described in the Section 1.5.

1.5 Convection Components

Convection bells come in various shapes and sizes and past work has separated them into four distinct components [29], [15]. Starting with the smallest, these are granules, mesogranules, supergranules and giant cells. Typical parameters for each of these components, where known, are given in Table 1.2. In the following, each will be described and evidence for their existence critiqued.

Table 1.2. Typical values for convection cells viewed at the photosphere [15]

Convection Cell	Spatial Size	Lifetime	Horizontal Velocity
Granules	10^3 km	~ 1 hour	~ 1 km s^{-1}
Mesogranules	7×10^3 km	few hours	~ 500 m s^{-1}
Supergranules	30×10^3 km	$1 - 2$ days	$300 - 500$ m s^{-1}
Giant Cells	10^5 km	$\sim 2 - 3$ months	~ 10 m s^{-1}

1.5.1 Granules

A close up look at the solar photosphere reveals a pattern of cells (Fig. 1.6) that tends to evolve over time. These cells, called granules, are the manifestations of subsurface convection flows [30]. As seen in Fig. 1.6, the pattern is defined by the bright cells divided by dark lanes. The former is due to hot material rising to the surface due to convection and emitting radiation, while the latter is the downflow of the material once cooled. One can assume the dynamics as a radial upflow at the center of the cell, with a divergence horizontal flow towards its boundaries, becoming a downflow at the boundaries where flows from adjacent cells converge.

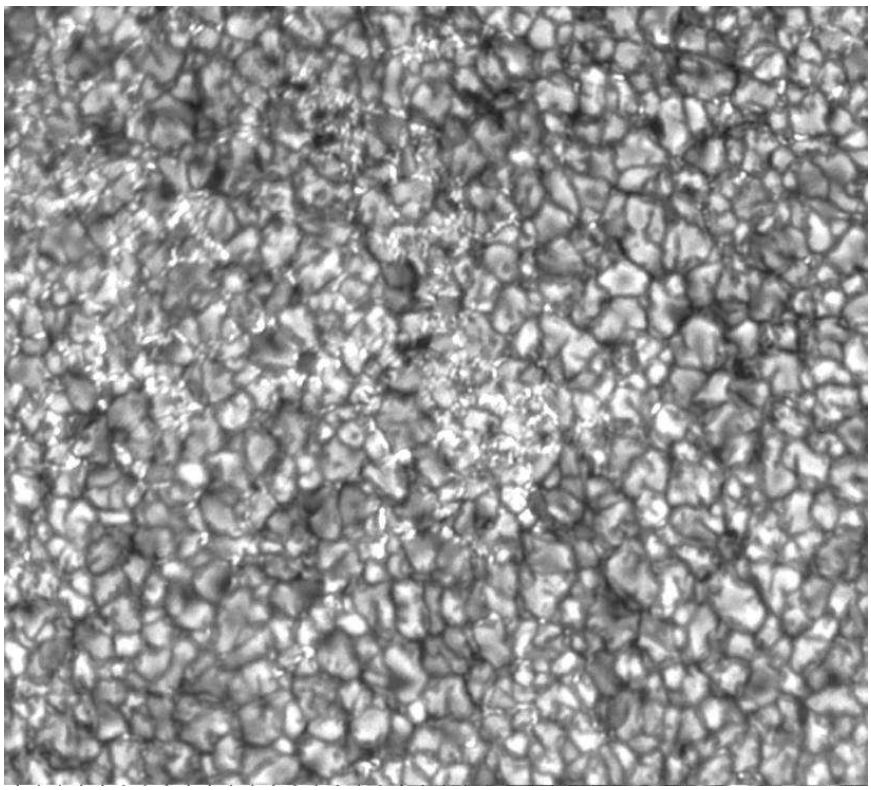

Figure 1.6. An image from the Swedish Vacuum Solar Telescope showing granulation on the solar photosphere (Courtesy: SVST).

Referring to Table 1.2 the surface cells have a spatial extent of around 1000 km and typically last for around an hour. However, as can be seen from Fig. 1.6, their range of spatial sizes is quite vast and, with better observations to resolve the thin dark lanes defining the cells, even smaller granules may exist.

Solar convection simulations ([32] and references therein) have been used to attempt to model the dynamics of the upper convection zone that produce the observed granulation. They constructed three-dimensional magnetohydrodynamic (MHD) code to analyze equations of mass conservation, momentum, energy and the induction equation. They were successful in producing results that realistically simulated surface granulation as well as other phenomena (Fig. 1.7), such as photospheric line profiles.

1.5.2 Mesogranules

The existence of mesogranules has remained a controversial topic since being first reported in 1981 [33]. The main supporting evidence is from horizontal divergence maps created by analyzing the surface motions of granules [34]. Granules that are embedded in larger scale flows can be tracked moving within such flows and their directions of propagations mapped. Should their relative motions be of a divergent nature (i.e. away from a common center), then it is likely that they are embedded in an underlying and larger divergent flow, possibly a convection cell. However, on analyzing a distribution of convection cells in a power spectrum (e.g. see [35]), no distinct component for mesogranulation seems to exist although power certainly exists spectral range theoretically inhabited by mesogranules. Additionally, models of the convection power spectrum suggest that only two components, granules and supergranules, are necessary to reproduce observations [35]. It is likely, therefore, that mesogranulation is not an independent, self-contained convection component and convection cells in this spatial range are most probably large granules or small supergranules.

1.5.3 Supergranules

Supergranules are not readily observed optically as the brightness of the granules overwhelms. They were originally observed by measuring the Doppler velocities of photospheric flows [36], a method that still remains a powerful observational tool. In a manner similar to those that observe mesogranules, divergence maps tracking granule advection can also betray the existence of supergranules [37]. However, unlike mesogranules, their existence is confirmed. What is still questionable, however, is the mechanism that drives this component. Their velocity characteristics are those expected of convective flows; similar to granules, they posses radial flows near the cell center, becoming a divergent horizontal flow towards the boundaries where downflows return material to below the surface. Previous ideas for their mechanisms invoke hydrogen and helium recombination that increase opacity [36]. More recent theories [38], however, suggest that the collective

downflows of smaller convection components contribute to the initiation of larger scale upflows. Realistic convection models [32] have tried to produce supergranules from such an amalgamation of granular downflows but, although convective features the size of supergranules are produced, an explicit supergranule convection component is not observed. This ongoing question contributes to the array of open issues still to be answered about supergranulation, some of which are discussed in Section 2.2.

1.5.4 Giant Cells

The largest component of solar convection are giant cells. Although proposed to exist since the late 1960s [39], hard observational evidence still does not exist, despite possible candidate signals being claimed [40]. Such cells are thought to span a vast area of the solar surface [41], although shearing within the convection zone might deform them into latitudinal thin but longitudinally long features [40]. Other methods may be used to obtain signals for these elusive cells, some of which are described in Chapter 7.

1.6 Dissertation Outline

The focus of this dissertation is the study and understanding of particular characteristics of supergranulation. These convection cells are described further in Chapter 2 and some of the open questions concerning their nature are raised. The observational data used in these studies are derived from those collected by the Michelson Doppler Imager (MDI) aboard the Solar and Heliospheric Orbiter (SOHO). The MDI instrument is discussed in detail in Chapter 3. The process of reducing the raw data from MDI into such that contains only that pertaining to non-axisymmetric flows due to convection is described in Chapter 4. Also within this section is described a data simulation that creates realistic data using coefficients derived from synthetic data and mapped onto the spherical harmonics.

The next four chapters are dedicated to the investigations and results achieved from analyzing real and synthetic MDI data involving myself and collaborations, in which I

was an active member. Chapter 5 investigates supergranule Doppler pattern rotation relative to the underlying plasma. Chapter 6 investigates the identity of hills discovered on the solar limb attributed to Rossby wave phenomena and questions whether the real cause is overshooting of supergranule convective upflows. Chapter 7 describes improvements made to the data simulation that include the implementation of advection of the convection pattern due to a realistic differential rotation profile. Chapter 8 moves away from supergranulation to their larger relatives, the giant cells and adopts methods that may contribute to their definite discovery. A concluding chapter then summarizes the work in Chapter 9.

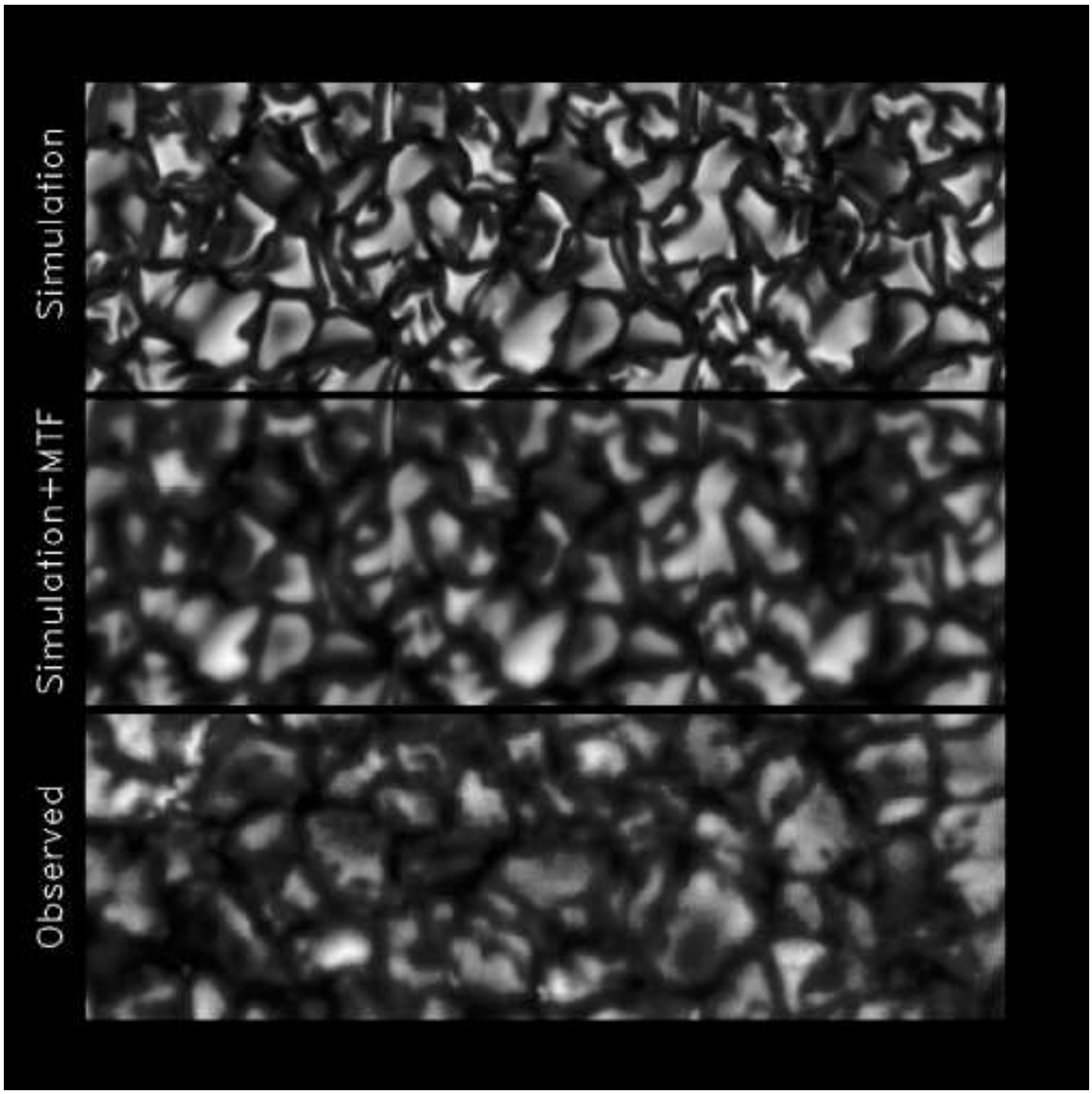

Figure 1.7. Comparison of a simulated to an observed granulation pattern [31]. The top panel shows a composite granulation pattern produced from images separated by 1 minute. The middle panel shows the same images but convolved with an Airy plus exponential point spread function. The bottom panel shows a white-light image taken from the La Palma telescope.

CHAPTER 2

SOLAR SUPERGRANULATION

Although Section 1.5.3 noted that the driving mechanism behind supergranulation is still not known for sure, many characteristics of supergranules have been discovered and will be discussed in the following sections. There are, however, a number of outstanding issues, some of which will be detailed toward the end of this chapter.

2.1 Characteristics of Supergranules

Recapping some of the basic characteristics, supergranule cells observed at the photosphere are typically 30,000 km across, last for around 1 day and their horizontal velocities in the range of 300 m s^{-1} are nearly 10 times that of their radial velocities.

2.1.1 Supergranule Shape

Supergranules are similar to granules in shape, although their boundaries may not be as structured as the latter. Evidence for this has been shown from velocity contour maps at the solar disk center [42]. Fig. 2.1 shows such a contour map. Near the center of the supergranule, the flows are predominantly blue-shifted, i.e. an outflow, becoming zero then red-shifted near its boundary which distinguishes inflow of material at the supergranule boundary. The discrepancy with the more regular boundaries of granules is highlighted in the disconnect of the red-shifted velocities.

The border of this supergranule as seen from a chromospheric network observation is overlaid, outlining the congregation of magnetic field lines at the boundaries of the supergranule and those adjacent to it. This chromospheric network is well observed via H_α emission and at the Calcium-K line as a seemingly organized pattern across the solar

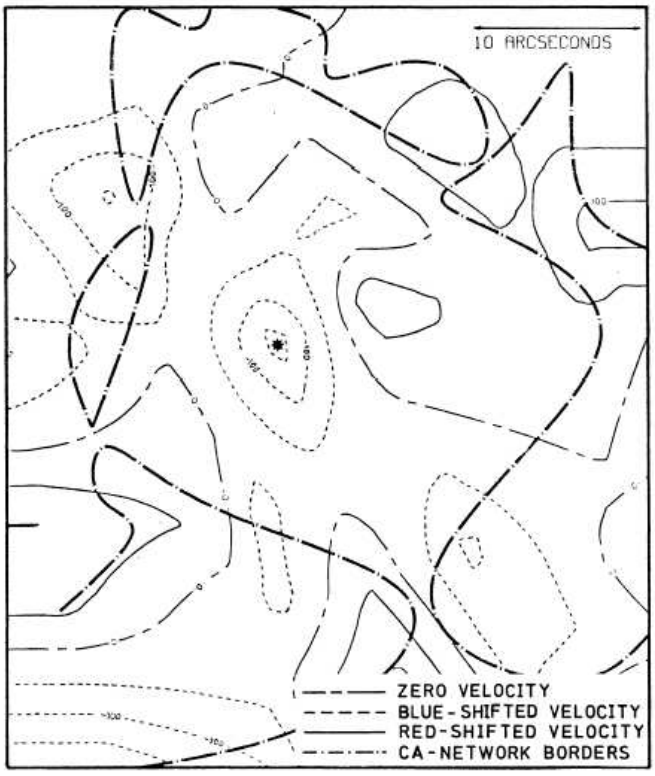

Figure 2.1. Velocity contour map of a supergranule observed at disk center [42].

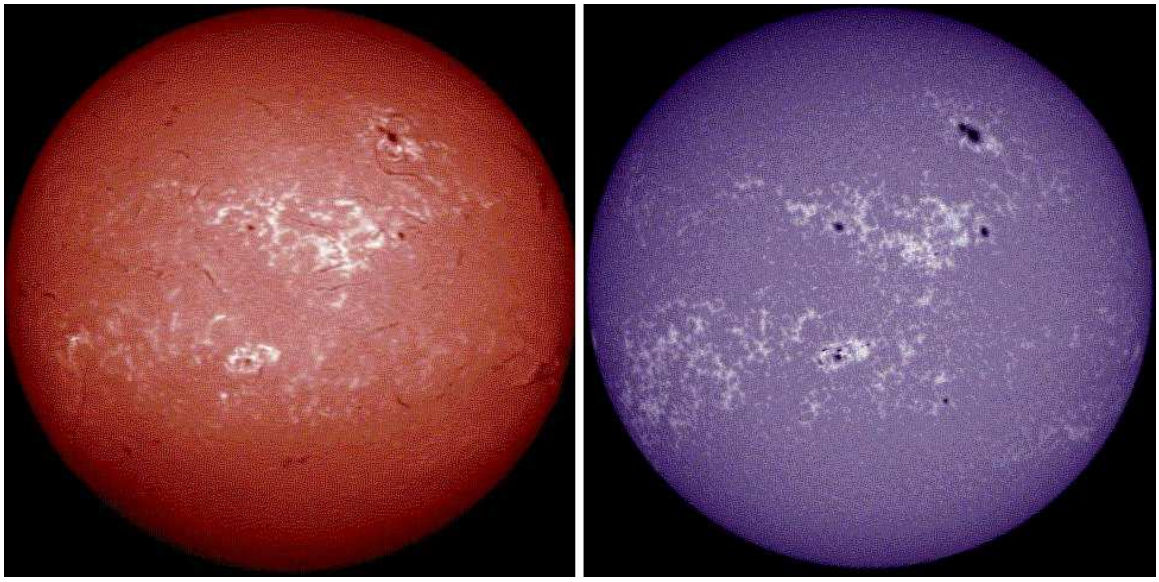

Figure 2.2. Images of the chromospheric network [24] in H-alpha (left) and CaK (right) emission.

disc (Fig. 2.2). This chromospheric emission is the result of an interaction with local magnetic fields and is discussed in Section 2.1.3 below.

2.1.2 Effect of Rotation on Supergranules

As the surface motions of convection cells lie on the surface of a rotating frame, then they are liable to be influenced by Coriolis forces. However, the influence of the Coriolis force is not equal for all flows and depends on the ratio of the inertial to Coriolis forces in the form of the Rossby number

$$Ro = \frac{u}{2\Omega l} \tag{2.1}$$

where u is the velocity of the motion, Ω is the rotation rate and l is a length scale for the flow. For a large Rossby number, the rotational influence can be neglected. However, such influences must be considered for small Rossby numbers.

In the context of surface convection flows, Ω is dependent on the location of the flow on the solar surface due to the Sun's latitudinal dependent differential rotation, whereas u and l depend on the flow itself describing horizontal flow velocity from the cell center and the size of the cell, respectively. By using a typical solar rotation rate of $\Omega \sim 3 \times 10^{-6}$ s^{-1}, considering the spatial extremes of convection (refer to TABLE), for granules ($u \sim 1000$ m s^{-1}, $l \sim 10^6$ m) we get $Ro \sim 500$ so Coriolis influences are negligible, while for giant cells ($u \sim 10$ m s^{-1}, $l \sim 10^8$ m) we get $Ro \sim 0.05$ so Coriolis influences must be taken into consideration. However, when studying supergranules ($u \sim 300$ m s^{-1}, $l \sim 3 \times 10^7$ m) we get $Ro \sim 5$ the criterion for rotational influence is on the borderline. A larger, slower flow would produce rotational influenced flows, while smaller faster flows would have no such influence.

Although initially calculating the rotational influence as small, Stix [15] continues to report spectroscopic evidence [43] of the Coriolis force affecting the direction of the cellular flow. Hathaway [44] showed that Coriolis effects can indeed influence the direction of supergranule type flows near their updrafts and downdrafts. He also showed that the

divergent flows from the center of a convection cell, modeled as a pattern of hexagons, were diverted clockwise for upflows and counter-clockwise for downflows.

2.1.3 Supergranule Interaction with the Local Magnetic Field

As magnetic fields are embedded throughout the convection zone, being generated by the dynamics of this region, the flows within will tend to distort the field lines. For example, any rotation of a rising packet of gas will tend to lift and twist the field lines. It is indeed this process that plays a role in the magnetic dynamos [45] discussed in Section 1.3.

Such processes are carried out within supergranule flows with field lines being brought to the surface. At the surface, the prodominant horizontal flow toward the edges of the supergranule cell carry field lines with it, so that they tend to congregate at supergranule boundaries [15]. It is this distribution of the field that interacts with chromospheric material to produce the outline of the supergranule boundaries that is observed in images of the chromospheric network (Fig. 2.2) [11].

Around the boundary, especially at boundary vertices of more than two cells [46], concentrations of magnetic field lines may combine to form flux tubes. These tube-like fields are confined within the down flow between convection cells, but spread out above the solar surface where the density of material is not high enough to confine them into a tightly bound configuration. Below the surface where they are confined, they may interact with the surrounding material and various types of oscillations may occur within the flux tubes, an area of physics which has attracted much investigation [47], [48].

Although these magnetic phenomena are on the whole tied with the global magnetic field produced by a global 11-year cycle dynamo, and the active regions resulting from them, noteworthy magnetic activity still exists during quiet phases of the cycle when no magnetic active regions are present. It follows, therefore, that a different mechanism is responsible for these 'quiet Sun' magnetic phenomena. Indeed, it has been suggested [49] that a more localized process is responsible for these fields, associated with granular and

supergranular flows. As magnetic fields generally have diffusive timescales compared to those for magnetic advection, such local dynamo models have to operate in regimes of vanishing magnetic diffusivity, something which is described in fast dynamo models [50]. Further numerical models [32], [51] are beginning to increase the influence of magnetic fields in their simulation domain and may assist in understanding what role such fields play in the production of a separate supergranule component to solar convection.

2.2 Outstanding Questions Concerning Supergranulation

Although there is a wealth of information about the nature of supergranulation and related phenomena, many questions are still unanswered and solving these issues may prove to be valuable pieces contributing to a global understanding of the Sun [29].

Some open topics, although not discussed in this dissertation, are, for example, at what point in the spatial size of a convection cell does rotation, and the subsequent Coriolis force, become important [44]. Is it tied solely to size or is it dependent on the nature of the convection component itself?

Following on from this, for what types of convection cells do local dynamos operate [45] and what influence, if any, do they have on the global field during the quiet periods of the solar cycle. Is there a link between local dynamos [49] and the α-effect [52] that plays a large role in global dynamo models?

Although these remain open and interesting topics, my research work as described in this dissertation pursues and answers other questions regarding supergranulation. These are briefly described in the following.

Observations of the supergranule pattern have shown that the pattern seems to rotate faster than the plasma within which the supergranules are embedded [53]. A number of explanations could be put forward. As there exists a radial differential profile throughout the convection zone [14], maybe the material at the depth within which the supergranules are anchored is rotating faster than the surface plasma so that the supergranules are therefore advected faster in a similar manner as magnetic features

seem to exhibit varying rotation rates depending on the depth at which they are anchored within the convection zone [54]. There could be underlying wave phenomena carrying the supergranules faster than the rotation rate [55]. As the observed images are actually two-dimensional characterizations of a three-dimensional flow-field, then this superrotation may well be the result of a geometrical projection effect. This topic we raised in Chapter 5 and perform studies into the superrotation and its causes.

The shape of the Sun has raised many questions beginning with the fact that it diverges from a perfectly spherically symmetric object with an oblate quality, exhibiting equatorial bulging and polar flattening, due to its rotational nature [56]. It has been the intent of observations to then study other, smaller scale, surface perturbations and understand the mechanisms causing them [57]. One such expected perturbation is due to convective overshooting at the surface. The coming and going of convection cells should also produce evolving undulation of the solar surface. Other phenomena, such as those produced by waves [58], may also have an effect on the solar shape on the order of supergranule spatial scales. This observation is described in Chapter 6 and where I then study the causes of these surface features.

Helioseismology has provided evidence that a differential rotation profile occurs not only at the solar surface but also extends throughout the convection zone [14]. Assuming that convection cells of different spatial sizes as viewed at the surface are anchored at different depths beneath the surface [54], it may be concluded that these cells should rotate at different rates according to the radial rotation profile. I analyze this hypothesis in Chapter 7 by means of comparing simulated data to real data. I make further data comparisons, described further in the chapter, to study evolutionary lifetimes of different sized convection cells.

It is understood that granulation cells are advected by the supergranule flows in which they sit [36]. However, is there an extra step in which supergranules themselves sit in the flows of an even larger component of convection, i.e. giant cells, and are themselves advected? Some studies contributing to the search for giant cells [39], [40] are described

in Chapter 8. I describe the construction of a numerical experiment I performed to simulate flow fields to attempt to produce supergranule advection by giant cells. Similar dynamics may be responsible for observed signals hitherto suggested to be derive from a wave-like component of supergranulation [59].

CHAPTER 3

THE MICHELSON DOPPLER IMAGER

3.1 Introduction

Until the launch of the Uhuru satellite in 1970, all astronomical observations were conducted from ground based instruments, including the important solar observations that form the basis for latter studies such as those noted in this dissertation. Among these are the Doppler velocity observations of Leighton, Noyes & Simon [36] at the Mount Wilson Observatory that provided the first measurements of the supergranule velocity field. Any observations require sufficient and continuous integration time (normally many days) to improve the integrity of the data, e.g. noise reduction, but this is hampered by the limited time that objects appear above the horizon. In the case of the Sun, observations can only , for obvious reasons, be made in the daytime. The daylight hours may be extended by moving the observation location nearer to the Earth's poles where observations may be made through consecutive months of the local summer. Indeed, successful programs have been carried out in Antarctica, for instance those carried out by Fossat et al. [60], right through to recent projects such as CASTEL [61]. Although an improvement on earlier observation sites, integration times made within the Antarctic Circle are still temporally limited as well as the highly remote nature of the location itself. Thus a method had to be developed to allow continuous ground-based observations of the Sun. The Global Oscillation Network Group (GONG) [62] was set up to meet this objective.

GONG is an international community-based helioseismology project which became operational in 1995 and allows near-continuous observations of the Sun. It operates a network of six observing stations around the globe, from which data is collected and combined to construct a constant solar record. The data is analyzed to produce a wide

range of results and information about the Sun, such as solar oscillations and surface convection manifestations (for example, see [63], [64], [65], [66]).

However, one remaining hindrance to the data quality from GONG has been the Earth's atmosphere. As the global observation sites are all ground based, any observations traverse the turbulent atmosphere thus making the data more susceptible to noise. Thus in 1987, the Solar and Heliospheric Observatory (SOHO) was proposed to carry a number of instruments to carry out a large variety of observations such as the solar corona and solar oscillations.

In December 1995, the SOHO satellite [67] was launched and parked in a stable orbit at the L1 Lagrangian point between the Earth and Sun. The instruments aboard were thus provided with uninterrupted observations of the solar disk without the constraints presented by the terrestrial atmosphere. One such instrument is the Michelson Doppler Imager (MDI) [68] that was built to probe the solar interior by studying the photospheric manifestations of internal oscillations.

3.2 Spectral Line Selection

MDI makes observations of the absorption spectral line of neutral nickel (Ni I) at 6767.77 Å (Fig. 3.1), which is produced just below the solar photosphere due to photon absorption by an excited state of Ni I, and has already been used effectively by GONG. The line fits a set of selection criteria for Doppler velocity measurements [66]. Firstly, it is well isolated from other spectral features, meaning that any features seen can be solely attributed to that line without being contaminated by its spectral neighbors. It should be insensitive to magnetic fields so that Doppler velocities can still be measured to high accuracy across the face of the disk over which the field strength may vary. However, magnetic field measurements are still possible with MDI by observing the circularly polarized components of the incoming light. There should be a weak dependence of the line observation on the viewing angle from solar center to limb (the edge of the solar disk). Although limb darkening is clearly seen optically due to the light passing through

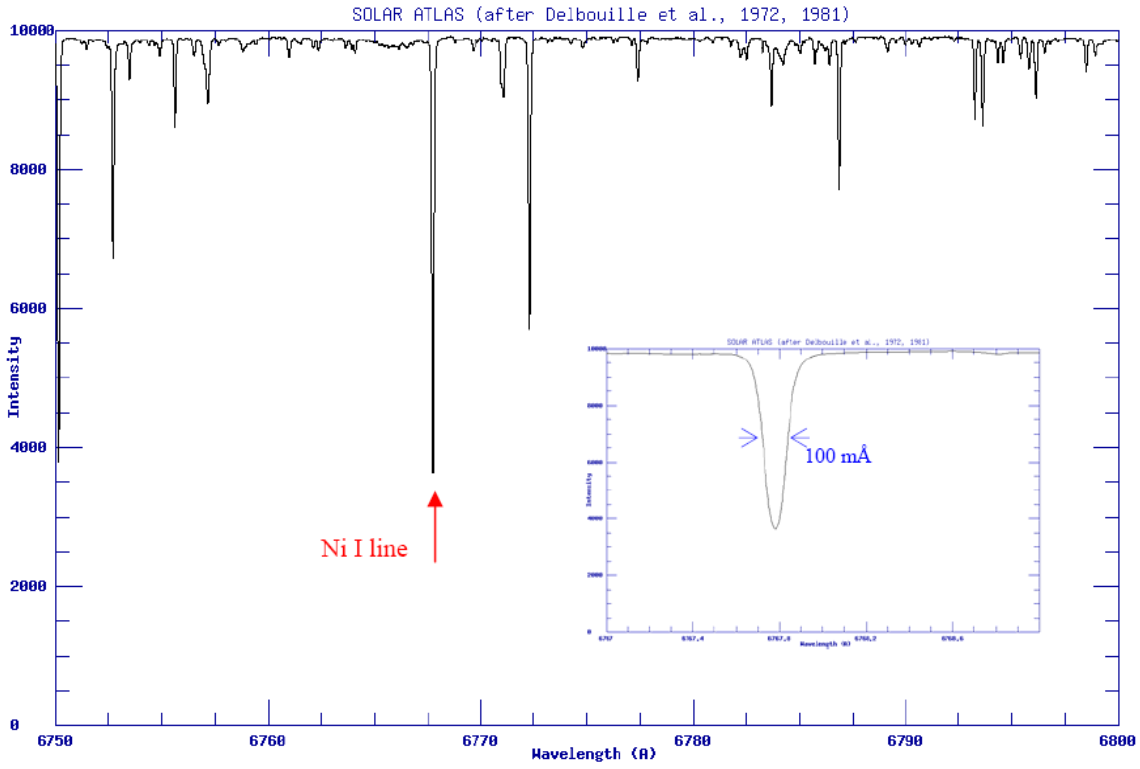

Figure 3.1. Solar spectrum [69] between 6750 Å and 6800 Å showing the position of the 6767.77 Å Ni I line observed by MDI. The inset shows a close up of the line and its corresponding width due to Doppler broadening (wavelength ranges between 6767 Å and 6769 Å).

more of the solar atmosphere at the limb compared to light emitted at the center, the depth of the absorption line should be relatively constant [68].

3.3 Instrument Design

The MDI instrument [68] was built by a collaboration of the Solar Oscillations Investigation Group (SOI) at Stanford University and the Lockheed Palo Alto Research Laboratory. There are two major packages within MDI: the optics package which contains the components to observe the solar disk within a particular wavelength range around the Ni I line and collect the data by CCD, and the electronics package which controls the optical system and also manages the data communications between the instrument and the Earth based center of operations. A schematic of MDI is shown in Fig. 3.2 and

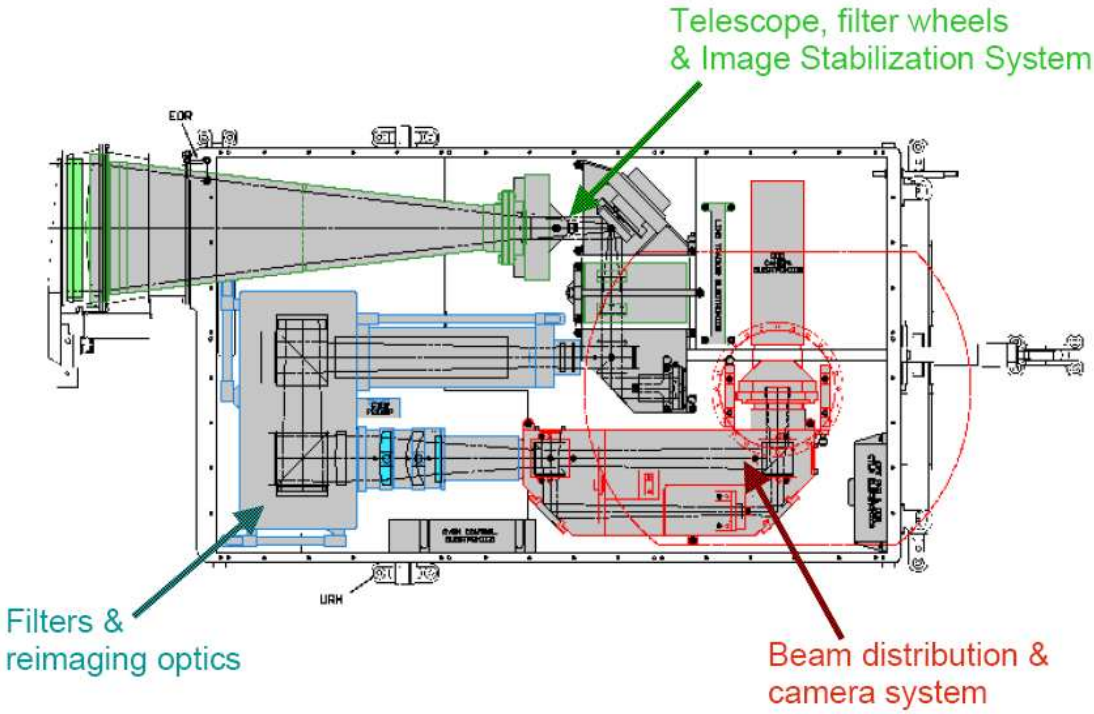

Figure 3.2. Schematic of the MDI instrument showing the three major parts of the optics package.

the optical layout of the optics package is displayed in Fig. 3.3. It is shown that three sections comprise the optics: the telescope, imaging system and polarization selectors (green), the filters and reimaging optics (blue) and the beam distribution and camera system (red).

3.3.1 The Telescope, Imaging Stabilization and Polarization

Light from the Sun enters the instrument via an entrance window which, like all the other optics-vacuum interfaces, is coated with an anti-reflection material which transmits with very high efficiency around 6768 Å, while reflecting other wavelengths. Thus, any light transmitted through the optics is essentially distributed immediately around the Ni I line. A 50 Å bandpass filter further reduces the transmission range, blocking infrared radiation to which the CCD is very sensitive. The telescope is a refractor with an objective lens, limited by a 12.5 cm diameter circular aperture stop, and a secondary enlarging lens with an effective focal length of 1867 cm. The image is folded by an image

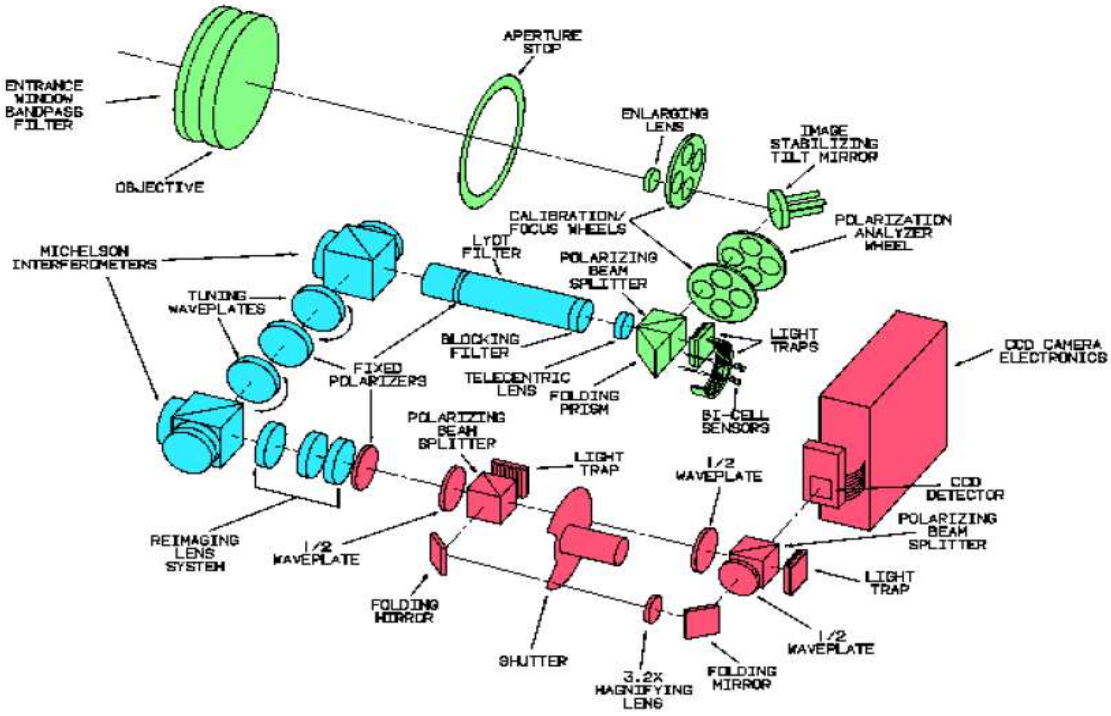

Figure 3.3. Optical layout of MDI showing the path of the beam through the instrument [68].

stabilizing mirror towards the polarization optics. The polarization analyzer wheel can select between right- and left-circularly polarized and horizontally and vertically ('p-' and 's-' respectively) polarized light. These components are converted into p- and s-components after which a polarizing beam splitter sends the p-component to a bi-cell detector, which is electronically linked to the image stabilization mirror and the complete circuit behaves like a feedback loop to analyze the light and adjust the mirror accordingly. This mechanism keeps the image centralized on the optics and also reduces any instrumental jitter that may occur. Meanwhile, the s- component is directed through the instrument into the filter system and onward through to the detector.

3.3.2 The Filter and Imaging System

The s-polarized light sent from the beam splitter first enters a telecentric lens which collimates the beam, focusing it to infinity. The transmission wavelength selection is then performed by a series of fixed and tunable filters (Fig. 3.4). The fixed filters

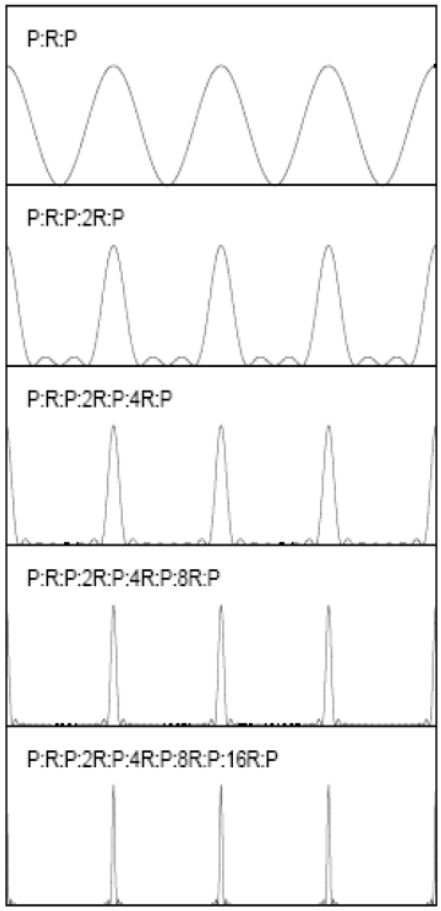

Figure 3.4. Periodic transmission profiles of a Lyot filter [70]. Each profile corresponds to one extra crystal added to the filter, being two times the thickness of the one preceding it.

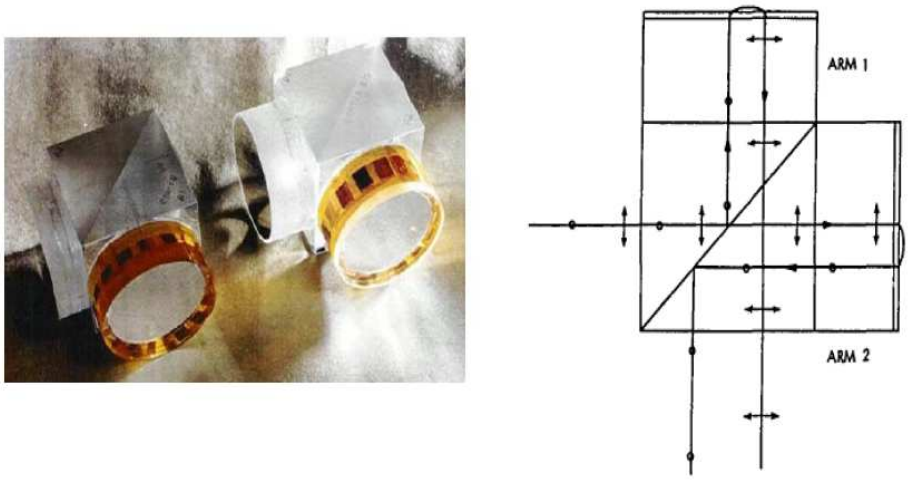

Figure 3.5. Photograph and schematic of a solid Michelson interferometer [71]. The two exit beams have been split in this diagram to illustrate their respective time delay.

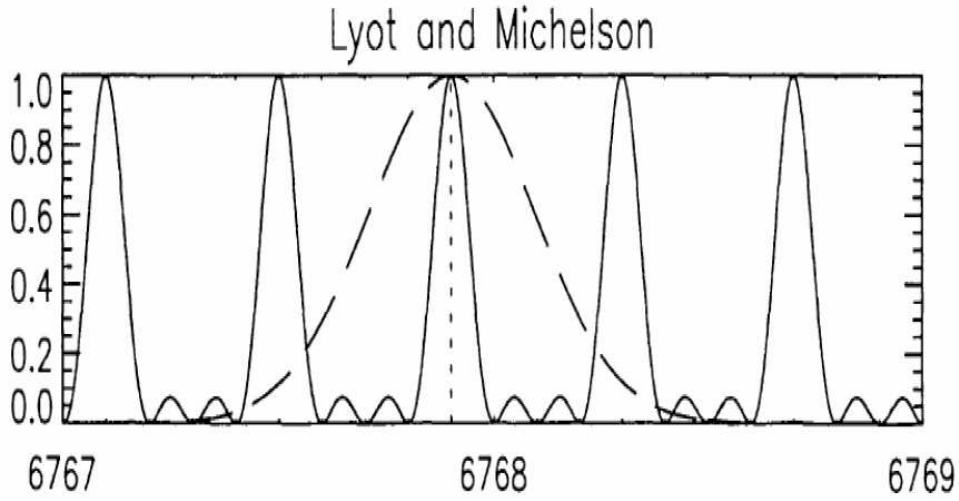

Figure 3.6. Diagram showing the transmission profiles of the filter optics within MDI [68]. The solid line shows the periodic profile due to the Michelsons, centered on the rest wavelength of Ni I (dotted line). The dashed line corresponds to the profile of the Lyot filter.

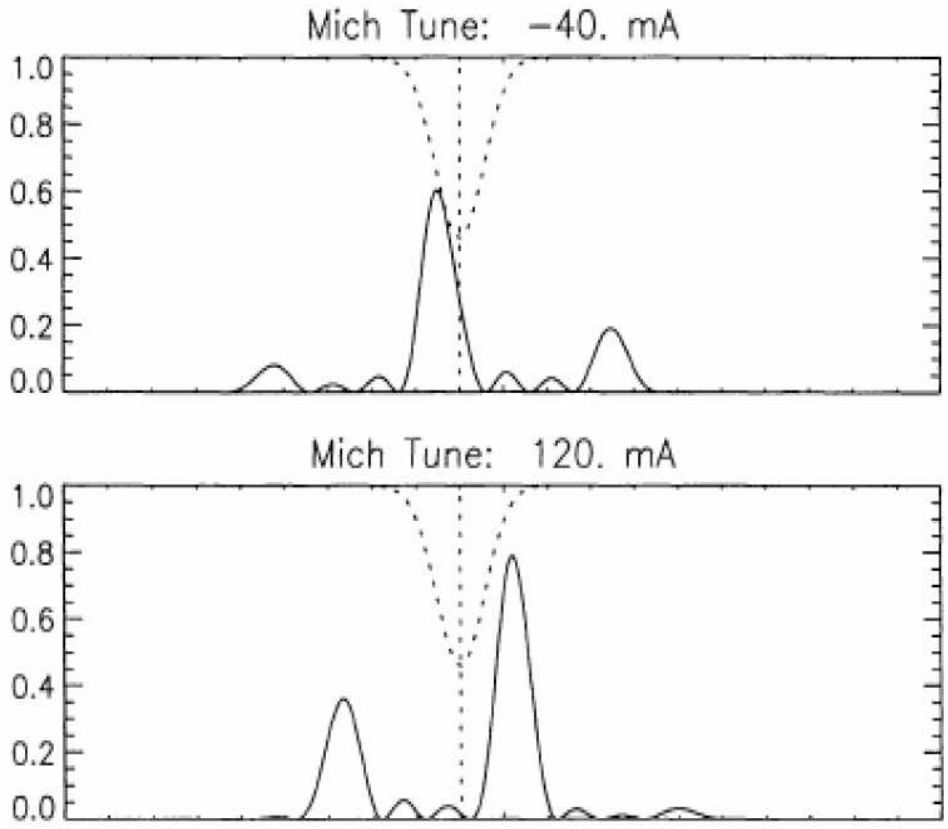

Figure 3.7. The Michelsons can be tuned so that the transmission profile can be centered at 8 m steps around the Ni I rest wavelength over a 377 Å range [68].

include an 8 Å bandwidth blocking entrance filter to a birefringent Lyot filter. The beam then passes through two solid Michelson interferometers (Fig. 3.5) which can be tuned with rotating waveplates which select the center of the transmission profile. A final set of re-imaging lenses focus the beam onto the detector. The interferometer system produces periodic transmission profiles 377 mÅ apart centered on the Ni I line with a transmission bandwidth of 94 mÅ. The Lyot filter is also centered on the Ni I line with a bandwidth of 465 mÅ. This selects the centroid Michelson interference transmission peak while quenching the others. Further, a blocking filter at the entrance to the Lyot filter with a bandwith of 8 Å permits the central peaks from the other two filter systems, while suppressing the other interference profiles produced by the Lyot. A diagram of the transmission profile is shown in Fig. 3.6. The central peak (solid line) is the by tuned Michelson interferometers to the 6767.77 Å Ni I line (dotted), while the other peaks either side are removed by the Lyot filter (dashed line). Using the tunability of the optics system, the input beam can be sampled at various wavelengths. The peak of the transmission profile can be positioned around the Ni I line in steps of 8 mÅ over a range of 377 mÅ (examples of profile positioning are shown in Fig. 3.7). The intensity of the output beam over selected wavelengths can determine the position and the depth of the absorption line, the intensity increasing from a minimum as the transmission profile is moved from the absorption line center toward the wings. In MDI, line intensities are measured at five fixed wavelengths separated by 75 mÅ, with the central profile positioned at 6767.77 mÅ. These produce a set of five filtergrams, F0 through F5, corresponding to the set of five wavelengths. F0 is at 6767.77 mÅ, the rest wavelength of Ni I, F1 and F4 correspond, respectively, to the blue and red wings of the line profile which F2 and F3 correspond, respectively, to the blue and red core of the profile. Each filtergram is passed through re-imaging optics which focuses the image onto the plane of the detector, before entering the beam distribution and camera system.

3.3.3 Beam Distribution and Camera System

A polarizer and a halfwave plate convert the beam into two orthogonal linearly polarized components which are split by a polarizing beam splitter and distributed into two paths. This selects the resolution of the image to be detected. One path corresponds to normal (1×) resolution, whereas the other path subjects the image to 3.2× magnification using a Barlow lens. The selectivity is selected using a simple shutter which allows the beam to traverse the path of the required resolution while blocking the other beam. A halfwave plate then readjusts the polarization of the selected beam before passing it through another beam splitter and towards the detector. The detector itself is a front-illuminated CCD with a 1024×1024 array of 21 m pixels. Further information on this part of MDI is given by Scherrer et al. [68].

3.4 Data Collection and Processing

Each filtergram is detected with a cadence of 3 seconds, meaning that a set of five is collected in 15 seconds [68]. Two or four sets are collected per minute corresponding to 30 or 60 second programs respectively, dependent on what other concurrent observing programs are underway. The filtergrams are combined onboard MDI by an image processor which reduces the amount of data to be downloaded to the command center on Earth. Certain combinations produce certain secondary observables, such as the line of sight Doppler velocity, line depth, continuum intensity and Zeeman splitting.

3.4.1 Doppler Velocity Calculations

The main observable constructed from combining the filtergrams is the line of sight Doppler velocity. This is estimated from a ratio of differences of the F_1 through F_4 filtergrams and given a value [68],

$$\alpha = \frac{F_1 + F_2 - F_3 - F_4}{F_1 - F_3}, \qquad \text{if numerator } > 0 \tag{3.1}$$

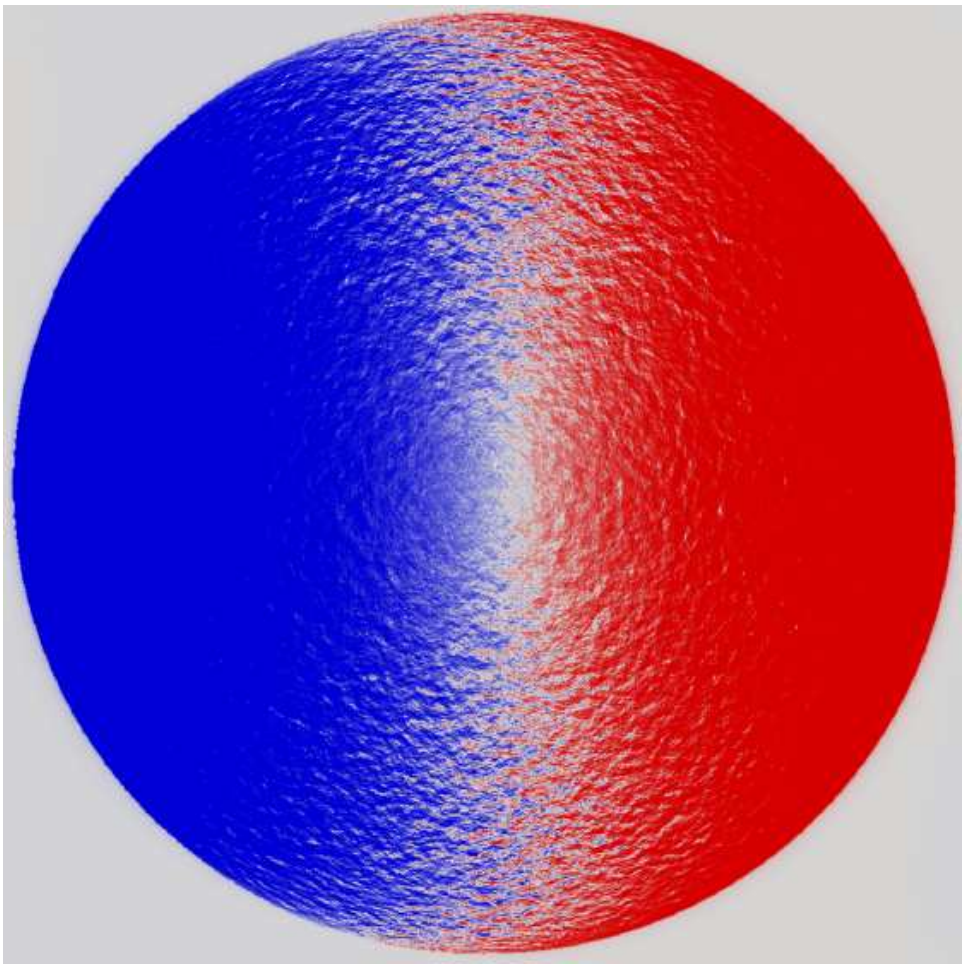

Figure 3.8. A raw Doppler image illustrating photospheric line-of-sight velocities. The dominant velocity component is that of rotation. The left side of the image is inherently blue (approaching velocities) whilst the right side is red (receding velocities).

$$\alpha = \frac{F_1 + F_2 - F_3 - F_4}{F_4 - F_2}, \qquad \text{if numerator } \leq 0 \tag{3.2}$$

If the numerator is greater than zero, then the filtergrams show higher intensities at the blue side (F_1 and F_2) of the Ni I rest wavelength than at the red side (F_3 and F_4), corresponding to a deeper absorption line at the red side of the Ni I rest line. This corresponds to a redshift of the absorption line with the absorbing material and the observer moving apart. The inverse is true if the numerator is less than or equal to zero; there is a blueshift of the absorption line. The Doppler velocity is calculated by an image processor from using a stored lookup table constructed from simulations before

launch. Negative corresponds to negative velocities (material moving toward observer) and positive to positive velocities (material moving away from observer). Errors in this measurement may arise from measuring profiles of widths different to those used to construct the lookup table, by mistuning of the Michelsons, mis-centering of the Lyot profile and systematic errors due to the variability of the solar line. A raw Doppler image is shown in Fig. 3.8 and it can be clearly seen that rotation is the largest component. The raw Doppler images are subsequently reduced by subtracting velocity component features, such as solar rotation and oscillations, which are described later in Section 4.2.

3.4.2 Other Observables of MDI

The filtergrams can be combined in other ways to derive other observables such as the continuum and the line depth. Magnetic properties can be derived by constructing a longitudinal magnetogram of the solar disk. Doppler shift data is collected from the right and left circularly polarized components of the input beam and the difference between the two measures the Zeeman splitting, which relates to the magnetic flux density. Further observables are derived after downloading the data to Earth and via subsequent computer processing.

3.4.3 Helioseismology Using MDI Data

The Sun is found to oscillate over a wide variety of modes and frequencies. Past work with GONG [62] has been furthered by studies using MDI into the nature of these oscillations. Acoustic (p) modes are predominant in the convection zone and are driven by pressure differences within the region, whereas gravity (g) modes are confined deeper within the interior and have gravity as their restoring force. Although g-modes are difficult to observe due to their spatial confinement, p-modes are easier (although still difficult) to detect as they interact with the solar surface (Fig. 3.9).

The surface manifestations of p-modes as the waves are reflected toward the interior can be observed over time with spatial and temporal Fourier transforms of the time series

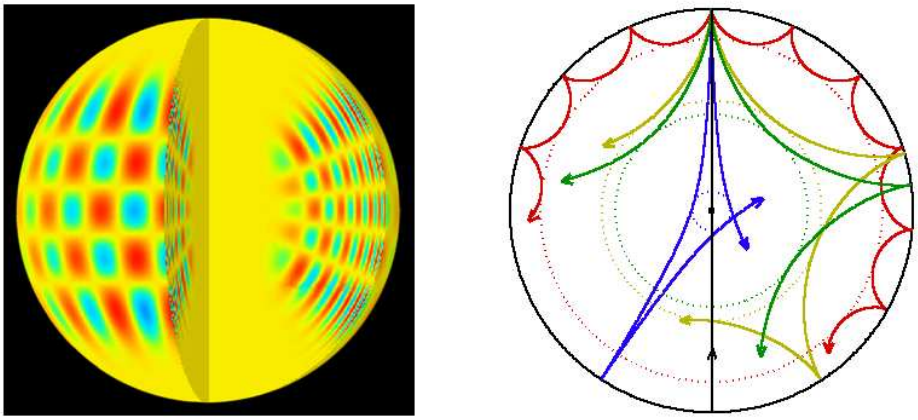

Figure 3.9. Schematics illustrating the nature of solar acoustic p-mode oscillations [72]. (Left) A computer image illustrating an oscillation within the convection zone made up of a radial mode (n=20) a latitudinal degree mode (ℓ=20) and a longitudinal order mode (m=16). (Right) Examples of p-modes showing how the acoustic waves traverse through the solar interior. Inward traveling waves are refracted by the material within the Sun where they can change direction and become outward traveling waves. At the surface, the waves are reflected back inward before once more being refracted. It is these surface manifestations that are measured and studied my helioseismologists.

used to produce power spectra of the Doppler velocities at the surface as a function of spherical harmonic degree ℓ and temporal frequency ν. Fig. 3.10 shows an example of such a spectra illustrating the vast variety of p-modes observable at the surface.

Using this vast array of helioseismic spectral data, investigations of the solar interior may be made such as the internal structure of the various zone within the Sun [64] and the differential rotation and dynamics of the solar interior [65]. The latter phenomena of internal differential rotation may have an impact into the convection features studied for this dissertation and will be investigated in Section 4.5.

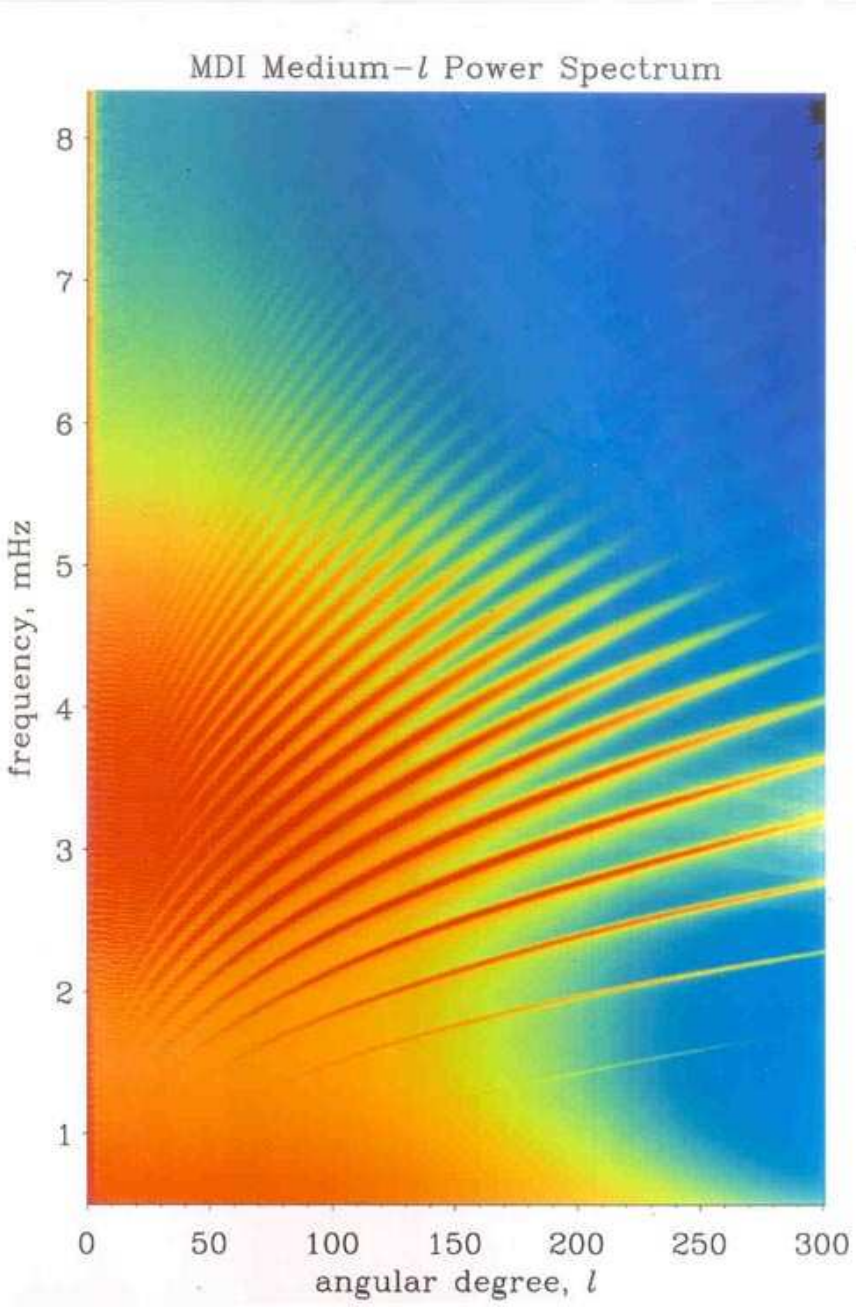

Figure 3.10. Power spectrum of solar acoustic modes derived from MDI Doppler data [64]. Data is averaged over spherical harmonic order m to produce a two dimensional spectrum as a function of ℓ and ν. Each ridge corresponds to a different radial mode n. Each ridge, however, is not a continuum of power but is made of discrete data points. The positions of the ridges on the diagram may be used to infer internal conditions within the Sun.

CHAPTER 4

DATA ANALYSIS AND SIMULATIONS

4.1 Introduction

The data received on Earth from MDI are raw data that include Doppler maps made up of line of sight velocities due to all motions visible on the solar surface. To be able to study particular features on the surface, the data must be processed to remove unwanted velocity components (as explained below), resulting in only those which are required for analysis, which, in the context of this dissertation, are non-axisymmetric flows due to internal convection motions.

The methods described in this section were previously conceived by researchers referenced herein prior to my involvement as a PhD student. Use of, and extensions to, these methods form the hub of my research work and are described in subsequent chapters. This chapter details such methods for the purpose of placing into context and understanding of my work perform for the PhD.

4.2 Data Reduction

A wide variety of velocity components contribute to the line of sight velocities that are observed within the Doppler maps collected by MDI. These include velocities due to:

a - differential rotation of the Sun [14];

b - the meridional circulation [73], which is a cyclic flow between the poles and equator at the surface and the base of the convection zone;

c - a disk-wide blueshift, becoming a redshift at the limb, due to the upflow of unresolved granulation cells [74];

d - the relative velocity of the the spacecraft carrying MDI itself;

e - p-mode oscillations [64], which are acoustic waves, with pressure as the restoring

force, with a period of around 5 minutes and occur due to the variability of the speed of sound within the Sun;

f - resolved convection cells due to different scales of convection [35] transporting heat from the Sun's interior to be radiated at the solar surface;

g - a redshift of the spectral line due to the gravitional influence of the Sun [75].

As much of the work contained within this dissertation focuses on manifestations and characteristics of supergranulation, the other components must first be subtracted from the original Doppler images received from MDI.

The following subsections outline the processes required to remove each unwanted component from the image (described in further detail by Hathaway [76]), leaving only velocity data due to the resolved convection cells required for our studies.

4.2.1 Selected Data

The MDI Doppler images used for the work discussed in this dissertation were gathered over a two month span during May and June of 1996. The main attraction of this data range is the very low amount of solar activity during this period, occurring near a minimum of the 11-year solar cycle. The sunspot count was subsequently very low, so that their interference with the surface convection patterns, that are the subject of our investigations, within this data was minimized. The MDI data used during this timespan were collected at a cadence of one minute.

4.2.2 Temporal Filtering

As the p-mode oscillations have a relatively short period, compared with the convection components of interest (Section 1.5), of about 5 minutes, Hathaway [77] devised a method to temporally filter out these oscillations, with longer-lived velocity components such as convective and long-lived axisymmetric flows remaining. Sets of weighted and unweighted discrete filters were tested on artificial data with varying results (Fig. 4.1). The ideal filter should be constructed to attenuate the p-mode signal as much as possible

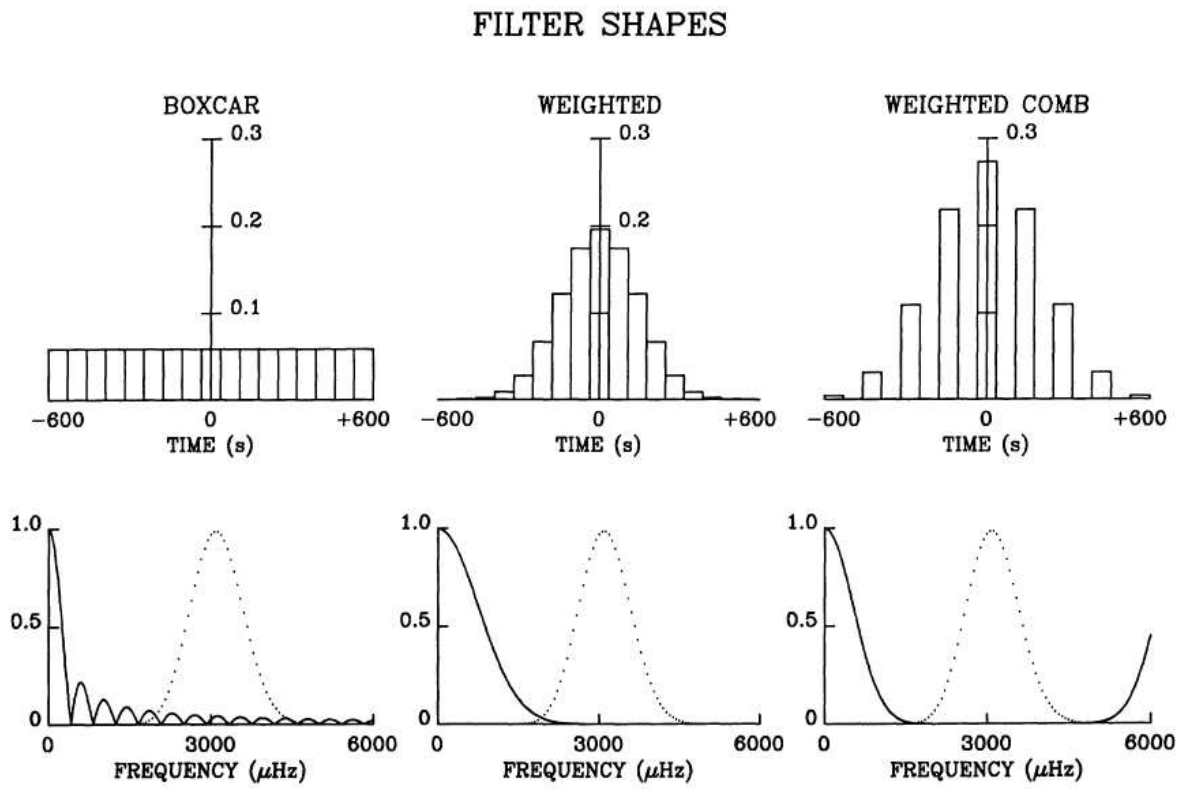

Figure 4.1. Shapes of the three filter types in the time (top) and frequency (bottom) domains [77]. The left filter is of a boxcar shape, the center is a near-Gaussian and to the right is a weighted comb near-Gaussian shape. In the lower set of figures, the dotted line corresponds to the frequency profiles of the p-mode oscillations whereas the solid line corresponds to the frequency transmission profiles of the filters.

and preferably have a short temporal filter length. Limiting the filter length means that the number of images involved in filtering out the signal is reduced and therefore any smearing of the remaining signal, such as supergranulation, is avoided.

The unweighted filter takes the form of a boxcar function (Fig. 4.1 left). However, when analyzed in frequency space, the filter exhibits transmission peaks over the range of the p-mode oscillation envelope. Even with a filter length of 60 minutes, the boxcar still transmits 2% of the p-mode signal (Fig. 4.2).

A weighted filtered was constructed from a near-Gaussian distribution (Fig. 4.1 center). The amount of overlap with the p-mode oscillations in frequency space is drastically reduced compared with the boxcar filter. The amount of attenuated signal reaches

the same amount for the 60 minute boxcar at around 20 minutes and after 30 minutes, the signal is removed altogether.

Another weighted filter was constructed from the same near-Gaussian distribution mentioned previously, but with every other discrete value set to zero, resulting in a weighted comb (Fig. 4.1 right). The amount of overlap with the p-mode oscillations in frequency space is nearly zero. For a filter length of 10 minutes, the signal is attenuated to the same value as that of the 60 minute boxcar. At around 15 minutes, the signal amplitude is reduced to zero.

As a series of images are utilized in the temporal filter, errors in the velocity data are produced from smearing effects due to solar rotation. These errors increase as the filter length is increased. The effect of reducing the p-mode signal must therefore be considered relative to the rotation errors (Fig. 4.3). Hathaway [77] found that the influence each error artifact can be balanced by specifying a filter length of around 20 minutes. This prevalent rotation error can subsequently be removed by artificially de-rotating the images to coincide with a common central image. This involves remapping the image data temporally on either side of the central image to coincide the Doppler pattern with the central image itself and adding them with appropriate weighting. This process may seem to depend on data that is on the other side of the Sun for use in the de-rotation process. However, as this data is situated near the limb and such data is removed in subsequent analyses, this problem does not carry through.

With this de-rotation process in operation, the filter length may be extended to further reduce the p-mode signal. The filter that results in the data used for this dissertation is of 31 minutes in length. Using the time series of images at 1-minute intervals, subsequent filtering and sampling results in a series of p-mode subtracted Doppler images with a cadence of 15 minutes.

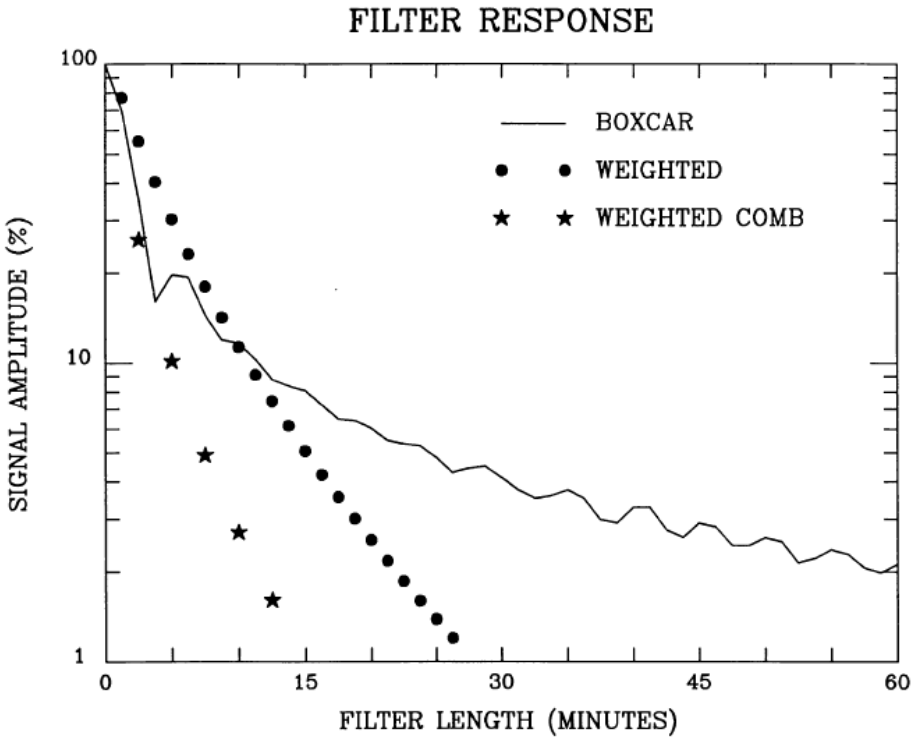

Figure 4.2. Response of each of the three types of filter [77].

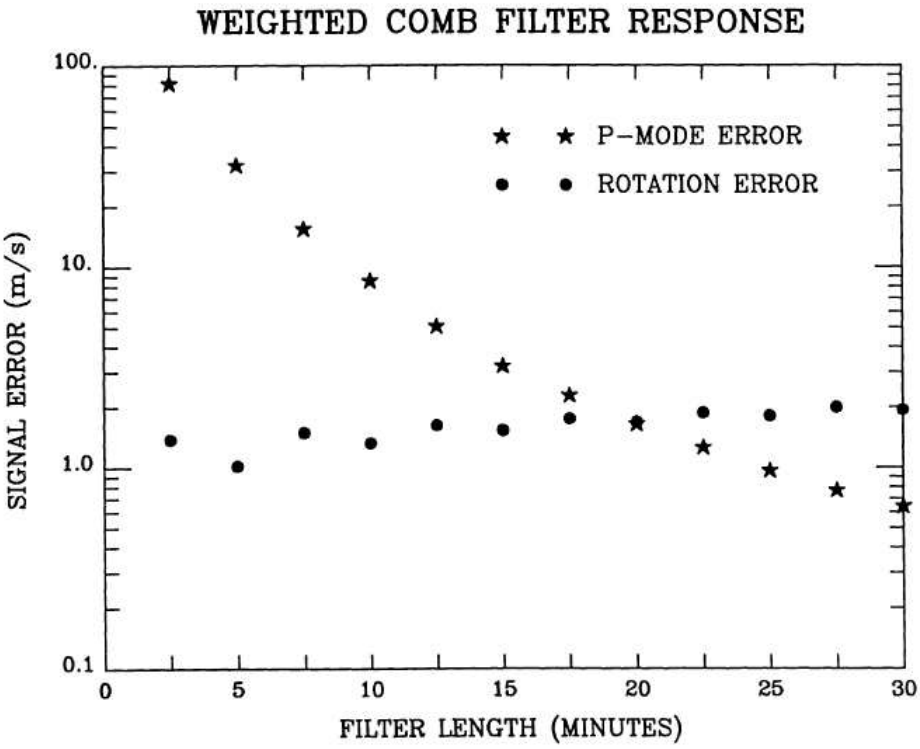

Figure 4.3. Comparison between the response of the comb filter to the p-mode oscillations and the rotation of the supergranule pattern [77].

4.2.3 Gravitational Redshift

From the General Theory of Relativity, it can be calculated that, due to the gravitational field of the Sun, the wavelength of any emitted photon will be redshifted. This gravitational redshift subsequently affects the spectral line observed by MDI. The result is an additional line-of-sight velocity component that must be removed. From a simple calculation, the corresponding Doppler velocity is around 636 m s^{-1}:

$$V_{\text{grav}} \;=\; \frac{GM_{\odot}}{R_{\odot}c} \;=\; 636 \text{ m s}^{-1}. \tag{4.1}$$

Here, G is the gravitational constant, $M_{\odot}$ is the solar mass, $R_{\odot}$ is the solar radius and c is the speed of light. Further investigations into the influence of the gravitational redshift on solar spectral lines have been made by Lopresto et al. [75].

4.2.4 Spacecraft Velocity

As described in previously (Section 3.1), the SOHO spacecraft, upon which MDI is mounted, orbits the Sun at Earth-Sun Lagrangian Point L1. Therefore, within any Doppler signal, velocity components exist due to the line of sight velocity of the spacecraft with respect to the Sun. Three-component velocity data (radial, east-west and north-south velocities) and other related geometric data are included as header files with each filtered Doppler image. For each image, the line-of-sight values can be extracted and the instrument velocity removed using

$$V(\rho,\Theta) = V(\rho,\Theta) - V_{\text{grav}} - V_R(1-\rho^2) + V_X\rho\sin\Theta - V_Y\rho\cos\Theta. \tag{4.2}$$

On the right side of (4.2), $V(\rho,\Theta)$ is the input Doppler velocity at an angular position ρ from disk center and an angle Θ clockwise from the solar rotation axis. V_{grav} is the gravitational redshift contribution as defined in the previous subsection. V_R, V_X and V_Y are the respective radial, east-west (parallel to the solar equator) and north-south (parallel to the solar rotation axis) velocities of the spacecraft. On the left side of (4.2), $V(\rho,\Theta)$ is the subsequent corrected Doppler velocity.

4.2.5 Heliographic Mapping

To aid in the removal of the axisymmetric flows, the velocity data is remapped from polar coordinate system (ρ,Θ) to one in heliographic coordinates (θ,ϕ). Here, θ is the colatitude of a point on the image as measured from the north pole, i.e. $\theta = 0$, $\pi/2$, π radians at the north-pole, equator and south-pole respectively, and ϕ is the longitude which increases from zero from the western limb. The mapping is performed using [76]

$$\sin\theta\cos\phi = \cos B_0\cos\rho - \sin B_0\cos\Theta \tag{4.3}$$

$$\sin\theta\sin\phi = -\sin\rho\sin\Theta \tag{4.4}$$

$$\cos\theta = \sin B_0\cos\rho + \cos B_0\sin\rho\cos\Theta. \tag{4.5}$$

Here B_0, the tilt of the solar north pole toward the observer, is also taken into consideration. The value of B_0 evolves as the observer moves around the Sun and is included for each image within its accompanying header file. B_0 varies between $\pm 7.12^\circ$ depending on the position of the observer, with 7.12° being the tilt of the solar rotation axis with respect to the ecliptic [78].

The velocity data contained within the image files are originally presented in a polar coordinate format, i.e., $V(\rho, \Theta)$. Thus, a remapping process, similar to coordinate remapping of (4.3)-(4.5), must apply to reformat the data to heliographic coordinates. This is performed by finding the coordinates of a pixel in a spherical polar coordinate system which which is mapped to a pixel in the heliographic coordinate system by performing a series of coordinate transformations, as described in the following.

Take a pixel with coordinates X_S, Y_S and Z_S to be its x,y,z coordinates on the surface of the Sun. In spherical polar coordinates, these are given by

$$\begin{pmatrix} X_S \\ Y_S \\ Z_S \end{pmatrix} = \begin{pmatrix} R\sin\theta\sin(\phi-\phi_0) \\ R\cos\theta \\ R\sin\theta\cos(\phi-\phi_0) \end{pmatrix}, \tag{4.6}$$

where R is the solar radius, θ and ϕ are defined earlier and ϕ_0 is the longitude at disk center.

These coordinates need to be transformed to account for the aforementioned angular tilt of the north pole towards the observer, B_0, and the angular tilt of the rotation axis clockwise with respect to the observer, P. As these are orthogonal transformations, they can be performed sequentially, using

$$\begin{pmatrix} X_B \\ Y_B \\ Z_B \end{pmatrix} = \begin{pmatrix} 1 & 0 & 0 \\ 0 & \cos B_0 & -\sin B_0 \\ 0 & \sin B_0 & \cos B_0 \end{pmatrix} \begin{pmatrix} X_S \\ Y_S \\ Z_S \end{pmatrix}, \tag{4.7}$$

and subsequently

$$\begin{pmatrix} X_P \\ Y_P \\ Z_P \end{pmatrix} = \begin{pmatrix} \cos P & \sin P & 0 \\ -\sin P & \cos P & 0 \\ 0 & 0 & 1 \end{pmatrix} \begin{pmatrix} X_B \\ Y_B \\ Z_B \end{pmatrix}. \tag{4.8}$$

The two-dimensional image disk coordinates are then calculated from the three-dimensional solar coordinates by

$$X_I = X_0 + \frac{X_P}{1 - \frac{Z_P}{R}\sin S_0}, \tag{4.9}$$

and

$$Y_I = Y_0 + \frac{Y_P}{1 - \frac{Z_P}{R}\sin S_0}, \tag{4.10}$$

where S_0 is the solar radius measured in arcseconds.

A data mask is also created to remove the pixels around the limb at 5% from the edge of the limb. This removed the problem of foreshortening at the limb which can result in anomalous data values. A similar data mask can also be used to remove active regions in real data to be replaced by synthetic data to fit the image. This process is not used for data described in this dissertation, but is discussed with more detail in [76].

As the described mapping is not 1:1, not only does perspective have to be taken into consideration, using (4.9) and (4.10), but also the influence of other points adjacent

to the point in question. Thus, a bi cubic interpolation from adjacent points is also performed using

$$V_{map}(i,j) = \sum_{\mu=0}^{3}\sum_{\nu=0}^{3} W_{x\mu} W_{y\nu} F_{\mu\nu}, \tag{4.11}$$

where $V_{map}(i,j)$ is the remapped velocity at the ith and jth pixel coordinates, with

$$F_{\mu\nu} = V(X_{int} + (\mu - 1), Y_{int} + (\nu - 1)), \tag{4.12}$$

where $V(X_{int}, Y_{int})$ is the velocity on the two-dimensional image disk at the rounded coordinates found from (4.9) and (4.10).

$W_{x\mu}$ and $W_{y\nu}$ in (4.11) are given by (after [79])

$$W_{x_i 0} = -\frac{1}{2}\Delta x_i + (\Delta x_i)^2 - \frac{1}{2}(\Delta x_i)^3, \tag{4.13}$$

$$W_{x_i 1} = 1 - \frac{5}{2}(\Delta x_i)^2 + \frac{3}{2}(\Delta x_i)^3, \tag{4.14}$$

$$W_{x_i 2} = \frac{1}{2}\Delta x_i + 2(\Delta x_i)^2 - \frac{3}{2}(\Delta x_i)^3, \tag{4.15}$$

$$W_{x_i 3} = -\frac{1}{2}(\Delta x_i)^2 + \frac{1}{2}(\Delta x_i)^3, \tag{4.16}$$

where i=0,1 so that $x_0 = x$ and $x_1 = y$. Δx_i is defined as the difference between X_I - X_{int} and Y_I - Y_{int}, respectively.

The values of $V_{map}(i,j)$ calculated from (4.11) are then used for the subsequent analyses.

4.2.6 Rotation Profile

Observations by Christoph Scheiner in the 17th century provided evidence of the differential rotation property of the Sun with sunspots being seen to traverse across the solar disk at a faster rate near the equator compared to those near the poles. However, it wasn't until the 19th century when Carrington [80] made the first numerical measurements to substantiate the earlier observations.

Subsequent investigations, using data such as Doppler shift [81] and magnetogram [82] correlations, have provided a functional form for the differential rotation, Ω, as a fourth order polynomial in the sin of the latitude, ψ,

$$\Omega = A + B\sin^2\psi + C\sin^4\psi \tag{4.17}$$

where the coefficients A, B and C are determined from data fitting, with A representing the equatorial rotation rate. A list of derived values for these coefficients is given by Stix [15].

As the differential rotation constitutes a Doppler velocity field (Fig. 4.5) (and is actually the strongest velocity component), it must be removed from the MDI data. Hathwaway [76] provides a method of doing this.

The rotation velocity at a given colatitude, θ, averaged between longitudes ϕ_1 and ϕ_2 is given by

$$U^0_\phi(\theta)\cos B_0 = \frac{1}{N(\theta)}\int_{\phi_1}^{\phi_2} V(\theta,\phi)\cos^2\phi\sin\phi d\phi \tag{4.18}$$

where B_0 is the angular tilt of the Sun, $V(\theta,\phi)$ is the line of sight velocity at a given colatitude and longitude position on the solar disk and $N(\theta)$ is a normalization factor taken between heliographic longitudes ϕ_1 and ϕ_2.

The rotation velocity Doppler map values derived from (4.18) are then fitted by

$$U^0_\phi(\theta) = \sum_{\ell=1}^{\ell_{max}} T^0_\ell[\ell(\ell+1)]^{1/2}\overline{P}^1_\ell(\cos\theta) \tag{4.19}$$

where $\overline{P}^1_\ell(\cos\theta)$ is an associated Legendre polynomial of degree ℓ and order 1 and T^0_ℓ is the toroidal spectral coefficient of degree ℓ and order 0 measured in m s^{-1}. The summation is executed up to ℓ_{max} equal to 8. Once found, this fit can be removed from the original data.

4.2.7 Convective Blueshift

With convection cells spanning a wide range of sizes, as described in Section 1.5, there will exist a sizeable number of granules that are too small to be resolved at the

normal resolution with the full-disk observations of MDI. However, a contribution to the Doppler velocity signal due to these disk-wide unresolved convection cells is still observed. As the high intensity signals of the surface upflows within the granules dominate the low intensity downflows around their edge, the velocity field is seen as a continuous upflow and the Doppler signal is blueshifted. This phenomenon is called the convective blueshift [15] (also known as the limbshift due to the signal's variation toward the limb) and need to be removed to study any underlying velocity fields. However, this removal is not a straightforward subtraction procedure as is the process for the gravitational redshift as it is found that the convective blueshift exhibits a slow disk center-to-limb variation [74] (Fig. 4.5) as the radial velocity responsible for the convective blueshift reduces along the line-of-sight towards the limb.

Beckers and Nelson [74] showed that whereas the convective blueshift is due to the vertical flows of the unresolved elements, the horizontal flows within the cells are responsible for the variation toward the limb. Near the limb, horizontal velocities along the line-of-sight directed away from the observer combine with the high intensity of the granules situated behind them (i.e. further toward the limb), the result being that these horizontal velocity signals now begin to dominate. Indeed very near the limb the blueshift becomes a redshift with velocity signals stronger than that of the gravitational redshift described earlier.

4.2.8 Meridional Circulation

Like the solar rotation, investigations of the meridional circulation can be traced back to the 19th century [80]. Despite being the weakest velocity component (typically around 20 m s^{-1} [73]), it still plays an important role in the dynamics of the convection zone and may be influential in controlling the 22 year solar-cycle [83], [84].

The surface profile of the meridional circulation shows a flow of varying strength from the equator to the pole [73] (Fig. 4.5). However, as the meridional circulation seems to play a role in determining the solar cycle, specifically influencing the equatorward drift

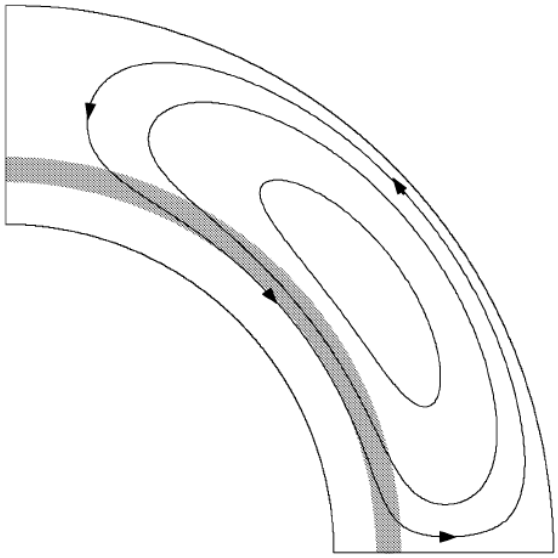

Figure 4.4. A schematic cross-section of the Sun showing the meridional circulation profile within the convection zone [85]. The tachocline at the base of the convection zone is shaded gray.

of sunspots, it is speculated that an equatorward component of the meridional circulation exists at the base of the convection zone [84] despite the current lack of helioseismic evidence. With respective inward and outward radial flows at the poles and the equator, a circulatory flow within the convection zone is set up (Fig. 4.4) [85].

4.2.9 Limbshift and Meridional Flow Removal

The process described by Hathaway [76] requires that the two previously described velocity components must be removed in conjunction with each other. The main reason for this is outlined in the first of three processes to extract these signals.

The first step begins by remapping the Doppler data to a heliocentric value of the angular distance from disk center, ρ, over all position angles, Θ. The data is averaged into a series of finite width annular radial bins. This process combines both convective blueshift values and the average of the meridional circulation, which must be separated in a later step. The averaged velocity data within each radial bin is calculated thus

$$V_{LS}(\rho) = \frac{1}{2\pi} \int_0^{2\pi} V(\rho, \Theta) d\Theta \tag{4.20}$$

where $V(\rho,\Theta)$ is the velocity at heliocentric angular distance from disk center, ρ, and position angle, Θ. Readjustments must be made during averaging to compensate for the data being weighted toward the outside of each annular bin; there are more data points at the outer edge than at the inner edge. A fit to the data collected in (4.20) can then be applied using a polynomial of the form

$$V_{LS}(\rho) = \sum_{n=0}^{n_{max}} C_n(1-\cos\rho)^n \tag{4.21}$$

calculated up to $n_{max} = 4$, giving a set of limb shift coefficients, C_n. At this point, the fit (including both limbshift and the average meridional circulation values) can be removed from the original data.

What now remains of the axisymmetric velocity fields is the meridional circulation component minus its average. This can be removed by fitting this component with a modified profile to account for the subtracted average

$$V_{MC}(\theta,\phi) = -\sum_{\ell=1}^{\ell_{max}} S_\ell^0[\ell(\ell+1)]^{1/2}(F_{MC}(B_0,\theta,\phi) - G_{MC}(B_0,\theta,\phi)) \tag{4.22}$$

where

$$F_{MC}(B_0,\theta,\phi) = \overline{P}_\ell^1(\cos\theta)[\sin B_0\sin\theta - \cos B_0\cos\theta\cos\phi] \tag{4.23}$$

and

$$G_{MC}(B_0,\theta,\phi) = \frac{1}{2\pi}\int_0^{2\pi} \overline{P}_\ell^1(\cos\theta)[\sin B_0\sin\theta - \cos B_0\cos\theta\cos\phi]d\Theta \tag{4.24}$$

resulting in

$$G_{MC}(B_0,\theta,\phi) = \Big[\frac{2}{2\ell+1}\Big]^{1/2}\overline{P}_\ell^0(\sin B_0)\sin\rho(\theta,\phi)\overline{P}_\ell^1(\cos\rho(\theta,\phi)). \tag{4.25}$$

All quantities have been previously defined, except S_ℓ^0 which is the poloidal spectral coefficient of degree ℓ and order 0. Eq. (4.23) accounts for the meridional circulation profile, whereas (4.25) accounts for its average. Summing (4.22) up to $\ell_{max} = 8$, the poloidal spectral coefficients of degree ℓ and order 0 can be extracted and the fit removed from the data.

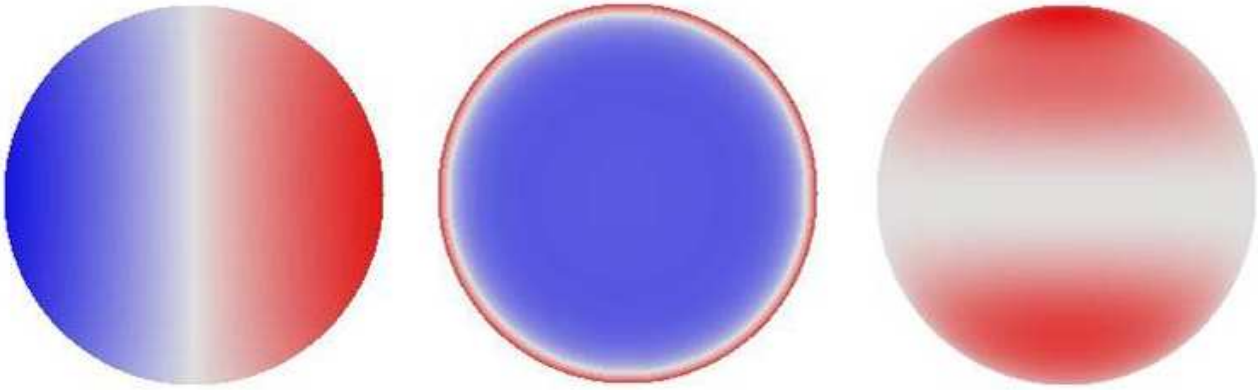

Figure 4.5. Doppler images of the three axisymmetric flows that require removal from the MDI images to extract convection velocity maps. (Left) Rotation; (Middle) Convective blueshift; (Right) Meridional circulation.

Knowing the meridional circulation spectral coefficients now means that the average can be removed from the limbshift profile produced in the first step

$$V_{LS}(\rho) = V_{LS}(\rho) + \sum_{\ell=1}^{\ell_{max}} S_\ell^0 [\ell(\ell+1)]^{1/2} G_{MC}(B_0, \rho) \tag{4.26}$$

the second term on the right hand side then being used to calculate a correction term to the convective blueshift coefficients using (4.21).

4.3 Data Analysis

After all the non-convective velocity components have been removed, what remains are the line-of-sight Doppler velocity fields due to convection mechanisms with spatial sizes that are resolvable by the optics of MDI. Fig. 4.6 shows an example of such a Doppler map, where red-shifted flows are colored red, and blue-shifted are colored blue. It can be seen that the signals become more intense toward the limb showing the dominance of horizontal velocities along the surface over the perpendicular radial flows.

As all resolvable convection components exist in Fig. 4.6, it is illustrative to deconstruct the image to produce a distribution of the range of different convection cell sizes

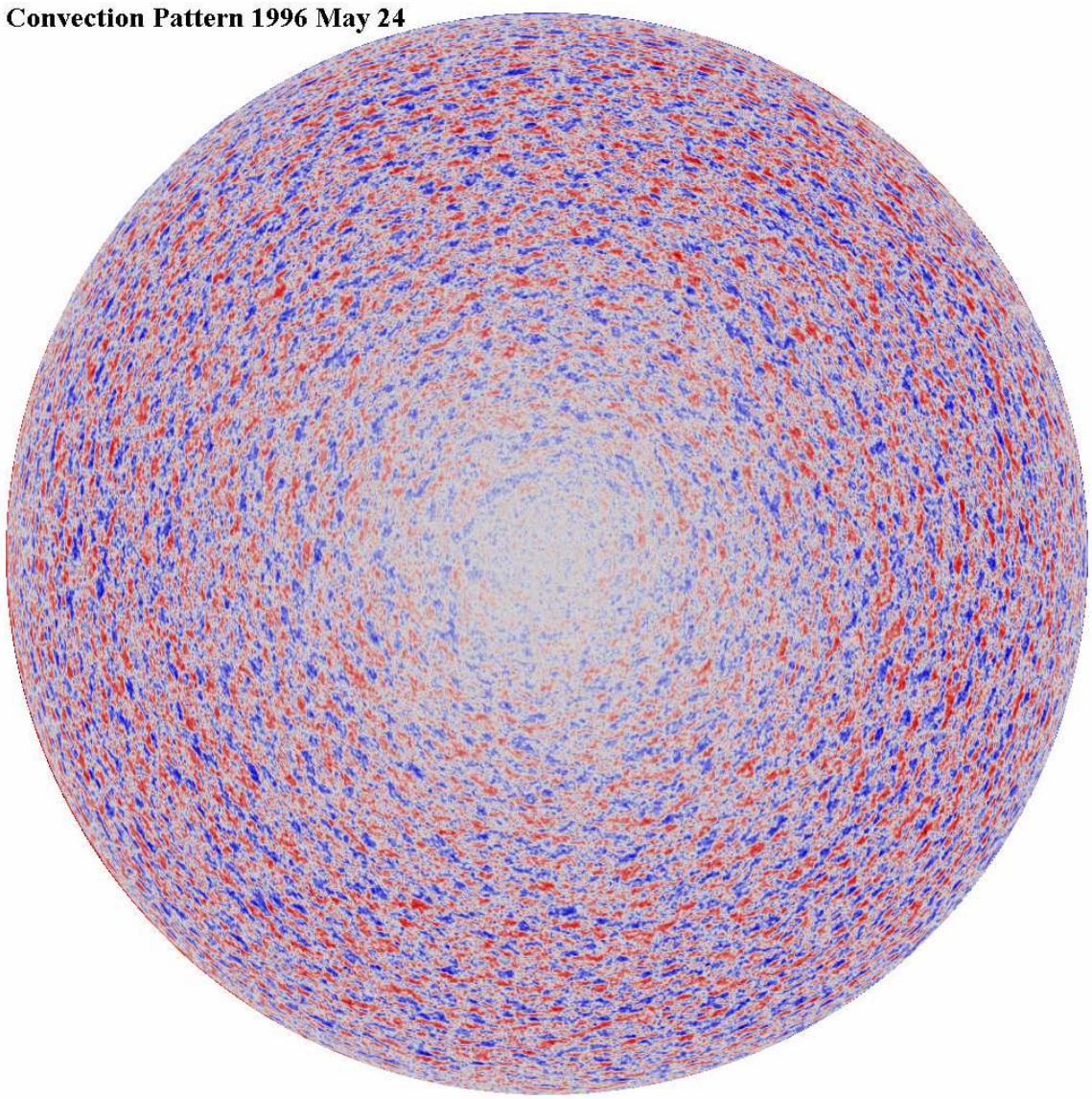

Figure 4.6. Image of the Doppler velocity fields remaining due to non-axisymmetric convection flows after all the axisymmetric velocities from the original MDI image have been removed [35].

that contributed to the final velocity field. This process, as follows, is described in [76] and [35].

Whereas the maximum line-of-sight values extracted from the Doppler maps give a reasonable estimate of horizontal flow velocities on the solar surface, further analysis of the maps can also give information on the typical velocities for radial flows at the surface, which are found to be dependent on the characteristic size of the convection cells [86].

4.3.1 The Photospheric Convection Spectrum

To separate out all of the contributing convection elements, the Doppler data (similar to that which produce the image in Fig. 4.6) must be mapped onto heliographic coordinates (co-latitude θ and longitude ϕ) and then mapped onto the spherical harmonics (Y_ℓ^m) using

$$A_\ell^m = \frac{1}{N_\ell^m} \int_{-1}^{1} \int_{\phi_1}^{\phi_2} V(\theta,\phi)\ W_2(\theta,\phi)\ Y_\ell^m(\theta,\phi)\ d\theta\ dx \tag{4.27}$$

where A_ℓ^m are complex amplitudes, N_ℓ^m is a normalization factor given by

$$N_\ell^m = \int_{-1}^{1} \int_{\phi_1}^{\phi_2} W_2(\theta,\phi)\ [Y_\ell^m(\theta,\phi)]^2\ d\theta\ dx \tag{4.28}$$

with

$$dx \equiv d(\cos\theta) \tag{4.29}$$

and $W_2(\theta,\phi)$ is a weighting function that smoothly apodizes the data at the limiting longitudes ϕ_1 and ϕ_2. What results is a two-dimensional convection spectrum given by the complex amplitudes, A_ℓ^m, and a set of corresponding random phases.

After subtracting a temporal average of the complex spectra, which removes any further stationary components remaining in the data that was missed by the processes in the previous section, the power at a given wavenumber, ℓ, can be determined by summing the product of the complex amplitudes with their complex conjugates over each order m

$$P(\ell) = \sum_{m=-\ell}^{\ell} |A_\ell^m|^2. \tag{4.30}$$

With the Doppler image diameter being 1024 pixels, the wavenumber range in the convection spectrum covers $\ell = 1$ to $\ell = 1024$, corresponding to a feature with a size comparable to the semi-circumference of the Sun, to one the size of a single pixel (i.e. $\pi R_\odot/512$). Fig. 4.7 shows an example of the convection spectrum constructed from the Doppler map displayed in Fig. 4.6. The main feature is a peak situated at around

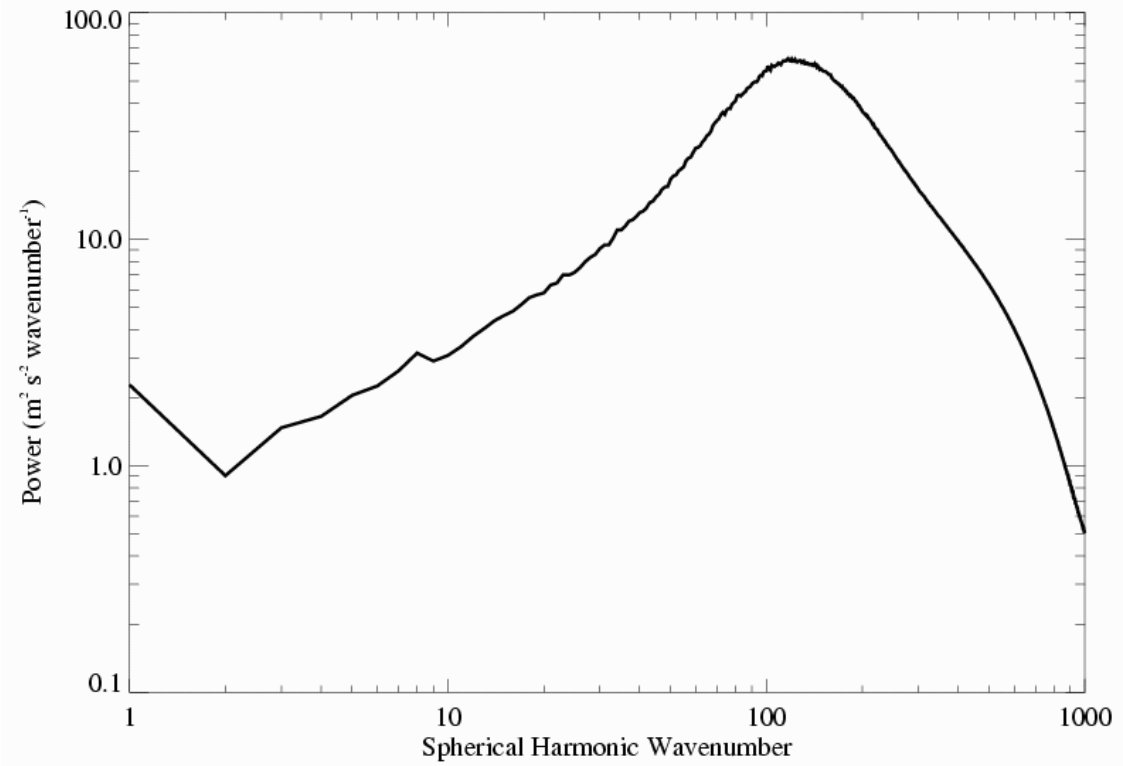

Figure 4.7. Image of the power spectrum due to non-axisymmetric convection flows [35].

$\ell = 120$ that represents supergranules [35], [87]. With $\ell = 1$ corresponding to a solar circumference, the supergranule diameter derived from this spectrum can be estimated

$$\lambda(\ell) = \frac{2\pi R_\odot}{\ell} = \frac{4400}{\ell}\text{Mm} \tag{4.31}$$

giving a characteristic size for $\ell = 120$ of 36 Mm.

Owing to the noise at lower wavenumbers, there is no definite sign of giant cells which are expected to peak at around $\ell = 60$. Further, mesogranules that have been proposed to exist [33], with a peak near $\ell = 400$, are not seen. Convection cells with such wavenumbers do exist, as can be seen by the power at such wavenumbers in Fig. 4.7, but no distinct feature around that wavenumber can be identified. Instead, the contribution to the spectral power is provided by smaller than average supergranules and larger than average granules.

The peak due to granules themselves is not seen as they are not resolved at the magnification used by MDI to provide these signals. However, using the higher resolution

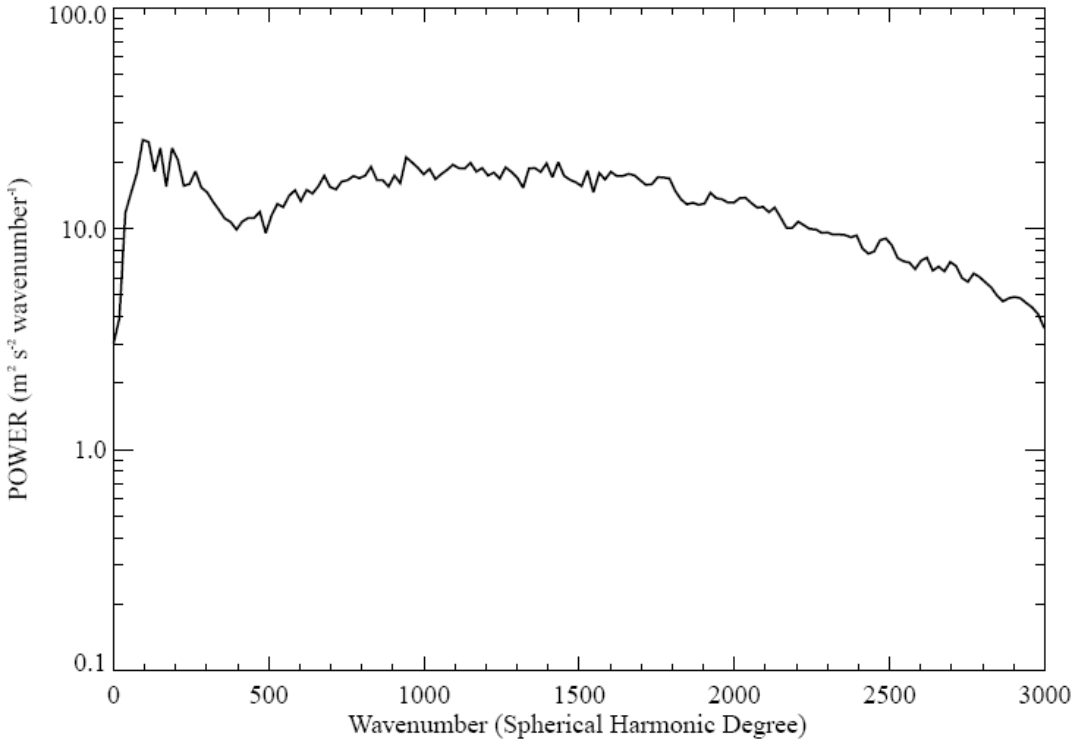

Figure 4.8. High resolution power spectrum due to non-axisymmetric convection flows showing both the supergranule and granule peaks [35].

optics (at 3× magnification) the range of the convection spectrum can be extended (Fig. 4.8). As well as the narrow supergranule peak near $\ell = 120$, a second broader, less prominent peak is now seen near $\ell = 1000$. This peak represents the granules. The loss of power above $\ell = 1000$, however, may not be representative of the actual size distribution as not only are many granules not resolved at higher wavenumbers, but their lifetimes are on the order of the temporal filter discussed in Section 4.2.2 (earlier section in this chapter), which may remove some of the signal [35].

4.3.2 Radial Flows in Supergranules

Whereas the Doppler maps shown in Fig. 4.6 provide only information on the line-of-sight velocities with respect to MDI, to understand some of the dynamics of convective flows, it is illustrative to extract the actual velocities with respect to a reference frame

situated at the solar surface. For this, two sets of orthogonal velocities can be extracted, horizontal (flows along the solar surface) and radial (those perpendicular to the surface).

Hathaway et al. [86] conducted a study of a series of Doppler maps to de-construct the line-of-sight velocities into their horizontal and radial components. They find that the mean squared line-of-sight velocity averages over 200 annuli situated over a range of heliocentric angles, ρ, from the center of the disk can be given by

$$\overline{V^2}(\rho) = \overline{V_r^2} + \left[\overline{V_h^2} - \overline{V_r^2} \right] \sin^2 \rho \tag{4.32}$$

where $V(\rho)$ is the line-of-sight velocity at heliocentric angle and ρ, V_r, and V_h are the radial and horizontal components with the overbars representing averages, respectively.

Eq. (4.32) has the functional form of a straight line graph with $\overline{V^2}(\rho)$ and $\sin^2 \rho$ being the dependent and independent variables, respectively. Plots are then constructed over a set of 20 images using (4.32), and the average taken of these plots. A straight line fit may then be applied to this average yielding a value for the radial velocity from the y-intercept and for the horizontal velocity from the gradient. Results yield horizontal velocities of around 260 m s^{-1} and radial velocities of nearly 30 m s^{-1}. The former value is noticeably smaller than that extracted from the maximum line-of-sight velocities. This is because data in the current method are only included out to 60% of the limb as foreshortening near the limb causes the plot to deviate from a straight line. Therefore, the horizontal flows are underestimated due to this lack of data.

The study by Hathaway et al. [86] also considered flow speeds for different sized convection components. Spectral windows centered at particular wavenumbers were constructed to filter out unwanted convection cell sizes while including the necessary sized components. In general, it is found that as the cell size decreases, both the radial and horizontal flow velocities decrease. However, it is further found that the ratio of the former to the latter increases with decreasing cell size. For supergranules, typical flow velocities are found using a filter centered at $\ell = 128$ with $V_r = 13.4$ m s^{-1}, $V_h = 153.1$

m s^{-1} and $V_r/V_h = 0.09$, resulting in the observation that horizontal flows are generally around 10 times faster than radial flows.

4.4 Data Simulations

To gauge a better understanding of the prevailing physical conditions, simulations are constructed to model such conditions within which user-defined variables can be adjusted to determine the model's behavior and match the physical conditions up to the limit of the simulation.

The goal of any simulation in the present context is to recreate an artificial map of the line-of-sight Doppler velocities that correctly matches those from MDI. The map should include both the axisymmetric and non-axisymmetric components mentioned in the previous section, which can then be removed using a similar to that already discussed.

At a colatitude point (defined as the angular distance from the north-pole to any point on a spherical surface), θ, and azimuth, ϕ, the line of sight velocity, $V_{\rm los}(\theta, \phi)$, can be derived from three orthogonal elements for the radial, latitudinal and azimuthal velocities, $V_r(\theta, \phi)$, $V_\theta(\theta, \phi)$, and $V_\phi(\theta, \phi)$, respectively,

$$\begin{aligned} V_{\rm los}(\theta, \phi) = \quad & V_r(\theta, \phi)[\sin B_0 \cos\theta + \cos B_0 \sin\theta \cos\phi] \\ & + V_\theta(\theta, \phi)[\sin B_0 \sin\theta + \cos B_0 \cos\theta \cos\phi] \\ & + V_\phi(\theta, \phi)[\cos B_0 \sin\phi] \end{aligned} \tag{4.33}$$

where B_0 is the tilt of the Sun's north pole toward the observer. As with general cases of Doppler shifts, velocities toward the observer are negative and observed as blueshifts, while those away from the observer are positive and observed as redshifts.

Chandrasekhar [88] showed that any vector field on the surface of a sphere can be expressed as a linear combination of toroidal and poloidal fields, and the radial compo-

nent, Hathaway [79] derived the three orthogonal velocity components that contribute to $V_{\rm los}(\theta,\phi)$ as

$$V_r(\theta,\phi) = \sum_{\ell=0}^{\ell_{max}} \sum_{m=0}^{\ell} R_\ell^m Y_\ell^m(\theta,\phi), \tag{4.34}$$

$$V_\theta(\theta,\phi) = \sum_{\ell=0}^{\ell_{max}} \sum_{m=0}^{\ell} \left[S_\ell^m \frac{\partial Y_\ell^m(\theta,\phi)}{\partial\theta} + T_\ell^m \frac{1}{\sin\theta} \frac{\partial Y_\ell^m(\theta,\phi)}{\partial\phi} \right], \tag{4.35}$$

$$V_\phi(\theta,\phi) = \sum_{\ell=0}^{\ell_{max}} \sum_{m=0}^{\ell} \left[S_\ell^m \frac{1}{\sin\theta} \frac{\partial Y_\ell^m(\theta,\phi)}{\partial\phi} - T_\ell^m \frac{\partial Y_\ell^m(\theta,\phi)}{\partial\theta} \right], \tag{4.36}$$

where R_ℓ^m, S_ℓ^m and T_ℓ^m are the respective radial, poloidal and toroidal spectral coefficients in latitudinal degree, ℓ and azimuthal order, m.

To determine values for the three velocity components, values for R_ℓ^m, S_ℓ^m and T_ℓ^m have to therefore be assigned. As mentioned in Sections 1.5 and 4.32, both radial and horizontal velocities are attributed to both granules and supergranules. As seen in (4.34)-(4.36), the radial spectral coefficient contributes to the radial velocity, $V_r(\theta,\phi)$, while the poloidal and toroidal coefficients contribute to the horizontal flows, $V_\theta(\theta,\phi)$ and $V_\phi(\theta,\phi)$. In the context of convection cells, the poloidal flows correspond to divergent flows direct outward from the cell center to its boundary, while the toroidal flows correspond to circulation within the cell.

To extract these spectral coefficients, a convection velocity power spectrum can be created dependent on wavenumber ℓ, similar to that constructed from the MDI velocity images of the previous section. The spectrum should be constructed to provide spectral coefficients to contribute to Doppler velocity maps along with the axisymmetric flows. Subjecting these maps to similar analysis described in the previous section, one can extract a synthesized photospheric convection spectrum. The goal is to produce a final synthetic spectrum that closely matches one extracted from MDI data.

4.4.1 Building a Synthetic Photospheric Convection Spectrum

To construct the initial spectrum, two modified Lorentzian functions are summed to represent a power spectrum from the spectral coefficients R_ℓ^m and S_ℓ^m. For the studies

given in this dissertation, the toroidal components are not included. Although a rotational element is expected to the flow within the convection cells at the surface due to Coriolis forces provided by the Sun's rotation, they are taken to have a negligible effect on the features studied here. The strength and possible effects of the Coriolis force on supergranule cells have been described by Hathaway [44].

The two functions contribute to the poloidal and radial coefficients, although they do not need to be constructed separately as they can be related to one another following the previously mentioned study of radial flows within supergranules [35] which relates their radial and horizontal velocities. From this work, the two coefficients can be related as,

$$|R_\ell| = \left(0.09 + \frac{\ell}{25000}\right)\sqrt{\ell(\ell+1)}|S_\ell|. \tag{4.37}$$

The 0.09 factor accounts for the overall relative strength ratio between radial and poloidal flows, while the $\ell/25000$ accounts for the variation in relative strength with wavenumber [86]. The poloidal spectral coefficient is then constructed from summing each Lorentzian respectively representing the supergranule and granule convection components,

$$|S_\ell| = \frac{7\times10^4}{2\ell+1}\frac{1}{(\ell-110)^2+100^2} + \frac{1\times10^8}{2\ell+1}\frac{1}{(\ell-4000)^2+4000^2}. \tag{4.38}$$

The first term represents a function of the supergranule component peaking at $\ell \sim 110$, while the second term represents a function of the supergranule component peaking at $\ell \sim 4000$. Each component and the resultant function are shown in Fig. 4.9. Extracting the spectral coefficient amplitudes contributing to this function and modulating them by a random phase, thus extending the spectral coefficient dependency to m as well as ℓ while also removing the phase coherence between the coefficients, for example,

$$|S_\ell^m| = |S_\ell|e^{im\phi}, \tag{4.39}$$

where ϕ is a random phase angle, the process of constructing the velocities can commence.

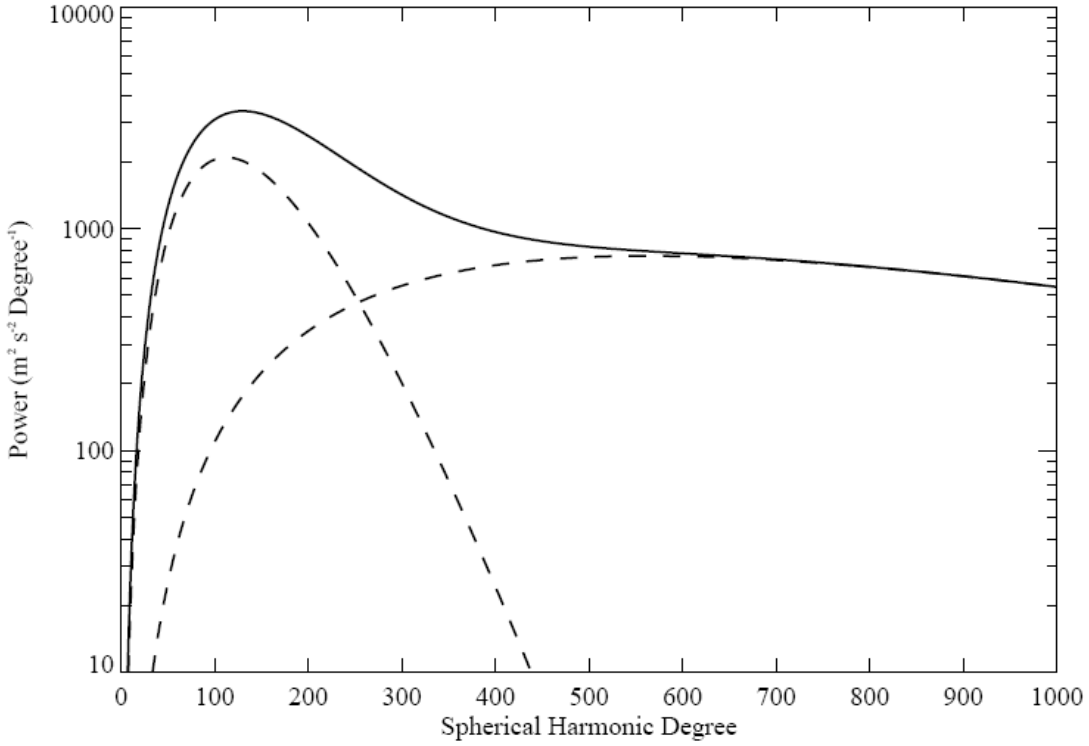

Figure 4.9. Profiles showing the supergranule and granule components (dashed lines) that comprise a synthetic photospheric convection profile (solid line) [35].

4.4.2 Building Realistic Doppler Maps

To begin the construction of a Doppler map image, spectral profiles for the velocity components are produced. The previous subsection describes how a photospheric convection profile is built. Additionally, to create a more realistic spectrum, the input spectral amplitudes and phases for each component are randomly modulated to remove coherence of the different modes to make the data as realistic as possible.

Profiles for rotation and meridional flow are also required. Both are zeroth order toroidal and poloidal, respectively, with values used for low degrees only. The three component toroidal spectrum for the rotational profile contribution is given by

$$T_1^0 = 1483 \tag{4.40}$$

$$T_3^0 = -26 \tag{4.41}$$

$$T_5^0 = -4 \tag{4.42}$$

while the two component poloidal spectra for the meridional flow contribution is given by

$$S_2^0 = 17 \tag{4.43}$$

$$S_4^0 = -26. \tag{4.44}$$

These values are used to produce velocity data which are combined with the convection flow velocity data to produce an image. These images are essentially simulated snapshots of a synthetic flow pattern. It should be noted that the none of the flows described until now are used to dynamically evolve the flow.

Evolution of the pattern progresses in two ways. One way is to evolve the pattern across the image disc using a solid body rotation profile and the other is to evolve the pattern itself using randomized phases so that supergranule cells within the pattern (around $\ell = 110$) evolve with a lifetime of about two days. As discussed in Section 4.2.6, the Sun rotates differentially, but a solid body profile is used as an initial approximation. The method of adding a differential rotation evolution of the spectral coefficients is involved and described in a later section.

The velocity components were then found from (4.34)-(4.36), using relations that equate the spherical harmonics to the Legendre polynomials, as well as the Legendre polynomial recursion relations

$$Y_\ell^m(\theta,\phi) = \overline{P}_\ell^1(\cos\theta)e^{im\phi}, \tag{4.45}$$

$$\begin{aligned}\frac{\partial}{\partial\theta}Y_\ell^m(\theta,\phi) = \quad & \frac{1}{\sin\theta}[\ell C_{\ell+1}^m \overline{P}_{\ell+1}^m(\cos\theta) \\ & +(\ell+1)C_\ell^m \overline{P}_{\ell-1}^m(\cos\theta)]e^{im\phi},\end{aligned} \tag{4.46}$$

and

$$\frac{1}{\sin\theta}\frac{\partial}{\partial\phi}Y_\ell^m(\theta,\phi) = \frac{1}{\sin\theta} im \overline{P}_{\ell+1}^m(\cos\theta)e^{im\phi}, \tag{4.47}$$

where

$$C_\ell^m = \left[\frac{(\ell+m)(\ell-m)}{(2\ell+1)(2\ell-1)}\right]^{1/2}, \tag{4.48}$$

to give for each discrete colatitude θ_j, and order m,

$$V_r(\theta_j, m) = \sum_{\ell=m}^{\ell_{max}} R_\ell^m \overline{P}_\ell^m(\cos\theta), \tag{4.49}$$

$$\begin{aligned} V_\theta(\theta_j, m) = & \frac{1}{\sin\theta_j} \sum_{\ell=m}^{\ell_{max}} S_\ell^m [\ell C_{\ell+1}^m \overline{P}_{\ell+1}^m(\cos\theta_j) \\ & - (\ell+1) C_\ell^m \overline{P}_{\ell-1}^m(\cos\theta_j)] \\ & + T_\ell^m [im \overline{P}_{\ell+1}^m(\cos\theta_j)], \end{aligned} \tag{4.50}$$

$$\begin{aligned} V_\phi(\theta_j, m) = & \frac{1}{\sin\theta_j} \sum_{\ell=m}^{\ell_{max}} S_\ell^m [im \overline{P}_{\ell+1}^m(\cos\theta_j)] \\ & - T_\ell^m [\ell C_{\ell+1}^m \overline{P}_{\ell+1}^m(\cos\theta_j) \\ & + (\ell+1) C_\ell^m \overline{P}_{\ell-1}^m(\cos\theta_j)]. \end{aligned} \tag{4.51}$$

Due to the parity properties of the Legendre polynomials, velocities need only be initially calculated for one hemisphere (say northern). Velocities within the southern hemisphere are then found from those in the north. Velocities are calculated for each component r, θ and ϕ, at each colatitude θ_j, and each spherical harmonic order m,by using (4.49)-(4.51), summing over the spherical harmonic degrees ℓ.

This results in six velocity components, i.e. three directional velocities for both velocities. These then undergo an inverse Fast Fourier Transform [89] to bring the velocities from spectral into velocity space. The real part is taken giving three directional velocities in both hemispheres at all colatitudes and longitudes.

A number of steps are taken to convert these three velocity components into a single line-of-sight value: **a** - each pixel is broken up into grid of 49 (i.e., 7×7) subpixels; **b** - each subpixel is mapped from Cartesian to Heliographic coordinates. **c** - a bi cubic interpolation of each velocity component from adjacent points is performed around each subpixel to account for the re-mapping process. **d** - each component is projected onto the line-of-sight and summed over all subpixels to produce the final line of sight velocity

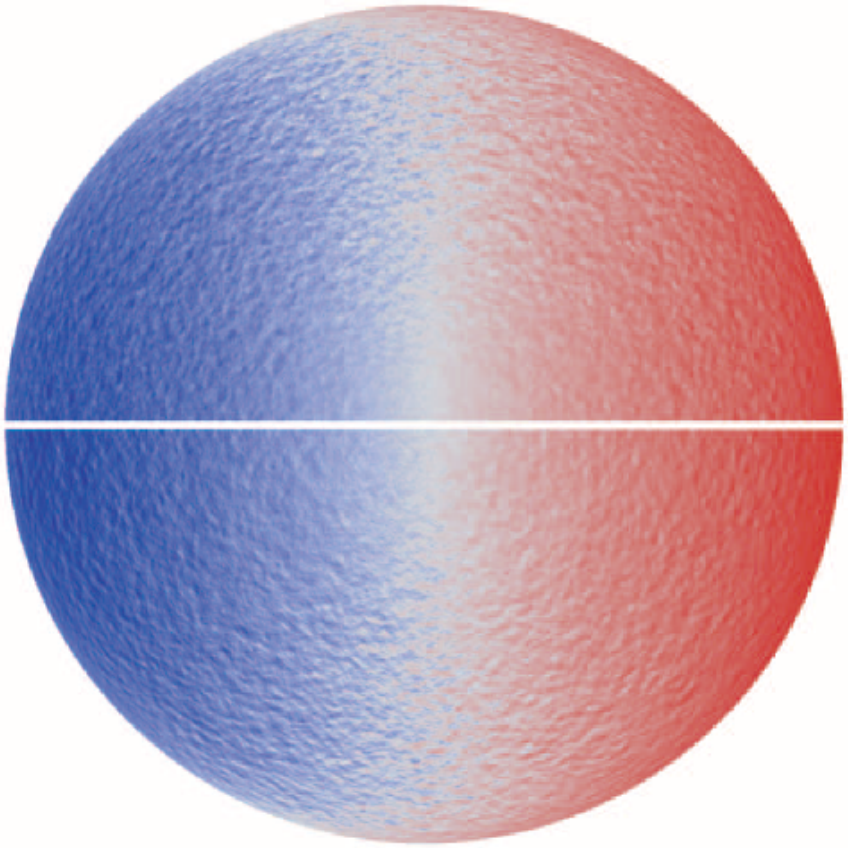

Figure 4.10. Comparison of Doppler velocity images. The top image is derived from real MDI data, while below is an example of a realistic synthetic image produced by the data simulations detailed in this chapter..

for that pixel. This is performed for all image pixels. A wrap around border is added to the Cartesian image map to account for the interpolation process including any pixel that happens to lie outside the map boundaries.

Once this is done, a the convective blue shift is added by considering this velocity component to be third order polynomial for the distance of a point from disk center. A random Gaussian noise element is added if necessary.

Further modulation to the velocity map is performed by considering the reduction of velocities as a function of distance from disk center due to limb darkening using another third order polynomial. Finally the optics of MDI are considered by a final modulation of the image using the Modulation Transfer Function of the instrument. The final image is then saved to disk.

An example of an image produced from this simulation is shown in Fig. 4.10 along with an MDI image for comparison. The similarity is clearly apparent for both large scale and small scale velocity features.

Sequences of images may be produced by looping this process and specifying a time gap between images. This time gap is used to evolve the phases, pertaining to differential rotation and convection cell evolution, that produce the image pattern.

4.4.3 Computational Data Production and Analysis

The code I used to perform the tasks to produce real and synthetic Doppler images, as described in this chapter, were written in Fortran 77. The code listings are given in appendices towards the end of this dissertation. The first flowchart of Appendix A illustrates the process route for `MDI_fake.for` (see first listing of Appendix B) which is the most recent version of a program to produce synthetic images for a solid body interpretation of the solar rotation. The implementation of differential rotation into a spherical harmonic process in depth will be discussed in Chapter 7. The second flowchart of Appendix A illustrates the process route for `MDI_analysis1.for` (see second listing of Appendix B) which analyzes a Doppler image and calculates the spectral coefficients that characterizes the observed axisymmteric flows. The third flowchart of Appendix A illustrates the process route for `MDI_analysis2.for` (see third listing of Appendix B) which uses the spectral coefficients extracted by the previous program to construct velocity data for each axisymmetric flow and subtract it from the original image.

On the High Performance Computer at the University of Texas at Arlington, the approximate running time per image for each process was as follows. Two minutes to produce a synthetic MDI image (`MDI_fake.for`), 0.25 minutes to perform the initial spectral analysis (`mdianalysis1.for`) and 1.5 minutes to remove the unwanted axisymmetric velocity data to produce an image that only includes non-axisymmetric components (`mdianalysis2.for`).

After initializing the necessary parameters, `MDI_fake.for` begins by reading in the MTF array which has been previously created and includes the information required to modulate the synthetic data with the optics of MDI. A limb darkening profile is constructed as previously described, and these two arrays are combined within Fourier space (using the `four1.for` subroutine) to be convolved with the final image.

The subroutine `plmcoef.for` is subsequently run once to calculate the values of C_ℓ^m for all ℓ and m, as in (4.48), to be used in the calculation of the vector velocities V_θ and V_ϕ as seen in (4.50) and (4.51), respectively, along with coefficients, A_ℓ^m and B_ℓ^m, described next. The modified associated Legendre Polynomials, $\overline{P}_\ell^m$, are calculated at each colatitude within the loop to create an image using the `plm.for` subroutine that uses the recurrence relation

$$\overline{P}_\ell^m(\cos\theta) = A_\ell^m \ \cos\theta \ \overline{P}_{\ell-1}^m(\cos\theta) - B_\ell^m \overline{P}_{\ell-2}^m(\cos\theta), \tag{4.52}$$

where

$$A_\ell^m = \left[\frac{(2\ell+1)(2\ell-1)}{(\ell+m)(\ell-m)}\right]^{1/2}, \tag{4.53}$$

and

$$B_\ell^m = \left[\frac{(2\ell+1)(\ell+m-1)(\ell-m-1)}{(2\ell-3)(\ell+m)(\ell-m)}\right]^{1/2}. \tag{4.54}$$

These two coefficients are calculated for all ℓ and m in the previously mentioned `plmcoef.for`. The starting values to be input into the recurrence relation are (see [79] for more detail)

$$\overline{P}_m^m(\cos\theta) = \left[\frac{1}{2}\sum_{\bar{m}=1}^{m}\frac{2\bar{m}+1}{2\bar{m}}\right]^{1/2}, \tag{4.55}$$

and

$$B_\ell^m = \left[\frac{(2\ell+1)(\ell+m-1)(\ell-m-1)}{(2\ell-3)(\ell+m)(\ell-m)}\right]^{1/2}. \tag{4.56}$$

The final image is saved to disk in binary format as opposed to a text file to save on disk space.

The spherical analysis programs `mdi-analysis1.for` and `mdi-analysis2.for` can be used for both real and synthetic data by changing an internal variable. If the programs

are run for synthetic data, solar parameters, such as the solar tilt, `b0`, are defined by the user to correlate with those used in `MDI-FakeNew.for`. If used for real data, solar parameters are read in from the header information for each image file. These include the distance from the Sun in AU (`rdist-au`), the tilt of the solar north pole with respect to the observer (`b0`) the radial, northern and western velocities of the observer with respect to the Sun (`c0`, `cy` and `cx`, respectively) and the image coordinates that determine the center of the Sun (`x0` and `y0`).

The subroutine `vfix.for` uses the solar parameters, notably the observer velocity values, to remove the observer's velocity from the image as seen in Section 4.2.4. This correction is performed according to As these values can be set to zero for the synthetic data analysis, for the sake of ease, this process is more important for real data.

The processes for mapping to heliographic coordinates (`heliomap.for` Section 4.2.5), determining the spectral coefficients for rotation and meridional circulation (`rotation.for` Section 4.2.6 and `mcirc.for` Section 4.2.8, respectively), finding the initial limb shift in polar coordinates (`lshft.for` Section 4.2.7) and the limb shift correction for the meridional circulation (`lshftc.for` Section 4.2.9) are subsequently performed. The calculated spectral coefficients and the respective velocities after the rotation and the limb shift corrections have been made are then written to disk.

These values are then used, along with the original image map, by `mdi-analysis2.for` to remove the axisymmetric flows. The spectral coefficients at each ℓ and m for the non-axisymmetric components are then determined (`plmxform.for` - Section 4.3.1) and their amplitude and phase information written to disk.

These spectral coefficients can be used in subsequent analyses to, for example, calculate the photospheric convection spectrum (Section 4.3.1) and those described later in this dissertation.

CHAPTER 5

THE SUPERROTATION OF SUPERGRANULES

5.1 Background

In Section 4.2.6, the differential rotation profile of the Sun was discussed and that a fourth-order polynomial in the sine of the latitude, ψ, (see equation 4.17 - alternatively, a similar polynomial in the cosine of the colatitude, θ, can be used) with correctly chosen coefficients (A, B, C) provides a good fit. However, this profile is dependent on the observational methods used; using sunspot data or spectroscopic methods results in slightly different profiles. It has been useful, therefore, to further this analysis to study how convection patterns move across the solar disc. Using numerical simulations and helioseismic measurements, Gilman and Foukal [90] and Hathaway [44], respectively, confirmed the idea proposed by Foukal and Jokipii [91] and Foukal [92] that the rotation rate beneath the photosphere should increase due to the conservation of internal angular momentum near surface convective flows.

As different sized convection cells are expected to be anchored at different depths within the convection zone, it is expected that the internal rotation gradient would advect these cells at different rates and thus different rotation rates would be seen over the range of different sized convection cells distributed over the photospheric convection spectrum.

5.1.1 Cross-Correlation Analyses

Characteristics such as those described above were among those found by Duvall [53], who made the first examinations of the equatorial rotation rate of the supergranule Doppler velocity pattern. He produced a regular sequence of Doppler velocity maps over a period of time and cross-correlated these to produce a rotation profile as a function of latitude of the supergranule pattern. He found that the rotation rate was approximately

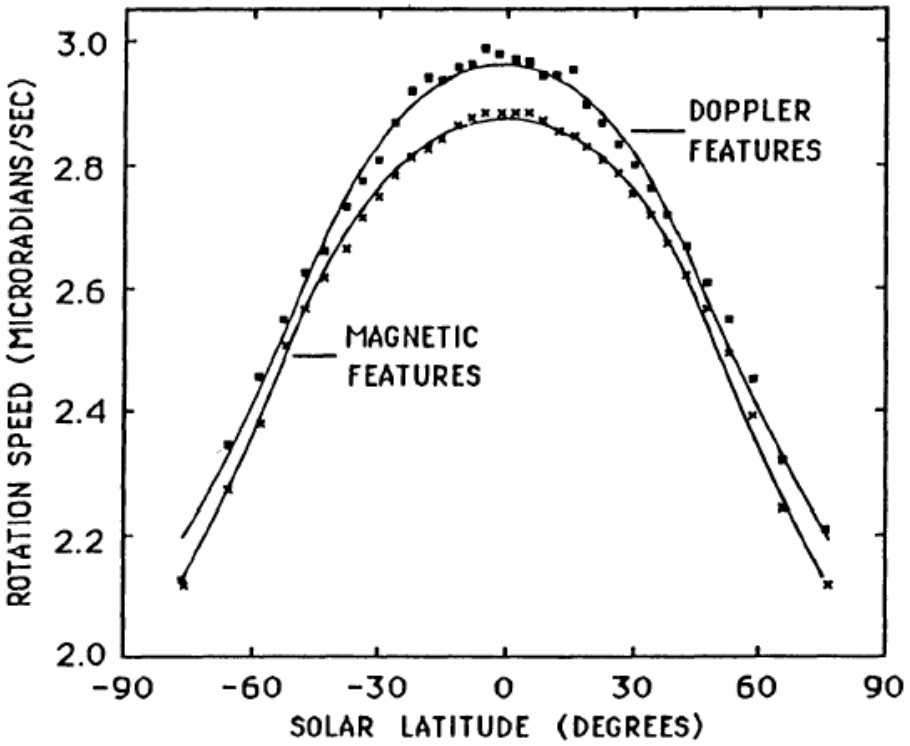

Figure 5.1. Differential rotation profiles for residual Doppler features (upper curve) and magnetic features (lower curve) found from the cross-correlation of Mount Wilson magnetograph observations spaced one day apart [93]. The data points along their respective lines represent the results calculated for each latitude by averaging the correlation amplitudes over the 20 year collection period. The smooth curves are least-squares fits to the data using (4.17).

3% faster than the Carrington rate and that the faster rotation rates were found for larger time differences between the correlated pairs. The latter suggested that larger-sized, longer-lasting cells that extend deeper into the convection zone should rotate faster than their short-lived, smaller-sized counterparts produced nearer the photosphere. Further, analysis of the rotation rate of different sized cells can act as a tracer into the radial differential rotation profile beneath the photosphere.

Snodgrass and Ulrich [93] followed similar methods to Duvall's [53] and were able to confirm his results with the added conclusion that the supergranule pattern also exhibits a latitudinal profile (Fig. 5.1), with the higher rotation rate being maintained throughout.

5.1.2 Fourier Analysis

Another method to study the rotation of the convection pattern is to Fourier analyze a time series of Doppler images. Beck and Schou [94] averaged over six 10-day MDI full-disk dopplergrams to construct a data cube of the supergranule pattern in the sine of the latitude, $\sin(\psi)$, longitude, ϕ, and time, t. They Fourier transformed this data cube in time and longitude to produce a power spectrum as a function of $\sin(\psi)$, spherical harmonic order, m, and frequency, ν. Cuts through the transformed cube in m and $\sin(\psi)$ produced rotational frequency plots in $\sin(\psi)$ and m respectively. They used their results to infer the equatorial rotation rate, averaging latitudes $\pm 9^\circ$ around the equator, as a function of m. This showed that their results were consistent with those produced by Duvall [53] and Snodgrass and Ulrich [93] in that larger-scale features exhibit higher rotation rates. They also produced rotation rates as a function of latitude for various ranges of m, which reflected previous observations of a differential rotation profile in $\sin^2(\psi)$ and the equatorial rotation rate as a function of m. Further analyses used results of a regularized least-squares rotation inversion Schou et al. [14] to compare the supergranule rotation rate measured by MDI with rotation rates at different depths in the outer 10% of the convection zone. These analyses showed evidence that the supergranule rotation rate is somewhat greater than the depths at which the supergranules were thought to be formed. They concluded that either supergranules are formed deeper within the convection zone than previously thought or that they genuinely rotate faster then the underlying plasma. They provide one suggestion to answer the superrotation problem, in that supergranules are not purely convective and waves may play a role in supergranule formation and are carried in a prograde direction, thus rotating faster than the surrounding plasma. This wave characteristic was investigated further by Gizon et al. [55] and Schou [59]. Gizon et al. [55] used the same 60-day sequence of MDI Doppler velocity images as Beck & Schou [94]. They used time-distance helioseismology methods [95] to obtain a 120×120 map of the horizontal divergence of flows 1 Mm below the photosphere with a 12 hour cadence. They produced a power spectrum of the supergranulation signal near the solar equator

and found both prograde and retrograde components of temporal frequency. With the former being much stronger than the latter, they suggested that the extra prograde signal was due to wave propagation of the supergranule pattern. The prograde flow was found to be similar in magnitude to the rotation rate of magnetic features coupled to supergranulation [82] but faster than the underlying photospheric rotation as studied by Snodgrass and Ulrich [93]. Schou [59] confirmed these findings while additionally observing that the same superrotation phenomenon is found at non-equatorial latitudes. Whereas these studies promote an observed superrotation of the supergranule pattern due to wave phenomena producing an excess prograde propagation of supergranules, in what follows, we suggest that projection effects in the line of sight Doppler velocity pattern produce most, if not all, of the observed excess superrotation [96].

5.2 Our Research into the Superrotation Phenomenon

The studies of MDI data produce an observed superrotation of the supergranule pattern. Beck and Schou [94] and Schou [59] attribute this phenomenon to an underlying wave that carries the supergranule signal along with it, producing an excess prograde propagation of supergranules. However, we hypothesize that projection effects within the line-of-sight Doppler velocity pattern produce most, if not all, of the observed excess superrotation [96]. In the following, I describe our studies of supergranule superrotation using synthetic data including no wave-like phenomena whatsoever. The flowchart, with relevant program names, illustrating the order of the work we carried out for this research is shown in the first chart of Appendix C.

5.2.1 Data Preparation

The first step is to produce a synthetic convection spectrum from which the spectral coefficients, needed to produce the simulated line of sight Doppler velocities (Eqns. 4.33-4.36), can be extracted. This is described in Section 4.4.1, using a two component spectrum representing supergranules and granules centered on $\ell \sim 100$ and $\ell \sim 4000$

respectively. This produced a spectrum similar to that produced from MDI data that was used by Beck and Schou [94] in their analyses. The simulation to produce the synthetic MDI Doppler velocity maps was simplified to consider only solid body rotation of the Sun at a rate of 14.50° per day or 466 nHz. This was done to study whether latitudinal projection effects would also come into play without being buried beneath any profile produced by differential rotation. A further simplification was made by neglecting any evolution of the supergranule pattern.

A series of these Doppler maps was produced at a 15 minute cadence over a period of 30 days, giving three 10-day series similar to the six used by Beck & Schou [94]. Each map underwent removal of Doppler signals due to rotation, meridional circulation and convective blueshift as described earlier (see Section 4.2 and subsections therein). The resultant data was analyzed in two ways: cross-correlation of latitudinal strips of maps separated by a given time lag, similar to that done by Duvall [53] and Snodgrass and Ulrich [93] and a two-dimensional Fourier analysis similar to that performed by Beck and Schou [94].

5.2.2 Cross-Correlation Analyses

To perform the cross-correlation analysis, spatial spectra were derived from the Doppler maps produced by the data simulation. These spectra were then filtered using Gaussian profiles in $\log(\ell)$ centered at ℓ = 32, 64, 128, 256 and 512. These were then inversely transformed and remapped to heliographic coordinates. The results were sets of Doppler maps featuring patterns over a range of sizes, dependent on the filter width, centered at wavenumbers listed previously ($\ell \sim 128$ being most suitable for supergranules). The rotation rates were found by cross-correlating data strips (about 1.75° in latitude and 105° in longitude) for a given latitude position between two pair of images separated by a time lag of 8 hours. The cross-correlation peak was fit with a truncated cosine function to extract the strongest cross-correlation coefficient which is used to calculate the longitude shift. This shift is then divided by the time-lag resulting in the rotation ve-

locity. This cross-correlation process was repeated for each filtered map over the range of feature sizes listed. Sets of rotation profiles, rotation rate versus latitude, were produced for the set of spatial sizes and are shown in the next subsection.

5.2.3 Fourier Analysis

To perform the two-dimensional Fourier analysis, every image within each of the three ten day series was apodized with a cosine function between 90-95% from disk center, then remapped to heliographic coordinates. Longitudinal strips of data covering 9 latitudinal degrees of the equator underwent a spatial transformation in longitude and the resultant Fourier coefficients were temporally transformed over the ten day data range. This produced a set of power spectra in time and space, the peaks for which were determined from their center of gravity using a window about 60 nHz wide about the peak. A plot of rotation rate versus the longitudinal wavenumber, m, was be produced and is described in the next section.

5.3 Results

Fig. 5.2 shows the rotation profile for a set of different spatial sizes at a single time-lag of 8 hours. It can be seen that a latitudinal profile exists despite a solid body rotation profile, thus displaying evidence of the existence of superrotation die to projection effects. The results of Duvall [53] are reflected with larger features having larger rotation rates. Functional forms of these profiles decreasing like $\sin^2(\psi)$ are included. The largest features have a rotation rate above 1% of the imposed 14.50° per day. Although smaller features rotate much slower, they are also seen to rotate faster than the imposed rate.

Fig. 5.3 shows the result of the two-dimensional Fourier analysis, plotting equatorial rotation rate versus longitudinal wavenumber, m. This plot (solid line) is seen to drop rapidly for increasing wavenumber from around 14 nHz at $m \sim 20$ to 2 nHz at $m \sim 100$, before leveling out at higher wavenumbers, around 1 nHz at $m > 200$. A functional

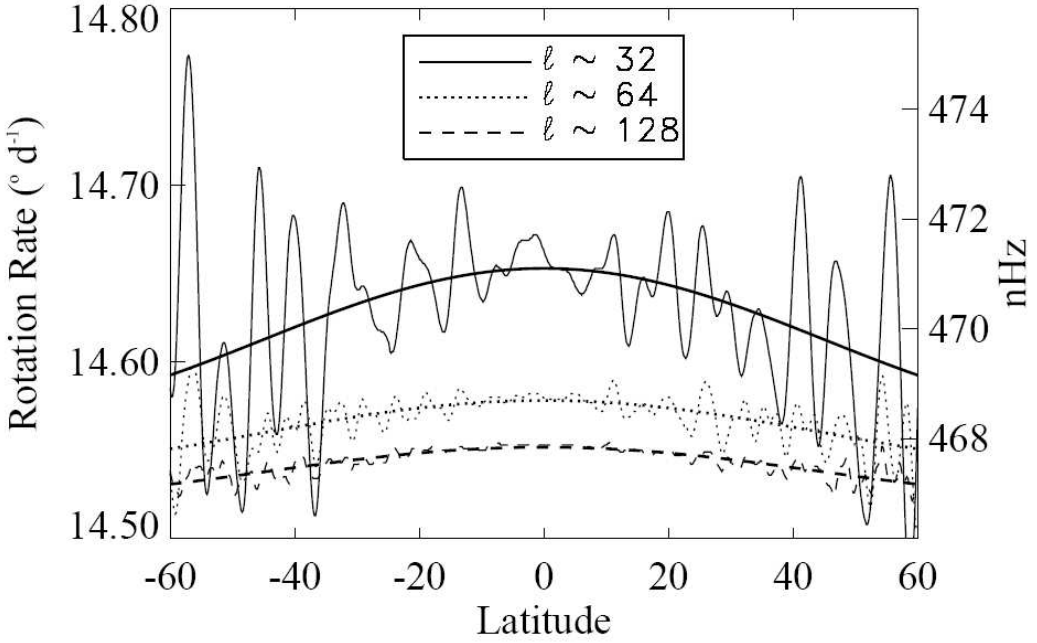

Figure 5.2. The rotation rates as functions of latitude from the cross-correlation study are plotted for Doppler features of three different sizes for a time-lag of 8 hours [96]. The largest features ($\ell \sim 32$, shown as solid lines) appear to rotate about 1% faster at the equator than the 14.50 degrees per day that was imposed. Smaller features ($\ell \sim 64$, dotted lines, and $\ell \sim 128$, dashed lines) appear to rotate somewhat more slowly but still at a rate faster than that imposed on the vector velocity pattern.

form to this profile is included (dashed line). Again, the rotation rate for the full range of spatial sizes is found to be greater than the imposed solid body rotation rate (solid straight line). The plot is found to be very similar to that produced by Beck & Schou [94] at wavenumbers, $m < 100$. The asymptotic behavior at higher wavenumbers in Fig. 5.3 is due to a lack of resolution in the rotation rates at higher wavenumbers, i.e. higher wavenumber features seem to rotate at similar rates.

5.4 Discussion

We have been able to produce a Doppler velocity pattern that rotates faster than the rate imposed in producing the vector patterns for scales at and around those typical for supergranulation. As opposed to the wavelike phenomenon to explain the similar results produced by Beck & Schou [94], our simulations produce results that allow us to

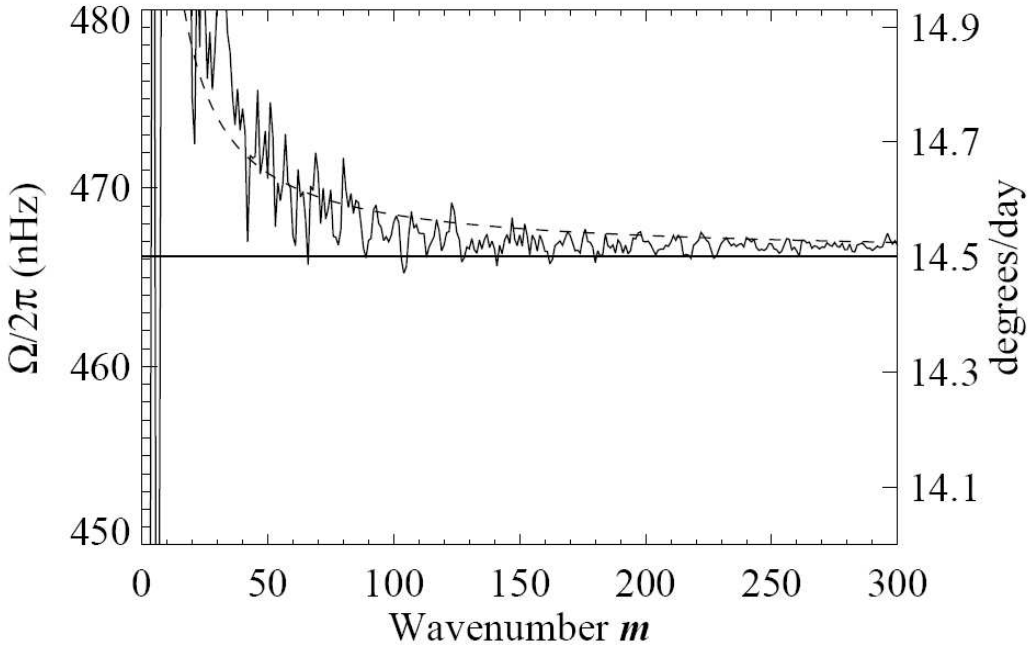

Figure 5.3. The equatorial rotation rate from the 2D Fourier analysis study is plotted as a function of longitudinal wavenumber [96]. The rotation rate is faster than the imposed rate at all wavenumbers and increases rapidly at wavenumbers less than ~ 100. The increase is about 2 nHz at $m \sim 100$, 5 nHz at $m \sim 50$, and more than 14 nHz at $m < 20$. An approximate functional form is shown with the dashed line.

conclude that the superrotation is a result of projecting the vector velocities onto the line of sight, a simple explanation of which is shown in the following example. Using a simplified version of Eqn. 4.33 so that we consider a signal at the equator ($\theta = \pi/2$) while neglecting the solar tilt of the north pole ($B_0 = 0$), we have for the vector velocities

$$V_{los}\left(\frac{\pi}{2}, \phi\right) = V_r\left(\frac{\pi}{2}, \phi\right)\cos\phi + V_\phi\left(\frac{\pi}{2}, \phi\right)\sin\phi. \tag{5.1}$$

This can be simplified by neglecting any radial flow and using a longitudinal velocity which varies sinusoidally to exhibit an underlying Doppler velocity pattern with wavenumber m rotating with an angular velocity Ω, giving

$$V_\phi\left(\frac{\pi}{2}, \phi, t\right) = A\sin[m(\phi - \Omega t)]. \tag{5.2}$$

However, when we come to project this pattern onto the line of sight, the process also includes a sin ϕ modulation factor (Eqn. 5.1) as well as window and apodization

functions. The original velocity vector pattern and the result after projecting onto the line-of-sight is shown in Fig. 5.4. The peaks in the line-of-sight Doppler pattern are pushed away from those of the original pattern due to the sin ϕ modulation factor. This results in a longer translation longitudinally of the Doppler pattern (the pattern tends to have further to travel) which is used in the cross-correlation analysis. As the pattern seems to cover a larger distance than the velocity vector pattern for a given correlation lag time, the Doppler pattern seems to travel faster and so a faster rotation rate results. This shifting is stronger at smaller wavenumbers. The modulation, windowing and apodization culminate in producing a Doppler velocity signal with a wavenumber of 0.5 higher than before, which is seen by the additional half-wavelength near the central meridian in Fig. 5.4. The phase velocities are thus increased by

$$\Omega' \simeq \frac{m' + 0.5}{m'}\Omega. \tag{5.3}$$

A functional form seen to fit the two-dimensional Fourier analysis results shown in Fig. 5.3.

5.5 Concluding Remarks and Future Work

We have found that using a simplified model of a non-evolving convection pattern produced from a synthetic photospheric convection spectrum and by imposing a solid body rotation rate to the pattern, we find a latitudinal-dependent superrotation of the pattern. The superrotation rate increases with increasing wavenumber. The strength of this superrotation, when analyzed using cross-correlation methods, is slightly less than that found by Duvall [53] and Snodgrass and Ulrich [93], which we assume is due to the simplification of our model. Including differential rotation and letting the pattern evolve should produce even better results with higher rotation rates.

We also produce similar results to Beck and Schou [94] when applying a two-dimensional Fourier analysis to our data. We get very good correspondence at wavenum-

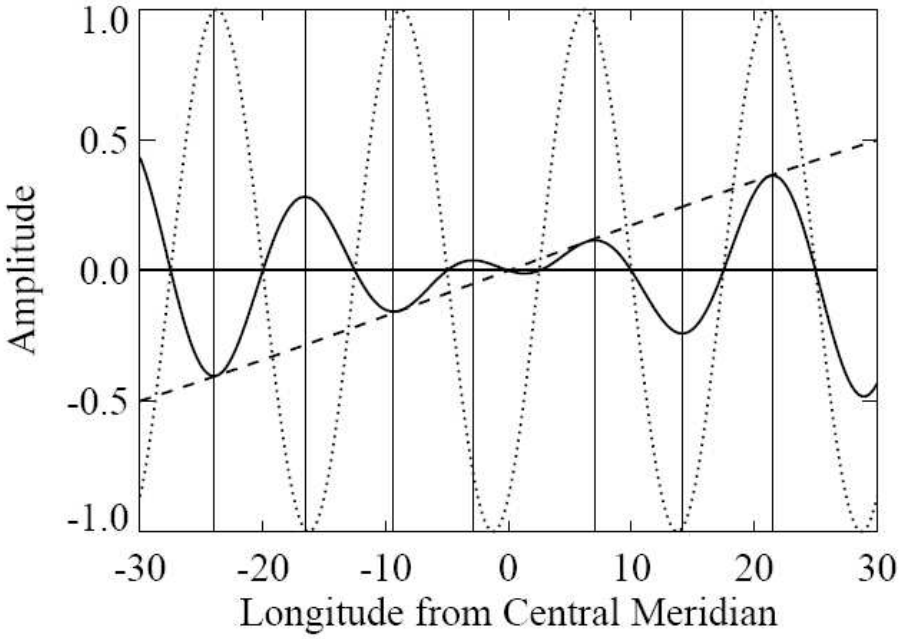

Figure 5.4. The Doppler signal (solid line) derived from a sinusoidal vector velocity (dotted line) multiplied by the line-of-sight projection function sin ϕ (dashed line) [96]. The peaks in the Doppler signal (marked by thin vertical lines) are shifted away from disk center relative to the positions of the peaks in the underlying vector velocity pattern. As the underlying vector velocity pattern translates in longitude the Doppler velocity pattern appears to move through a larger range of longitudes thereby giving the Doppler velocity pattern a more rapid rotation rate. Note also the appearance of an additional half-cycle in the Doppler signal near the central meridian.

bers below $m \sim 100$, although we do not yet produce a continual decrease in rotation rate above this value.

We have shown that we can, on the whole, reproduce the findings of Duvall [53], Snodgrass and Ulrich [93] and Beck and Schou [94]. Although subsequent analysis by Gizon et al. [55] and Schou [59] suggest wave propagation to be the main factor behind the superrotation, we find this phenomenon can be produced from a model which includes no wavelike properties whatsoever. Although the projection effects probably account for the vast majority of the superrotation, further results and analyses produced by Gizon et al. [55] and Schou [59] find other wavelike properties of supergranulation that have not been accounted for in our studies and therefore cannot be described by projection effects. We hypothsize, however, that these additional wavelike properties can be attributed to

the advection of supergranules by larger-scale, non-axisymmetric flows, such as giant cells. This idea is investigated in Chapter 8.

Our studies can be extended by including large scale dynamical flow due to differential rotation. Convection features of a given size are expected to extend below the surface and be anchored at a depth specific to their surface size. To a first order approximation, it can be assumed that the depth is on the order of their surface size. As their surface size can be described in wavenumbers, then the depth to which they extend can similarly be defined. As seen in Section 6.2, the internal rotation profile is a factor not only of latitude, but also of depth. It follows, therefore, that convection features of different wavenumber rotate at different rates. Using this characteristic means that our studies of superrotation can be extended using the differential rotation algorithms described later in Section 6.1. This should alter the profile seen in Fig. 5.3, removing the asymptotic nature and match such profiles achieve from earlier work using MDI data [94].

CHAPTER 6

SOLAR ROSSBY WAVE "HILLS" IDENTIFIED AS SUPERGRANULES

6.1 Introduction

6.1.1 The Shape of the Solar Limb

It is well known that the shape of the Sun is slightly non-spherical, its oblate shape exhibiting bulging at the equator and flattening at the poles due to rotation [56]. Observations using the MDI [68] and RHESSI [97] instruments both provide up to date evidence of this oblateness. More detailed studies of the collected data [57],[58] reveal further variations in the shape of the solar limb, with evidence for small scale 'hills' on the surface. These hills have been characterised as being 100 m high (height above the mean photospheric surface) and uniformly spaced over the solar surface by around 90,000 km, thought to be a manifestation of solar Rossby waves [58].

6.1.2 Rossby Waves

Rossby waves (inertial waves whose restoring force is the latitude-dependent strength of the Coriolis force [98], [99]) were first proposed [100], [101] to operate in the interior of the Sun. It was suggested that these waves contribute to a magnetohydrodynamic dynamo that produces solar magnetic fields, including their periodic polarity reversals. Rossby waves could also be important in maintaining the structure of the Sun's differential rotation [102], [103], [104]. These theoretical studies suggest that Rossby waves may be connected to a large array of phenomena such as the solar surface structure, the Sun's magnetic cycle, the initiation and propagation of magnetic waves, and the dynamics of the solar atmospheric environment responsible for "space weather". It has been argued that similar effects also exist in other stars [105] and gaseous giant planets [106]. Rossby

waves were previously observed in the Earth's oceans [107],[108] and atmosphere [109] as low-amplitude long wavelength features.

6.1.3 The Discovery of Solar Rossby Waves?

In their discovery of the Rossby wave 'hills', Kuhn et al. [58] argued against the possibility that these hills were produced by supergranulation. The radial flows in typical supergranules [86], as mentioned in Section 4.3.2, should produce a series of bumps on the surface of the Sun but Kuhn et al. [58] argue that the spacing would be too close and that the random forcing of these flows would not produce the spectral signatures they see. However, our results seem to indicate [110] that hills on the solar surface produced by supergranules largely reproduce the spectral features attributed to Rossby waves.

The following sections describe my analysis of the signals produced from synthetic Doppler maps that match those derived from observations [58] despite containing no wavelike properties whatsoever. The flowchart, with relevant program names, illustrating the order of the work carried out for this research is shown in the second chart of Appendix C.

6.2 Data Preparation and Results

6.2.1 Producing Surface Height Data

Photospheric velocity data are produced using the methods described in Section 4.4 [79]. The radial component of the velocity field produces variations in photospheric heights which are then analyzed in a manner equivalent to that employed by Kuhn et al. [58] in their analysis of the solar hills seen at the limb.

The spectral coefficients for the radial velocity, R_ℓ^m (Eqn. 4.37), are converted to spectral coefficients for height by dividing the velocity amplitude by the square root of the wavenumber, ℓ. This relation is adapted from the theory for up-flowing gas forming a 'forced plume' subject to buoyancy with mass flux and momentum conservation [111]. Realistic numerical models for solar granulation [31] indicate that these smaller convective

features have diameters of about 1000 km, radial velocities of about 3000 m s^{-1}, and produce surface height variations of about 30 km. These granular parameters can be scaled using the forced plume model to determine supergranule height variations, an operation derived from mass conservation. Using the characteristic size (30,000 km) and radial velocities (30 m s^{-1}) for supergranules indicates that supergranules should produce 'hills' with heights of about 2 km. This is more than an order of magnitude larger than the estimate reported by [58] and may reflect on differences in driving mechanisims for granules and supergranules. However, the actual size of the hills is not what is important here. The spectral features identified by [58] are temporal signatures associated with the rate at which these hills rotate into view over the limb.

6.2.2 Constructing Time Series of Limb Heights

Height maps of 4096×1024 elements (longitude by latitude) are produced, representing the full solar surface in a similar manner to how the Doppler velocity maps had been produced in previous studies [35], [79], [86], [96]. Two latitudinal pixel columns separated by 2048 longitude pixels (i.e. meridional columns separated by 180° in longitude) are extracted from the height map array. These columns are reallocated into a single one-dimensional array representing the limb heights all the way around the Sun starting from the western solar limb and proceeding counter-clockwise through north. The center of the right-hand column represents the western limb, and the data north of that represent the northwestern limb (ending at the north pole). The data from the left-hand column are joined on (north to south) representing the eastern limb then the remainder of the first column is joined onto that (south pole to western limb). This is repeated for each time step (a solar rotation/4096) by stepping through the entire height map one longitude step at a time. (Note that halfway through the extraction, the western limb data column wraps around back to the far left of the map.) These limb height strips are combined into a two-dimensional array, so they represent a time-series of limb height data around the solar limb for each 9 minute time interval, or conversely, a time-series of

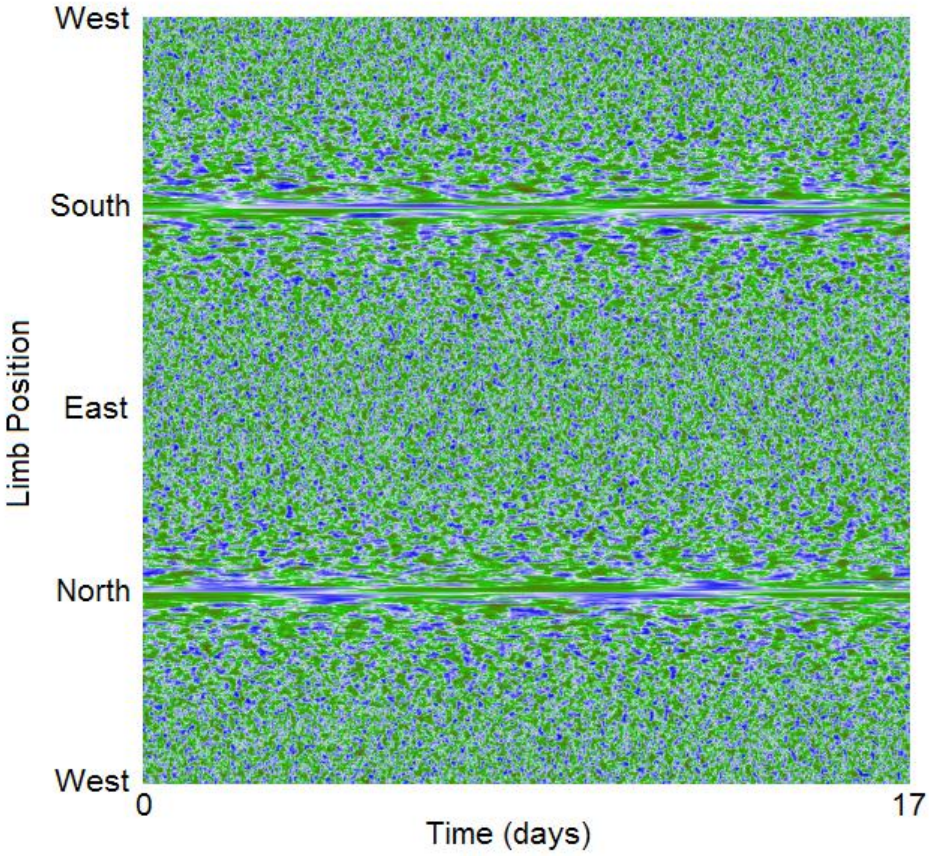

Figure 6.1. A sample data set of a timeseries lasting 17 days sampled at a cadence of 9 minutes illustrating the variation of heights within convection cells around the solar limb. The data is sampled approximately every 5.7 degrees beginning from the western limb at the top and progressing clockwise around the limb. Green points relate to raised material, blue points to sunken material relative to a zero point defined by material that is neither rising nor falling.

limb height data at particular positions around the limb over one whole 27-day rotation sampled at a cadence of 9 minutes (Fig. 6.1). A set of thirty such 27-day time-series are produced, analyzed, and averaged for the purposes of noise reduction. Note that these simulations do not include differential rotation — the patterns from which the limbs heights are extracted rotate rigidly.

Additional data sets are produced representing limb heights over 34 days for evolving supergranule patterns. The patterns are evolved by adding random changes in phase to the spectral coefficients, while holding the amplitudes fixed, and accumulating these

over time. Applying the same cross-correlation methods employed by Duvall (1980) [53] and Snodgrass & Ulrich (1990) [93] to the simulated data produces supergranule lifetimes on the order of a day, coinciding with what is seen in solar data [53], and thereby removing any long-range coherence in the time-series which was a prior argument against the supergranule nature of the hills [58]. These data are then reformatted into 34 day time-series with a 12 minute cadence (matching the cadence used by Kuhn et al. (2000) [58]).

6.2.3 Limb Height Data Analysis

Each limb-strip is convolved with a 4 pixel wide filter and the data sampled every fourth pixel, to create 512 limb position bins similar to those produced by Kuhn et al. (2000) [58]. Taking the FFT of each of these 512 pixel spatial strips produces a spatial spectrum for each time sample. Subsequent sampling along the time strips and taking the FFT of each strip similarly produces a temporal spectrum for each spatial frequency. This results in two-dimensional arrays which are the 2-D FFT of the original spatial-temporal data. Multiplying these 2-D FFT arrays by their complex conjugate gives power spectra for the limb height over a range of spatial and temporal frequencies. The power spectra are summed over all spatial frequencies ($\ell = 1$ to 255) and then multiplied by the temporal frequency to produce the spectra shown in Fig. 6.2. It is clearly seen that an excess of power is present at a frequency of around 50 μHz (slightly higher than the frequency of the peak seen by Kuhn et al. (2000) [58]). This feature is produced by the supergranules in our simulation. The smaller granules are not well resolved in SOHO/MDI data after its subsequent smoothing and re-sampling to get data at 512 limb positions.

The simulated data can also be used to produce temporal spectra of the limb signal as a function of limb position angle using a process similar to that of Kuhn et al. (2000) [58]. The data are smoothed in the spatial direction with a 256 bin running mean and in the temporal direction with an 8.3 day running mean, and the residual between

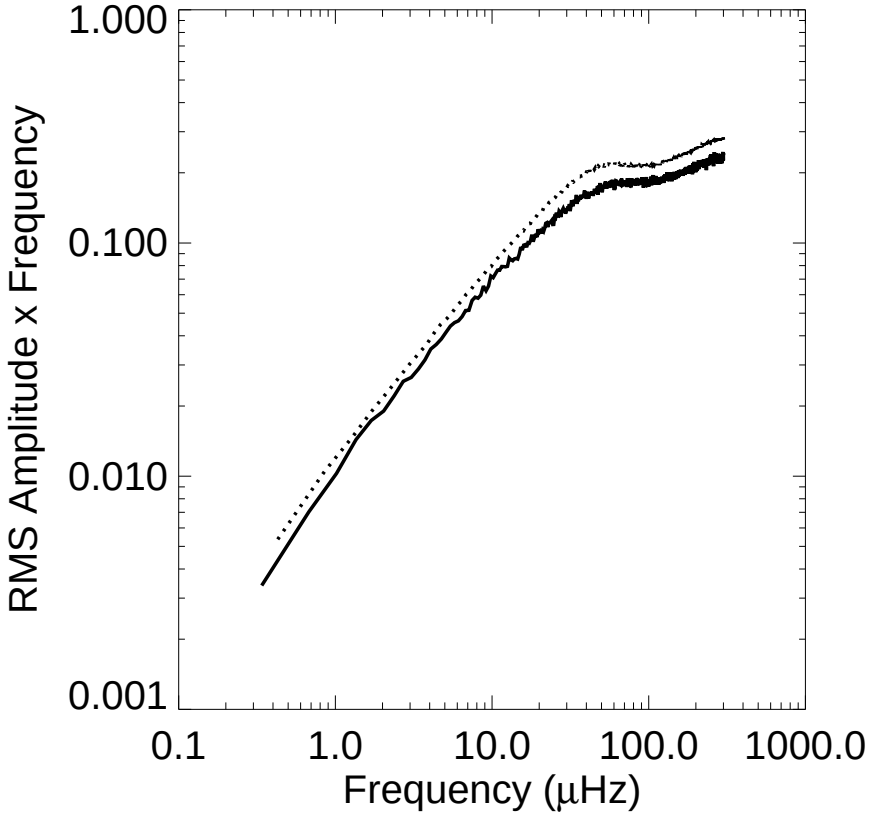

Figure 6.2. Power spectrum [110] created by taking the spatial and temporal FFTs of the limb height time series summed over wavenumber ℓ and rescaled to similarly represent the plot constructed by Kuhn et al. (2000) [58]. The solid line is the average from three evolving supergranule simulations. The dotted line is the average from 30 non-evolving supergranule simulations. The excess of signal seen as a bump at a frequency of around 50 μHz is in good agreement with, but somewhat higher than, that seen by Kuhn et al. (2000) [58].

the smoothed and original data calculated. The temporal FFT of this residual power spectrum is taken at each limb position and smoothed with a 4 pixel bin running mean for the 27 (or 34 in the case of the evolving pattern) day data stream (corresponding to the 88 pixel bin running mean over the 800 day sequence used by Kuhn et al. (2000) [58]). Multiplying this result with its complex conjugate produces temporal power spectra which can be plotted against position angle, as shown in Fig. 6.3. A 'sawtooth' pattern is seen, similar to that produced by Kuhn et al. (2000) [58], with the maximum and minimum frequencies occurring at the equator and the poles, respectively.

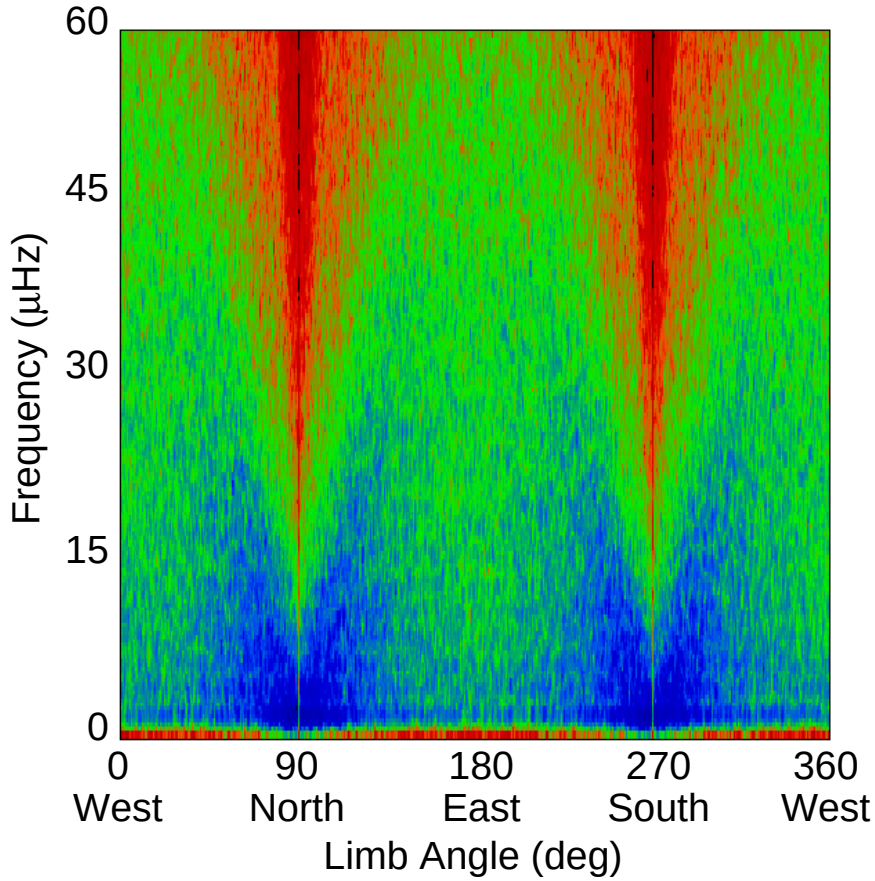

Figure 6.3. Average power spectrum from three evolving flow pattern data for a range of temporal frequencies at each angular position around the limb [110]. The signal strength increases logarithmically as color changes from red to green to blue. The result is a near sawtooth distribution of excess power, similar to that found by Kuhn et al. (2000) [58]. This illustrates that by distributing similarly sized features over a rotating sphere, features at the equator are more numerous and pass over the limb more frequently than at the poles.

The temporal power spectra at each limb position are stretched in proportion to the linear speed of rotation at the corresponding latitudes so that the maximum for each limb angle now lies along the frequency of maximum power at the solar equator instead of distributed along the sawtooth pattern. The power spectra are then averaged over all limb angles and plotted against the temporal frequency (Fig. 6.4). The non-evolving supergranule patterns give a peak near 30 μHz while the evolving supergranule patterns have reduced power with a peak near 15 μHz – almost identical to the frequency obtained by Kuhn et al. (2000) [58].

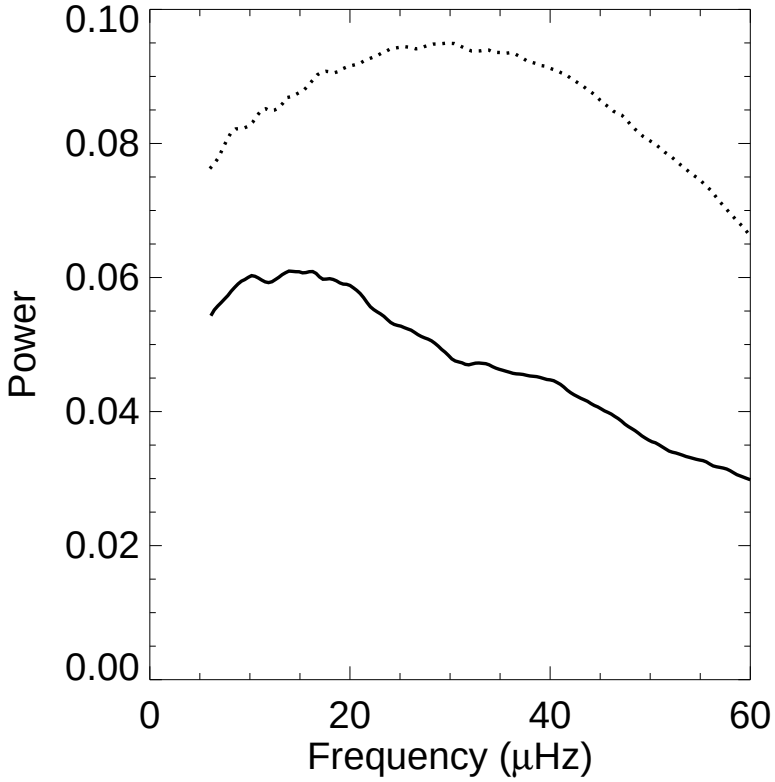

Figure 6.4. Spectral data from which Fig. 4 is produced are stretched for each limb position in proportion to its linear rotation velocity relative to that of the equator [110]. Those data are then averaged over each temporal frequency bin and smoothed. The results for the 30 nonevolving supergranule simulations display a peak near 30 μHz as shown by the dotted line. The results for the three evolving supergranule simulations display a peak near 15 μHz as shown by the solid line. This spectral peak is similar to that found by Kuhn et al. (2000) [58] from SOHO/MDI data.

6.3 Summary

This work has explored the nature of 'hills' observed on the solar surface which had previously been attributed to Rossby waves. The solar hills phenomenon is investigated by analyzing the output from a synthetic model based solely on the observed solar photospheric convection spectrum [35], [86]. We show that the characteristics of these hills can largely be reproduced by the corrugation of the surface due to the radial flows of the convection. The hills in our simulations are dominated by supergranules, a well-known component of the solar convection spectrum. This result is in disagreement with the conclusion by Kuhn et al. (2000) [58] that these spectral features cannot be produced by supergranules. Although the 2 km heights we derived by means of mass

conservation within a forced plume model may be an overestimation owing to the model's simplicity, the observed spectral features presented in Figs. 6.2 to 6.4 are independent of the actual height of the hills and closely match the spectral features seen by Kuhn et al. (2000) [58]. The small differences in the shapes and positions of the spectral features are probably due to the simplifications within our model; we do not include differential rotation of the pattern and the method used to evolve the pattern is purely statistical without regard for the surrounding flows or magnetic elements. The signatures that lead to our conclusions are produced from a spherical harmonic simulation of the photospheric Doppler velocity field based on a convection spectrum containing only supergranule and granule components. No wave phenomena whatsoever are included.

Our results indicate that what have been detected are 'hills' due to supergranulation. Our model was run and the resulting data subsequently analyzed for three different scenarios — both spectral components, as described above, granulation only and supergranulation only. On removing the supergranulation, it is found that despite the spectral overlap of the supergranule and granule components, the excess power features as seen in Figs. 6.2 and 6.4 disappear, thus granulation cannot be responsible for the observed signal as expected from the small size of these features. However, the feature reappears for the spectrum containing only the supergranulation component. Thus we conclude that the signal previously attributed to Rossby waves is most likely due to supergranulation. On comparing our results to the observations of Kuhn et al. (2000) [58], we envision that the latter have provided an independent technique for characterizing supergranules, which may harbor future research potential.

6.4 Outlook

In a recent paper, Kaladze & Wu (2006) [112] used the results of Kuhn et al. (2000) [58] to explain the hill phenomena in the context of Rossby waves. As these observations can now be explained by supergranulation, it can be concluded that Kaladze & Wu [112] attempted to base their model on what turns out to be supergranule features. It

is conceivable that what their model describes are indeed underlying features not yet detected on the Sun, but at most this work is deemed speculative and not backed up by unequivocal observational data.

Direct observational evidence of solar Rossby waves are still yet to be confirmed. While our work presented in this Letter concludes that the signals reported by Kuhn et al. (2000) [58] are explained by supergranulation, there may yet be Rossby wave signatures still hidden within the observational data reported by [57]. Data collected by the RHESSI instrument [97] as reported by Fivian et al. (2005) [113] may also contain Rossby wave signatures. Both sets of data, however, would require the necessary filtering, including the removal of the supergranulation signal, to extract any signals pertaining to Rossby waves.

By extending the data simulation to include differential rotation, as described in the following chapter, new analyses may be performed that are expected to bring the peak seen in Fig. 6.2 considerably closer to the frequency found by the studies of Kuhn et al. (2000) [58].

CHAPTER 7

EXTENDING THE DATA SIMULATION

7.1 Modeling Large-Scale Flows

Thus far, although realistic Doppler images have been produced that match those derived from MDI data (Fig. 4.10), there exists no dynamic link between the images produced within any given timeseries apart from a simple evolution of the spectral coefficient phases has been applied to model solid body rotation. Evolution of the convection cells is performed by changing the phases of the spectral coefficients which changes the pattern over time according to a benchmark setting of around 48 hours for cells of around $\ell = 100$ to change dramtically so that image correlation coefficients of these patterns over time drastically reduces over that time. This setting corresponds to the lifetime of supergranules having a lifetime of around 2 days. Further, although Doppler velocity profiles of large scale flows such as differential rotation and meridional circulation are modeled and mapped to the images, the dynamics of these flows and their subsequent influence on the smaller scale convection cells are not included.

To make the data simulations more realistic, the dynamics of large scale flows can be included. What follows is a description of how the spectral coefficients should evolve to correctly modeled an observed surface differential profile as described by Eq. (4.17) in Section 4.2.6.

7.1.1 Modeling Solar Differential Rotation

To provide a realistic, dynamical flow such as differential rotation, we must begin with a relevant physical relation, namely the three-dimensional momentum equation

$$\frac{\partial \vec{u}}{\partial t} + (\vec{v} \cdot \vec{\nabla})\vec{u} = 0, \tag{7.1}$$

where $\vec{u}$ is the velocity of our flow field of interest, $\vec{v}$ is the velocity profile of the differential rotation flow and the partial derivative is taken with respect to time. Note that no other external forces, such as gravity, are included in this study and thus do not appear in this version of the momentum equation. Differential rotation is only longitudinal in direction with latitudinal dependence, namely

$$v_\phi(\theta) = R\ \sin\theta\ \Omega(\theta), \tag{7.2}$$

with R being the radius at which the rotation profile is measured, in this case the solar surface and Ω being the rotation profile as a function of colatitude, θ. Expanding the dot product of 7.1 and keeping the longitudinal term only results, after relevant cancellations, in

$$\frac{\partial \vec{u}}{\partial t} = -\Omega(\theta)\frac{\partial \vec{u}}{\partial \phi}. \tag{7.3}$$

The evolution of the three spectral coefficients can be found independently, so this example provide the evolution of the radial coefficient describing the radial flow field given by 4.49. Inserting this into both sides of 7.3 gives

$$\sum_{\ell=0}^{\ell_{max}}\sum_{m=-\ell}^{\ell}\frac{\partial R_\ell^m}{\partial t}\overline{P}_\ell^m(\theta)e^{im\phi} = -\Omega(\theta)\sum_{\ell=0}^{\ell_{max}}\sum_{m=-\ell}^{\ell} imR_\ell^m\overline{P}_\ell^m(\theta)e^{im\phi}, \tag{7.4}$$

where the ϕ derivative of the relevant term has been performed.

Normalization of both sides with respect to ϕ can then be made giving

$$\sum_{\ell=m}^{\ell_{max}}\frac{\partial R_\ell^m}{\partial t}\overline{P}_\ell^m(\theta) = -im\Omega(\theta)\sum_{\ell=m}^{\ell_{max}} R_\ell^m\overline{P}_\ell^m(\theta), \tag{7.5}$$

followed by a similar normalization of both sides with respect to θ which results in

$$\frac{\partial R_\ell^{m'}}{\partial t} = -im\int_{-1}^{1}\Omega(\theta)\overline{P}_{\ell'}^m(\theta)\sum_{\ell=m}^{\ell_{max}} R_\ell^m\overline{P}_\ell^m(\theta)d\cos\theta, \tag{7.6}$$

where the normalization of the left hand side has been carried out. Using the fourth-order polynomial in colatitude as laid out in (4.17) and letting x=cos(θ) gives

$$\begin{aligned}\frac{\partial R_{\ell'}^m}{\partial t} &= -imAR_{\ell'}^m \\ &- imB\sum_{\ell=m}^{\ell_{max}} R_\ell^m\int_{-1}^{1}\overline{P}_{\ell'}^m(\theta)\overline{P}_\ell^m(\theta)x^2dx \\ &- imC\sum_{\ell=m}^{\ell_{max}} R_\ell^m\int_{-1}^{1}\overline{P}_{\ell'}^m(\theta)\overline{P}_\ell^m(\theta)x^4dx.\end{aligned} \tag{7.7}$$

Using the recurrence relation 4.52 to eliminate the two powers of x within their respective integrands, performing the normalization on the right hand side and resetting ℓ' back to ℓ results in

$$\begin{aligned}
\frac{dR_\ell^m}{dt} &= - imAR_\ell^m \\
&- imB\left\{\left[\frac{1}{A_\ell^m A_{\ell-1}^m}\right]R_{\ell-2}^m + \left[\frac{B_{\ell+1}^m}{A_{\ell+1}^m A_\ell^m} + \frac{B_{\ell+2}^m}{A_{\ell+2}^m A_{\ell+1}^m}\right]R_\ell^m + \left[\frac{B_{\ell+3}^m B_{\ell+2}^m}{A_{\ell+3}^m A_{\ell+2}^m}\right]R_{\ell+2}^m\right\} \\
&- imC\left\{\left[\frac{1}{A_\ell^m A_{\ell-1}^m A_{\ell-2}^m A_{\ell-3}^m}\right]R_{\ell-4}^m\right. \\
&+ \frac{1}{A_\ell^m A_{\ell-1}^m}\left[\frac{B_{\ell+2}^m}{A_{\ell+2}^m A_{\ell+1}^m} + \frac{B_{\ell+1}^m}{A_{\ell+1}^m A_\ell^m} + \frac{B_\ell^m}{A_\ell^m A_{\ell-1}^m} + \frac{B_{\ell-1}^m}{A_{\ell-2}^m A_{\ell-2}^m}\right]R_{\ell-2}^m \\
&+ \left[\frac{B_{\ell+3}^m B_{\ell+2}^m}{A_{\ell+3}^m A_{\ell+2}^m A_{\ell+2}^m A_{\ell+1}^m} + \left(\frac{B_{\ell+2}^m}{A_{\ell+2}^m A_{\ell+1}^m}\right)^2\right. \\
&+ \left.\frac{2B_{\ell+2}^m B_{\ell+1}^m}{A_{\ell+2}^m A_{\ell+1}^m A_{\ell+1}^m A_\ell^m} + \left(\frac{B_{\ell+1}^m}{A_{\ell+1}^m A_\ell^m}\right)^2 + \frac{B_{\ell+1}^m B_\ell^m}{A_{\ell+1}^m A_\ell^m A_\ell^m A_{\ell-1}^m}\right]R_\ell^m \\
&+ \frac{B_{\ell+3}^m B_{\ell+2}^m}{A_{\ell+3}^m A_{\ell+2}^m}\left[\frac{B_{\ell+4}^m}{A_{\ell+4}^m A_{\ell+3}^m} + \frac{B_{\ell+3}^m}{A_{\ell+3}^m A_{\ell+2}^m} + \frac{B_{\ell+2}^m}{A_{\ell+2}^m A_{\ell+1}^m} + \frac{B_{\ell+1}^m}{A_{\ell+1}^m A_\ell^m}\right]R_{\ell+2}^m \\
&+ \left.\frac{B_{\ell+5}^m B_{\ell+4}^m B_{\ell+3}^m B_{\ell+2}^m}{A_{\ell+5}^m A_{\ell+4}^m A_{\ell+3}^m A_{\ell+2}^m}R_{\ell+4}^m\right\},
\end{aligned} \tag{7.8}$$

where the A and B coefficients are given in equations 4.53 and 4.54, respectively.

The value of the spectral coefficient can then be determined at any time using

$$R_\ell^{m'}(t+\Delta t) = R_\ell^{m'}(t) + \frac{dR_\ell^m}{dt}\Delta t = R_\ell^{m'}(t) + \Delta R_\ell^{m'}(t), \tag{7.9}$$

and by calculating

$$\Delta R_\ell^{m'}(t) = \frac{dR_\ell^m}{dt}\Delta t, \tag{7.10}$$

all the information is needed to evolve the spectral coefficient at each timestep Δt to produce the effect of differential rotation. It can be shown that the poloidal and toroidal spectral coefficients can be evolved in the same way to progress all three coefficients and thus dynamically progress a given velocity field by means of a given differential rotation profile.

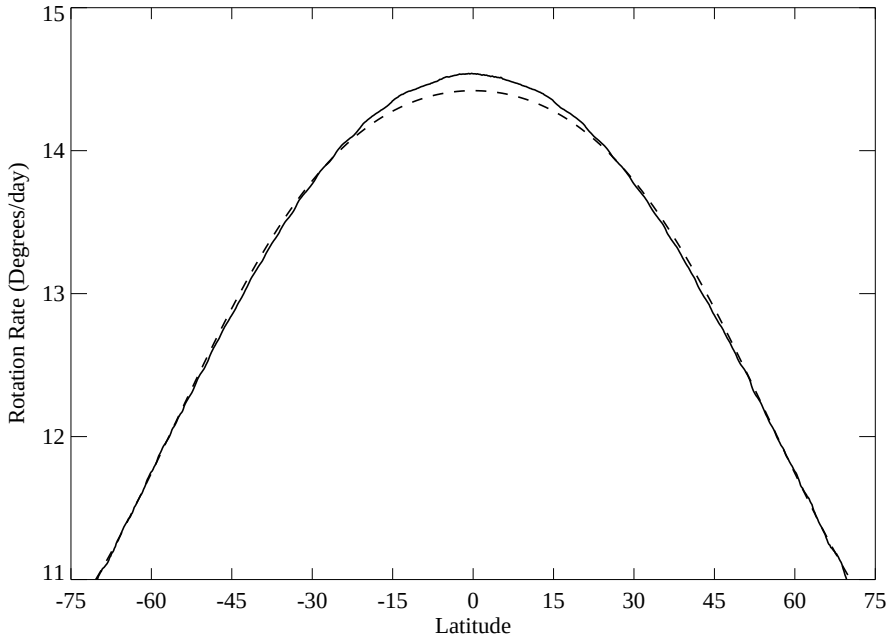

Figure 7.1. Differential rotation profile produced from a numerical evolution of the spectral coefficients. The solid line is the output profile from the updated data simulation and the dashed line shows the profile produced from using the coefficients described in the text in the fourth order colatitude differential rotation profile..

The simulation has been updated to include effect of differential rotation where the profile can be adjusted simply by adjusting the three polynomial coefficients of Eqn. 4.17. Using a given set of coefficients (A=14.42, B=-2.00, C=-2.09 [82], all measured in degrees per day), a set of Doppler maps were produced and correlated to produce a synthetic rotation profile. Comparing this to the input profile (Fig. 7.1), it can be seen that the match between input and output profiles is very good. The discrepancy at the equator is accounted for by the superrotation of the Doppler pattern due to geometric projection effects as described in Chapter 5.

7.1.2 Modeling the Solar Internal Differential Rotation

Helioseismic measurements have shown that the Sun not only rotates differentially in latitude, but also in radius. Using methods such as rotational splitting and inversion

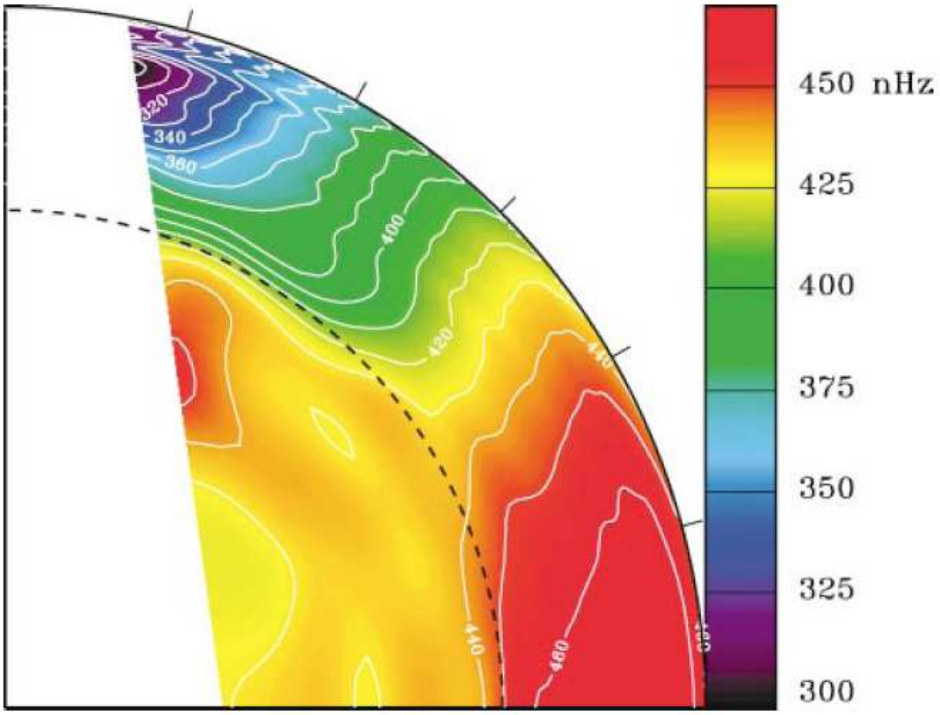

Figure 7.2. Internal rotation profile of the Sun derived from observations by MDI [115]. The horizontal axis defines the equator and the vertical axis defines the pole. Contour labels are in nHz and the dashed line defines the base of the convection zone. The latitudinal tick marks are spaced by 15 degrees.

techniques [114], [14], [115], two dimensional radial and latitudinal differential rotation profiles have been produced 7.2.

The profile clear shows distinct variation in the two directions. Latitudinally, the profile tends to continue the trend of faster rotation at the equator than near the pole with a nearly constant radial profile at mid latitudes, while showing some variance with depth at the near the two latitudinal ends of the domain. Notably, the profile sharply changes near the surface and near the base of the convection zone. At the surface, there exists a shear layer which sharply reduces the rotation with increasing depth, possibly due to the presence of ionization in this region [65]. At the base of the convection zone, there exists an even sharper shear layer which actually defines the boundary between the convection zone and the deeper radiative zone, called the tachocline. Within the radiative zone itself, the rotation is observed to be essentially that of a solid body.

Although unreliable below R=0.8$R_\odot$, at depths above this the latitudinal differential profile of 7.2 is valid [14]. This means that is possible to use the updated simulation described in the previous section to construct a synthetic rotation profile using 7.2 and derived values for the three coefficients. The latter process is done by extracting rotation values at a given depth and latitude from an already existing profile (for example, that shown in Fig. 7.2). To test the integrity of the extracted data (for example, for reasons of sampling resolution) the rotation rates at a given depth and a given latitude were re-plotted, as shown in Fig. 7.3.

Next, each latitudinal profile at each sampled depth was plotted and fitted and using a least squares fit of data using 7.2. From this fit, the three coefficients can be found.

These coefficients were then used in the updated data simulation to provide a series of maps for each sampled depth. Maps within the series were correlated and rotation profiles determined at each depth. A further two dimensional plot of the internal rotation profile is shown in Fig. 7.4, and illustrates that above the valid $R = 0.8R_\odot$ region, the data simulation accurately models the internal rotation of the Sun.

By sampling points throughout the convection zone, an expression can be constructed to describe the radial differential rotation profile. Further, by assuming that the size of a convection cell, described by its wavenumber ℓ, relates directly to the depth at which it is anchored within the convection zone the expression can be used to describe the rotation rate of convection cells as a function of their of size ℓ. Considering the profile at the equator, we get

$$\Omega(\ell) = A - 0.34\sqrt{(\frac{\ell}{1000}}), \tag{7.11}$$

where A is the equatorial rotation rate as applied in Eqn. 4.17 and is measured in degrees per day, as is the coefficient of 0.34.

With each individually sized convection cell now having its own rotation rate as described by Eqn. (7.11), we revisited the work we performed in regard to Fourier analysis

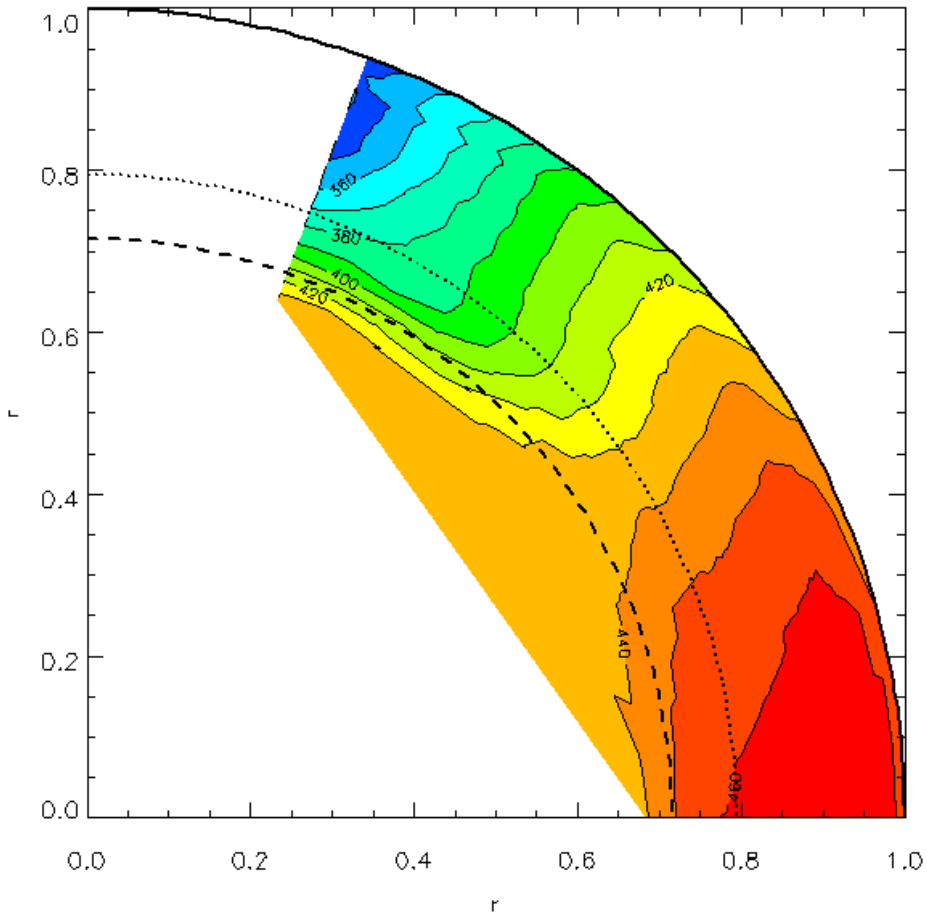

Figure 7.3. Internal rotation profile of the Sun using extracted values from the previous figure. Despite the course sampling grid, the figure reproduces the profile well including the shear at the tachocline. However, because of the sharp shear at the surface, the sampling does not exactly represent this shearing. The dashed line again shows the tachocline while the dotted line shows the depth above which the rotation profile of 7.2 is applicable.

of the superrotation phenomenon as described in Chapter 5. Previously, the result shown in Fig. 5.3 produced a profile similar to that obtained from observational data [94] for wavenumbers below $m \sim 100$ and with asymptotic behavior beyond $m \sim 200$. In the context of the internal rotation profile, this was due to a lack of resolution in the profile near the surface (i.e. at large wavenumbers). After applying the internal profile of Eqn. (7.11) to the simulation that will now produce not only latitudinal differential rotation, but also differential rotation over the range of convection cell sizes, and following

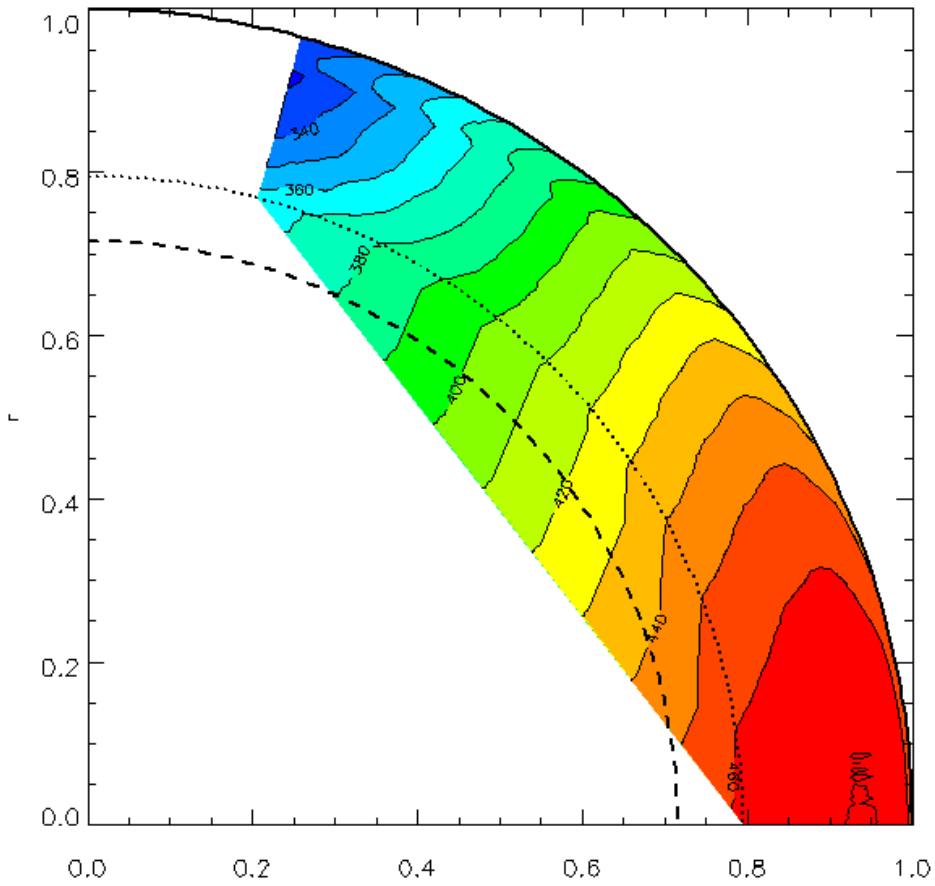

Figure 7.4. Internal rotation profile of the Sun derived from correlating Doppler maps from the updated data simulation.

the same Fourier analysis procedure as described Section 5.2.3, we produce the plot shown in Fig. 7.5.

These results further confirm our theory that superrotation is indeed a projection effect and not due to any wavelike properties.

7.1.3 Future Work

The first stage of updating the data simulation to include large scale flow field dynamics to advect the convection velocity field has been made by including an algorithm to evolve the spectral coefficients to model differential rotation. The model was successfully tested against an existing profile extracted from real data and extended to produce a realistic profile if the internal differential rotation.

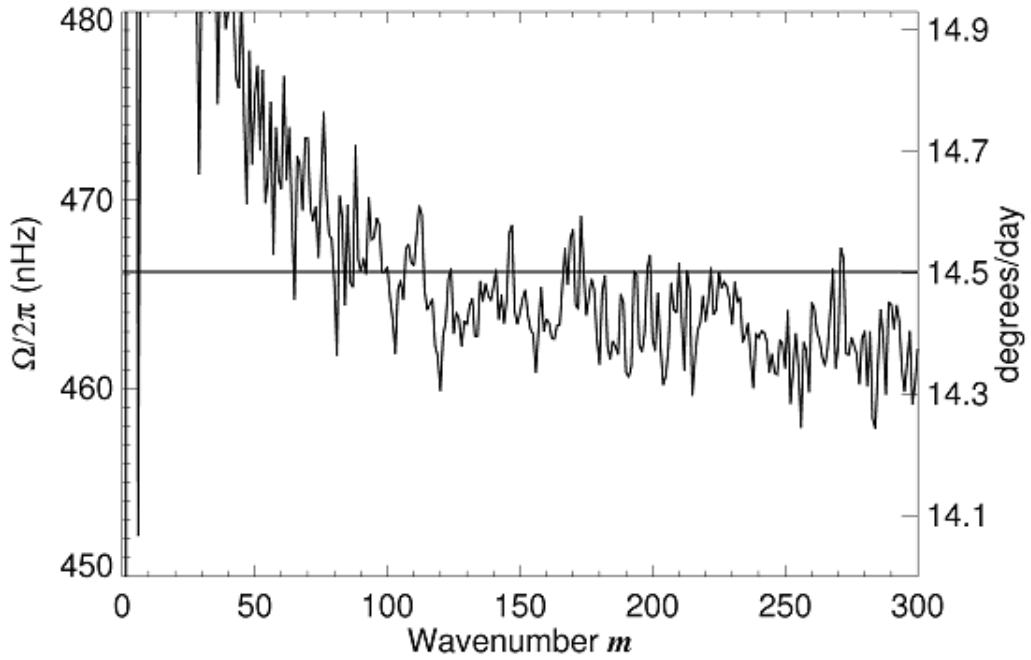

Figure 7.5. The equatorial rotation rate from the 2D Fourier analysis study using the updated simulation to include internal differential rotation. The behavior below wavenumbers of $m \sim 100$ is the same as before (Fig. 5.3), but the rate continues to drop off at higher wavenumbers in line with observational results [94].

A further extension to the model is to include the flow field due to meridional circulation. The algorithms to evolve the spectral coefficients have been derived but a discrepancy between the radial and the solenoidal expressions still has to be solved.

7.2 Modeling Convection Cell Evolution

A further extension to the simulation was to attempt to accurately evolve the convection cells over time. This has adequately been performed thus far by means of a simple evolution of phases, but a more accurate evolution, i.e. one that gives similar results to those seen observationally, is required.

Within the process of determining the rotation rates over the range of solar latitudes as used in Section 5.2.2, cross-correlation peaks are used to determine the rotation rate at a given latitude from correlating latitudinal strips of data of two images separated by a specified time difference. These correlation coefficients can be collected over a range of

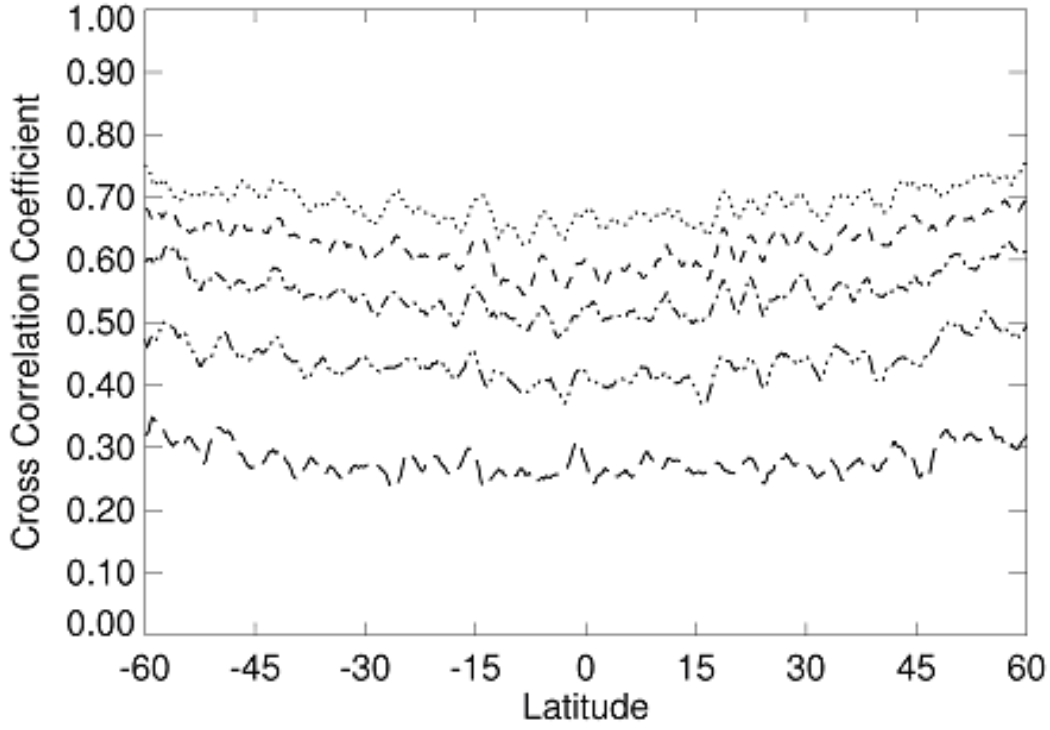

Figure 7.6. Cross-correlation coefficient profiles derived from MDI Doppler images for time differences of (top-to-bottom) 1-hour, 2-hour, 4-hour, 8-hour, and 16-hour between maps.

time differences and over the latitudinal domain of the Sun. It is found that for increased time differences, i.e. as time progresses, the correlation coefficients decrease (Fig. 7.6). This is expected due to the observed decay of convection cells over time.

7.2.1 Phase Evolution

To perform convection cell evolution within the simulation requires an evolution of the phases that produce the convection pattern. Assuming an initial phase of zero, then the pattern would look completely different at a phase of π, i.e. the final pattern is totally out of phases with the original. As it is only required that the final phase of the pattern be reduced by a factor of e to produce a significant change compared to the original pattern, then it is only required that the phase be evolved from zero to π/e. This value can be estimated to be around unity, so that we need only evolve the phases from zero to one.

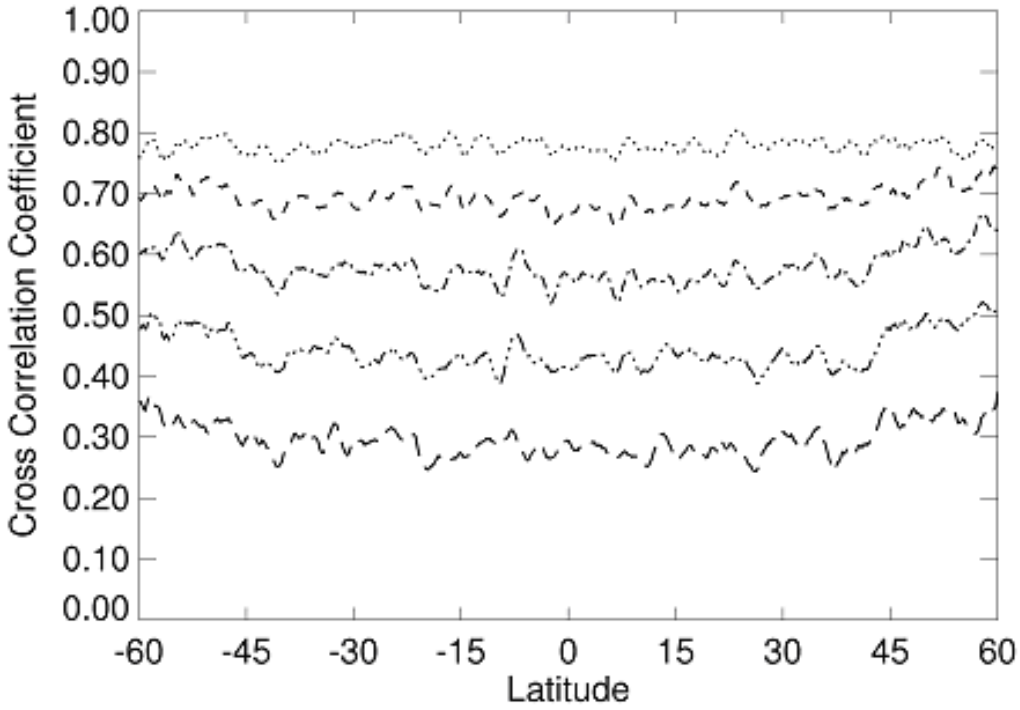

Figure 7.7. Cross-correlation coefficient profiles derived from synthetic data produced from a version of the simulation extended to include accurate evolution of convection cells dependent on their size and noise factors modeling the non-perfect temporal filtering. Similar to Fig. 7.6, the coefficient are plotted over latitude for time differences of (top-to-bottom) 1-hour, 2-hour, 4-hour, 8-hour, and 16-hour between maps.

A further consideration is that the convection cell lifetime differs dependent on the cell size. Larger cells live longer than smaller cells. Therefore, the phase evolution must also be size dependent, i.e. a function of the wavenumber ℓ. Setting a value of a lifetime of 48 hours for a cell of size $\ell \sim 100$, we produced an expression to determine the change in phase at each simulation timestep dependent on the cell size, derived from trial and error methods, using observational data as the benchmark

$$\Delta\phi = C\ \Delta t \ell^{5/6}. \tag{7.12}$$

$\Delta\phi$ is the change in phase for each timestep Δt, $\ell^{5/6}$ provides the size dependence of the rate of evolution and C progresses the phases to a value of π/e in the form of a random walk.

7.2.2 Adding Another Noise Component

A further addition to the simulation which has a bearing on the present subject was the inclusion of a noise term. Thus far, noise has been included to account for that produced within the instrument as mentioned in Section 4.4.2. However, it is found that an extra element of noise exists due to the less than perfect 31 minute temporal filtering as described in Section 4.2.2. Larger, longer lived oscillation elements are able to leak through the filtering produce resulting in a speckled noise component in the Doppler image that exhibits a strength variation across the disk dependent on the square root of the distance to disk center. Trial and error methods were used to adequately produce this noise, modeled using random sampling Gaussian distribution, by comparing real and synthetic Doppler images.

7.2.3 Results

Incorporating the phases evolution process and the additional noise considerations, we performed a cross-correlation analysis over a range of time differences to extract the correlation coefficients over the latitudinal domain using synthetic data produced by the updated simulation in a similar manner to that described earlier for the MDI data. Fig. 7.7 shows the results of the analysis of this synthetic data.

7.2.4 Conclusions

Comparing Fig. 7.7 to Fig. 7.6, there is an excellent similarity between the plots over all time differences. The similarity is also consistent over all latitudes. Improved versions of this evolution may be performed by more accurately analyzing the noise produced by the temporal filtering and by more accurate modeling of the evolution for smaller, shorter lived convection cells that is highlighted by comparing the plots for 1-hour and 2-hour time differences between the two figures.

CHAPTER 8

THE SEARCH FOR GIANT CELLS

8.1 Introduction

The focus of the research discussed thus far have been supergranules, with a typical size of around 30 Mm that is characterized in the photospheric convection spectrum as a peak at around $l \sim 110$ wavenumbers. However, it can be seen that the this peak covers a range of wavenumbers, so it expected that supergranules themselves come in a variety of sizes. At the high wavenumber end, supergranules become smaller and their size range tends to coincide with the larger end of granules, whose peak is seen in the high resolution convection spectrum (Fig. 4.8). At low wavenumbers, supergranule sizes increase although they are less common, as reflected in the lower power in the convection spectrum. However, at the lowest wavenumbers, a separate component of convection, namely giant cells, has been proposed to exist.

The earliest prediction of giant cells was made from a model produced by Simon and Weiss [39] that signified typical cell sizes of 300,000 km ($\sim 0.06\ R_\odot$ or $l \sim 15$) and lifetimes of 34 days (~ 1.25 solar rotations). Subsequent observational techniques have been proposed and carried out, but with no definitive results [116], [117], although methods of correlating strips of Doppler data [93] and tracking the motions of supergranules in Dopplergram images [118], [119] may still hold potential. A claim had been made [40] that by correlating Dopplergrams over many rotations giant cells had indeed been detected. Despite a long-lived, recurring signal being seen, there is still no real evidence that these are due to convecting giant cells and may be a form of inertial oscillation [120].

In what follows, I describe a numerical analysis that I performed to study the influence of a single giant cell component on a single component of supergranulation [121].

8.2 Numerical Experiment into Giant Cell Advection of Supergranules

It has been observed that not only does the supergranule signal seem to exhibit prograde superrotation, but also shows a retrograde rotation signal [55]. As well as these extra longitudinal velocity signals, both poleward and equatorward flow signals have been detected [59]. These investigations both suggest that wavelike phenomena carry the supergranule cells across the solar surface. Our work described in chapter 5 has shown that the majority of the prograde superrotation signal is due to a projection effect of modulating the supergranule signal by the sine of the longitude. The remaining excess signals, however, are yet to be explained.

Our hypothesis is that underlying divergent giant cell flows advect the supergranule cells across the solar surface producing the observed latitudinal and longitudinal signals. To study how giant cell flows may interact with supergranule cells contained within, we formulated a simple time-dependent numerical experiment.

A simplified supergranule pattern comprising of a single sinusoidal component at a wavenumber $m = 100$ was constructed in a one-dimensional domain defining the equator of the Sun. Our goal was to advect this supergranule signal with an underlying giant cell component constructed at a wavenumber $m = 20$.

The advection would be carried out by evolving the amplitude and phase information of the supergranule pattern, in a similar manner to how the differential rotation advected the convective Doppler patterns as described in Section 7.1. Using the one-dimensional version of the momentum equation

$$\frac{\partial u_\phi}{\partial t} = -v_\phi \frac{\partial u_\phi}{\partial \phi}, \tag{8.1}$$

where u_ϕ defines the supergranule signal and v_ϕ defines the giant cell signal and the derivatives are taken in time, t, and longitude, ϕ, respectively.

Using a sinusoidal distribution for the one-dimensional poloidal flows along the equator only, we get for u_ϕ

$$u_\phi = \sum_m S_m \; e^{im\phi}. \tag{8.2}$$

The complex spectral amplitudes, S_m, were initially set to 1.0 at m=100, while for all other wavenumbers (within the range m=0 to m=1024), the amplitude is zero. At this wavenumber, accompanying the non-zero spectral amplitudes are random phases to make the supergranular spectral distribution more realistic. These are applied using the exponential term.

The giant cell pattern is constructed using

$$v_\phi = A\cos(\bar{m}\phi) = \frac{e^{i\bar{m}\phi} + e^{-i\bar{m}\phi}}{2}, \tag{8.3}$$

where $\bar{m}$=20, defining the wavenumber of the giant cell component. The amplitude, A, can be varied to provide the velocity amplitude at which the supergranule signal is advected.

Substituting 8.2 and 8.3 into 8.1, normalizing and writing the changes in S_m and t as discrete quantities results in the change in amplitude ΔS_m at a given wavenumber, m, over a given timestep, Δt,as

$$\Delta S_m = -\frac{iA}{2}((m-\bar{m})S_{m-\bar{m}} + (m+\bar{m})S_{m+\bar{m}})\Delta t. \tag{8.4}$$

By progressing the amplitudes from $S_m^{(t)}$ to $S_m^{(t+1)}$ (i.e., by ΔS_m) over a timestep Δt, the supergranule signal at time t is given by

$$u_\phi^{(t)} = \sum_m S_m^{(t)} \; e^{im\phi}. \tag{8.5}$$

The timestep and the giant cell advection velocity were chosen such that the supergranule pattern changes slowly to give a smooth and steady progression of the pattern evolution at a reasonable temporal resolution and the number of timesteps chosen so that the supergranule pattern would be evolved long enough to observe stretching in some regions and bunching up in others. The longitudinal domain from ϕ = -π/2 to ϕ =

$\pi/2$ was divided into 2048 discrete points to provide the required spatial resolution for the experiment to progress. Rotation was neglected for this study.

Fig. 8.1 shows a series of images sampled at regular time-steps displaying the distribution of the supergranule pattern across the domain. It can be seen that as time progresses the pattern evolves are expected. In some regions the pattern is compressed corresponding to the convergent velocities at the boundaries of adjacent giant cells, while in other regions the pattern is stretched out, corresponding to divergent velocities at the center of the giant cells.

8.3 Future Work

The data created in the numerical experiment can be reformatted and processed using Fourier analysis to produce power spectra that can be compared with that produced from observational studies as shown in Fig. 8.2 [59]. The convergent and divergent flows that are observed in our experiment become a series of prograde and retrograde flows in a rotation frame and should produce similar signals as to those seen by Schou [59].

In a similar manner to the implementation of the differential rotation surface flows into the data simulation (Section 6.1) and using the results of the numerical experiment, a two-dimensional giant cell surface flow profile may be constructed and, via the momentum equation, the expressions to evolve the spectral coefficients derived. Synthetic Doppler images produced can be Fourier transformed in latitude, longitude and time and the resulting power spectra compared to those produced from the MDI data [59]. Such MDI data can be further scrutinized for any explicit signals of giant cells via spatial and temporal filtering while accounting for the continued presence of any instrumental artifacts.

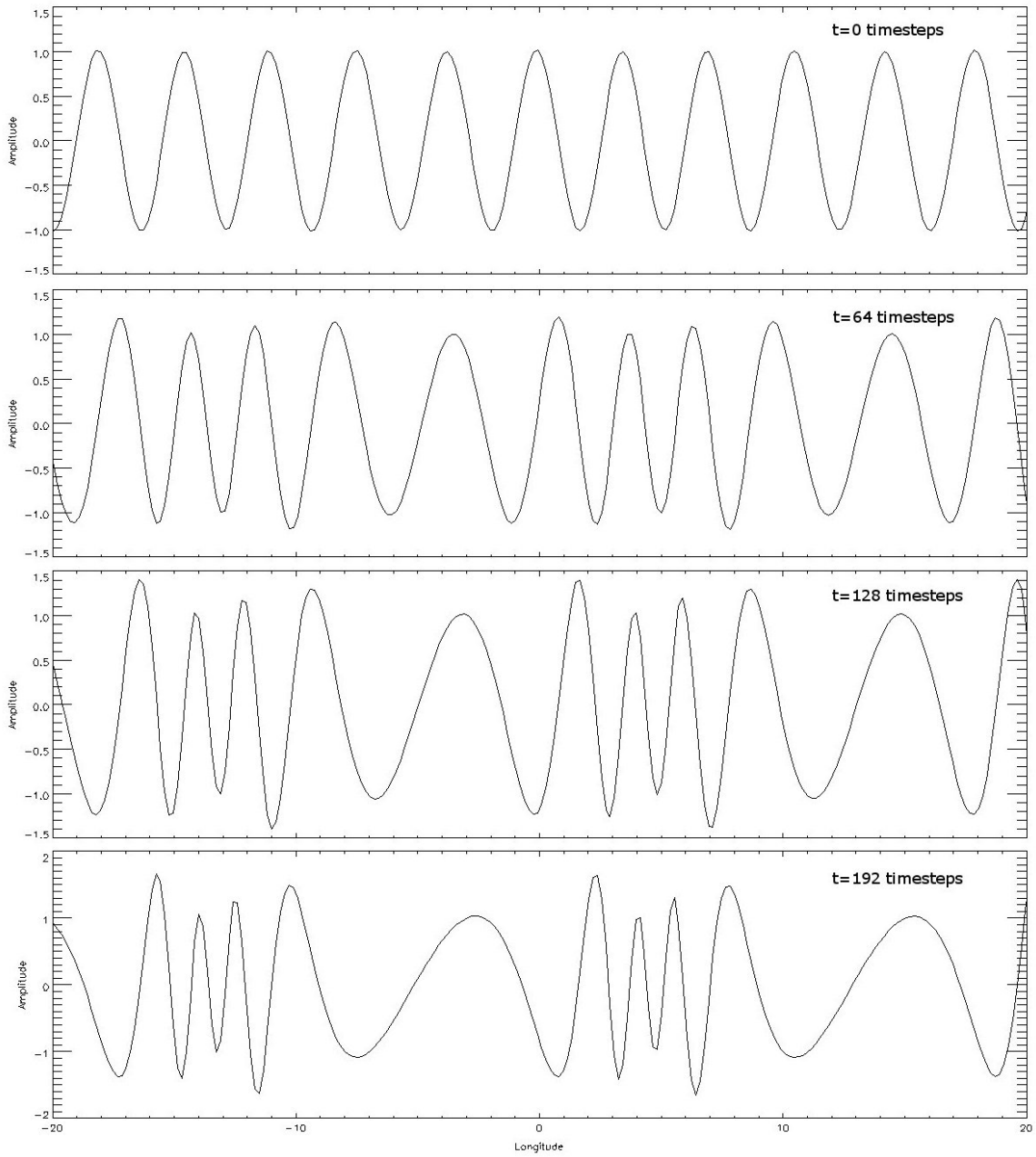

Figure 8.1. Series of timeplots illustrating the advection of a supergranule pattern by a giant cell component performed from a numerical simulation. The plots show a domain 20 degrees in longitude either side of the central meridian. Adjacent giant cells exhibit converge flows which bunches up the supergranule pattern, while the centers of the giant cells spread the pattern out. These convergent and divergent flows are prograde and retrograde to any underlying rotational flow, which is left out of this simulation for simplicity.

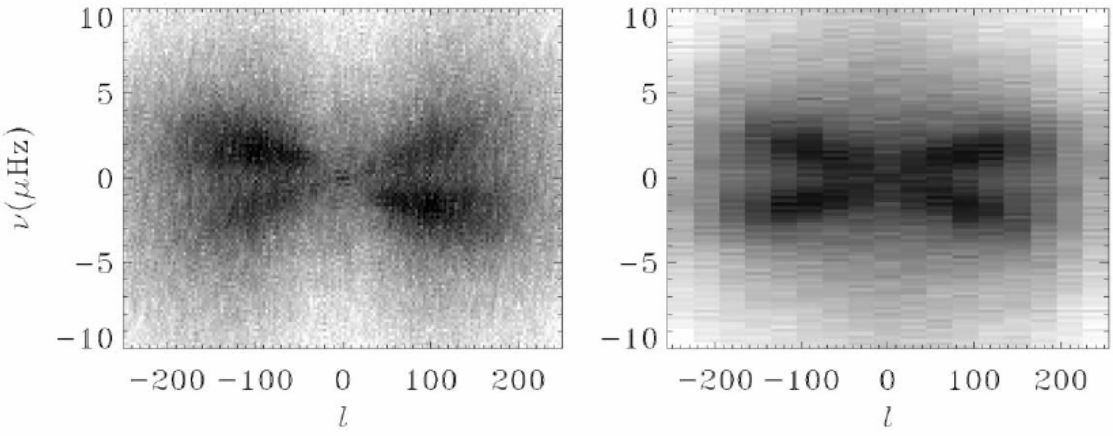

Figure 8.2. Power spectra derived from Doppler maps illustrating the advection of supergranule cells [59]. The gray scale is logarithmic with black pixels representing 300 times more power than white pixels. The signal is de-rotated so that any inherent solar rotation is not included. (Left) Spectrum taken longitudinally at the equator showing power excess due to prograde (diagonally top left to bottom right) and retrograde advection (diagonally top right to bottom left) of the supergranule signal. Excess seen in the prograde signal we can attribute to the projection effect phenomenon. The steep negative gradient slope near $\ell = 0$ is due to stationary artifacts in the MDI Doppler signal that become visible due to the derotation process. (Right) Spectrum taken latitudinally at 40 degrees latitude. The excess power shows poleward flow (diagonally top left to bottom right) and equatorward flow (diagonally top right to bottom left). Whereas such signals have previously been attributed to wavelike phenomena carrying the supergranule signal, we hypothesize that the advection is carried out by underlying giant cell flows.

CHAPTER 9

CONCLUSIONS AND FUTURE WORK

9.1 Conclusions

The work I have performed and described in this dissertation has assisted in constraining solar properties, providing new characteristics of supergranules, extending Doppler map analysis by ways of enhancing the data simulations and furthered the discussion of the existence of giant cells and their influence on smaller convection components.

9.1.1 Supergranule Superrotation

By means of analyzing synthetic Doppler images produced by data simulations, we have accounted for the observational characteristics of the rotation of convection cells around the Sun as described in the literature [53], [93], [94], [55], [59]. In contrast to earlier conclusions that the cause of superrotation derives from underlying wavelike phenomena [94], [55], we find that the superrotation can easily be explained by considering the influence of geometric projection effects due the Doppler signal being modulated across the solar disk image.

9.1.2 Supergranule Manifestations as Hills at the Solar Limb

The production observed corrugation of the solar surface [57] had hitherto been attributed to the existence of Rossby waves in the Sun [58]. Using our data simualtion, we produced a timeseries of heights around the solar limb which were analyzed using the same process as that performed on MDI data [58]. We found signals identical to those derived from MDI data, although our data simulation contains no wavelike characteristics whatsoever. We conclude that Rossby waves are not the cause. By analyzing the resultant

signals from input convection spectra with only granule and supergranule components respectively, we find that supergranulation is the behind the signal. We therefore conclude that the hills observed around the limb are caused by the overshooting of the upflows of supergranules, a phenomenon that opens up potential research in itself.

9.1.3 Extending the Data Simulations

Although the data simulation has provided Doppler images that are identical to those produced from MDI observations, subsequent improvements can still be made. The modeling of large scale flows to advect the convection pattern were considered and a method to implement the observed latitudinal dependent differential rotation, by means of evolving the spectral coefficients that make up the synthetic Doppler pattern, derived. The result of this implementation produced rotation rates exactly like those observed as well as pronounced superrotation near the equator.

Internal rotation rates were sampled from profiles derived from helioseismic data and used to produce similar profiles constructed from synthetic data. Assuming that convection cells stretch deep within the solar interior to a depth equal to their surface size, we produced an expression to determine a size dependent rotation rate of convection cells. Along with additional noise factors to account for the non-perfect temporal filtering of short-lived Doppler features, the rotation data was used to revisit the superrotation phenomenon and produce an even better fit than before to signals derived from observational data. This further entrenches our idea that supergranules are not a consequence of solar wavelike properties.

With differential rotation successfully modeled the simulation may be used to revisit questions, such as the supergranule explanation for solar corrugation, with an increased accuracy which are expected to further entrench our prior conclusions. The implementation of large scale flow dynamics into the simulation can be continued by modeling surface flow profiles due to meridional circulation and giant cells.

9.1.4 Giant Cells

Giant cells have so far not been observed and any evidence of their existence remains circumstantial. To understand what the influence of such structures would have on convection cells such as supergranules, we performed a numerical experiment to simulate the advection of supergranules by an underlying giant cell component. It was found that over time the supergranules became bunched at the boundaries of two adjacent giant cells while dispersed at their centers. Within the context of a rotating frame, constituted by the solar rotation itself, these flows characterize prograde and retrograde flows with respect to rotation. Such flows, both in latitude and longitude, are seen in observational data [59] and our experiment may provide evidence that they produce not by wave phenomena, as previously thought [59], but by these elusive giant cell flows.

Further analysis may be performed not only on the results of our numerical experiment, but on results from a further extension of the data simulation to include a surface wide giant cell flow pattern.

9.2 Future Work

As well as the future research potential as mentioned in the previous section, there are a number of outstanding issues that require investigation. Some of these are outlined in the following.

9.2.1 MDI Instrumental Artifacts

By time-averaging the MDI Doppler data, there results evidence of artifacts within the image that are certainly instrumental in nature. Such artifacts can be analyzed and removed from the data to not only clear the Doppler signal but also characterize some of the outstanding optical issues of MDI. A comparison between MDI and GONG data may be helpful where the data from the Sun is exactly the same, but any instrumental components can be isolated.

9.2.2 Rotation of Supergranules

Upflows of material within the solar interior are expected to be influence by the Coriolis force resulting from the rotating frame within which these upflows reside. Within the specific context of supergranule convection cells, the strength of the Coriolis force is, however, size dependent (Eqn. 2.1) so that whereas smaller cells are less influenced, the larger cells should exhibit a rotation component due to Coriolis factors. It would be worthwhile to derive an expression for the influence of the Coriolis force over the range of convection cell sizes and attempt to model this within the data simulation.

9.2.3 Magnetic Flux Transport Models

With a future working models for the large-scale flows as well as those existent for non-axisymmetric convective flows within the data simulations, the interdependence of material flows and the entrenched magnetic fields can be analyzed. Such analysis would concentrate on localized fields, as those linked to active regions are generally so strong as to inhibit some material flows. The latter, however, offers research possibilities in itself. Local fields can be situated on the solar disk and be advected by the existent flows to produce field patterns and motions that can be compared to observational data. One example is the divergence of flux towards the boundaries of supergranules that is responsible for the observed chromospheric network, while another is the flow of local field lines toward the pole due to the poleward sense of the meridional circulation at the solar surface. The equatorward flow, thought to occur near the tachocline, could well be responsible for carrying active regions equatorward, a characteristic well seen during any particular solar cycle.

APPENDIX A

COMPUTER CODE - FLOWCHARTS

MDI_fake.for

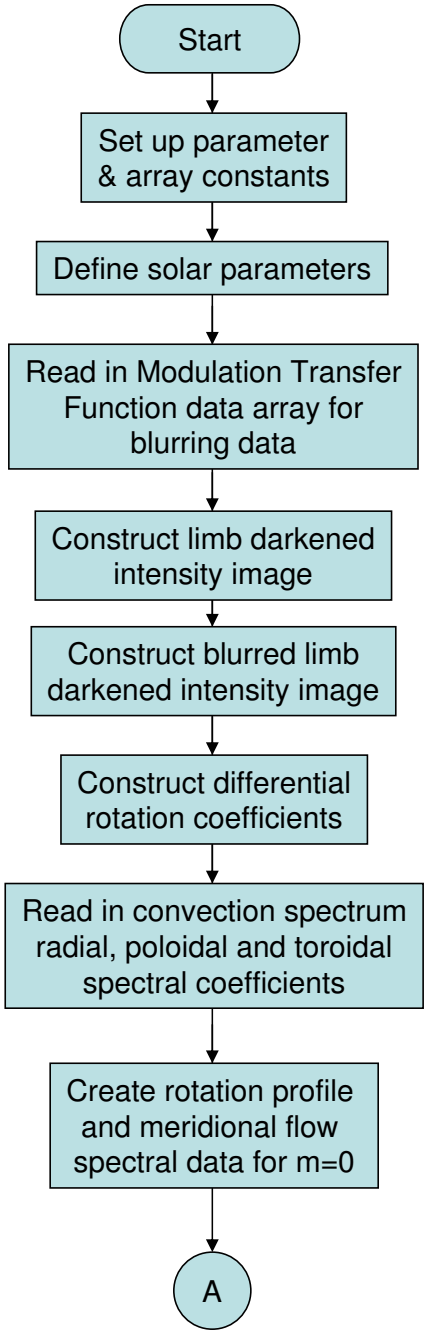
Start
Set up parameter & array constants
Define solar parameters
Read in Modulation Transfer Function data array for blurring data
Construct limb darkened intensity image
Construct blurred limb darkened intensity image
Construct differential rotation coefficients
Read in convection spectrum radial, poloidal and toroidal spectral coefficients
Create rotation profile and meridional flow spectral data for m=0
A

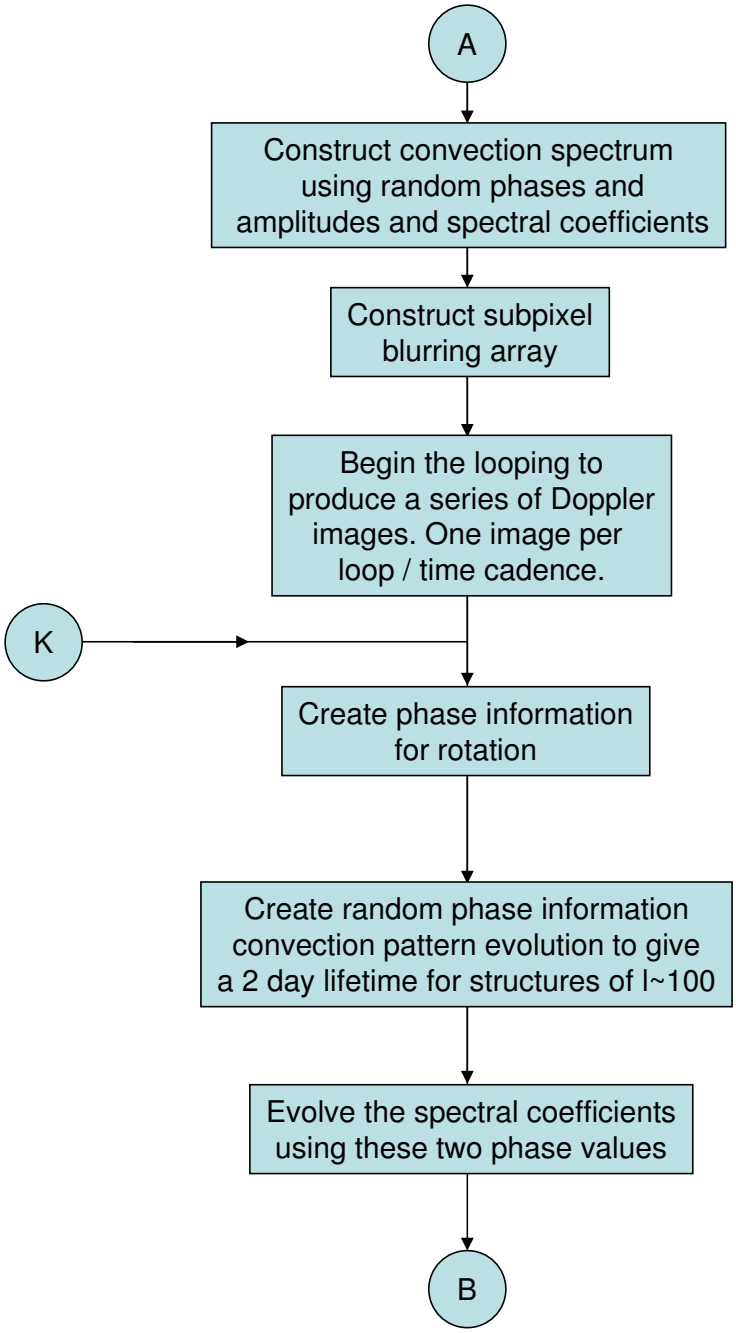
A
Construct convection spectrum using random phases and amplitudes and spectral coefficients
Construct subpixel blurring array
Begin the looping to produce a series of Doppler images. One image per loop / time cadence.
K
Create phase information for rotation
Create random phase information convection pattern evolution to give a 2 day lifetime for structures of l~100
Evolve the spectral coefficients using these two phase values
B

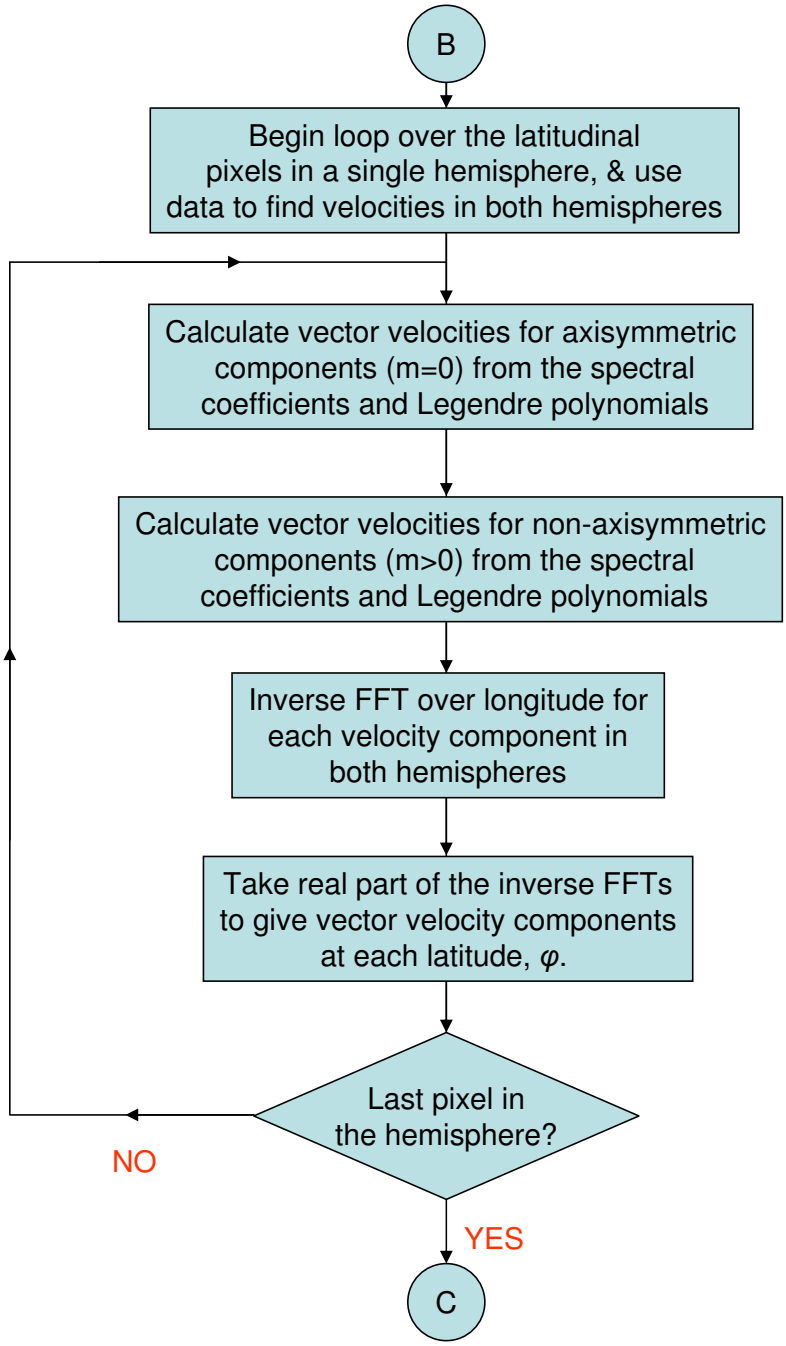
B
Begin loop over the latitudinal pixels in a single hemisphere, & use data to find velocities in both hemispheres
Calculate vector velocities for axisymmetric components (m=0) from the spectral coefficients and Legendre polynomials
Calculate vector velocities for non-axisymmetric components (m>0) from the spectral coefficients and Legendre polynomials
Inverse FFT over longitude for each velocity component in both hemispheres
Take real part of the inverse FFTs to give vector velocity components at each latitude, φ.
Last pixel in the hemisphere?
NO
YES
C

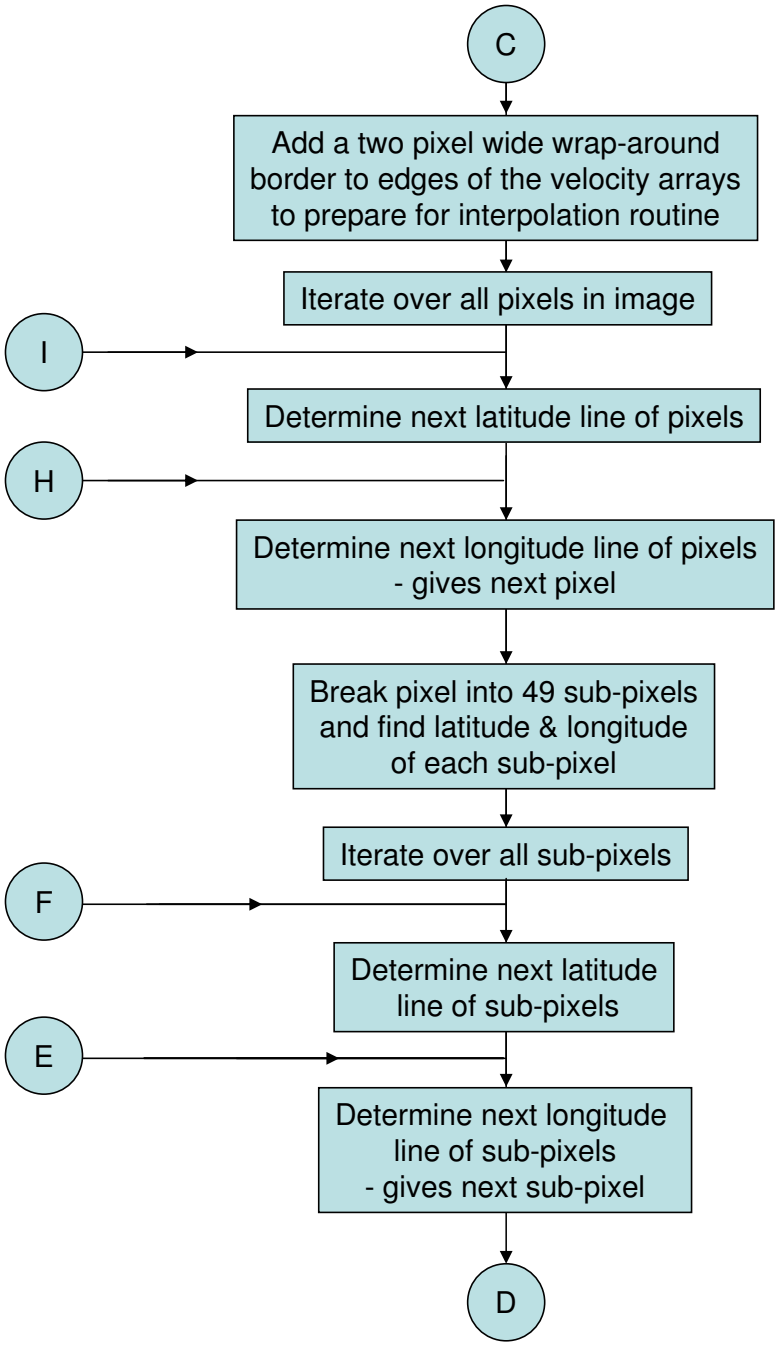
C
Add a two pixel wide wrap-around border to edges of the velocity arrays to prepare for interpolation routine
Iterate over all pixels in image
I
Determine next latitude line of pixels
H
Determine next longitude line of pixels - gives next pixel
Break pixel into 49 sub-pixels and find latitude & longitude of each sub-pixel
Iterate over all sub-pixels
F
Determine next latitude line of sub-pixels
E
Determine next longitude line of sub-pixels - gives next sub-pixel
D

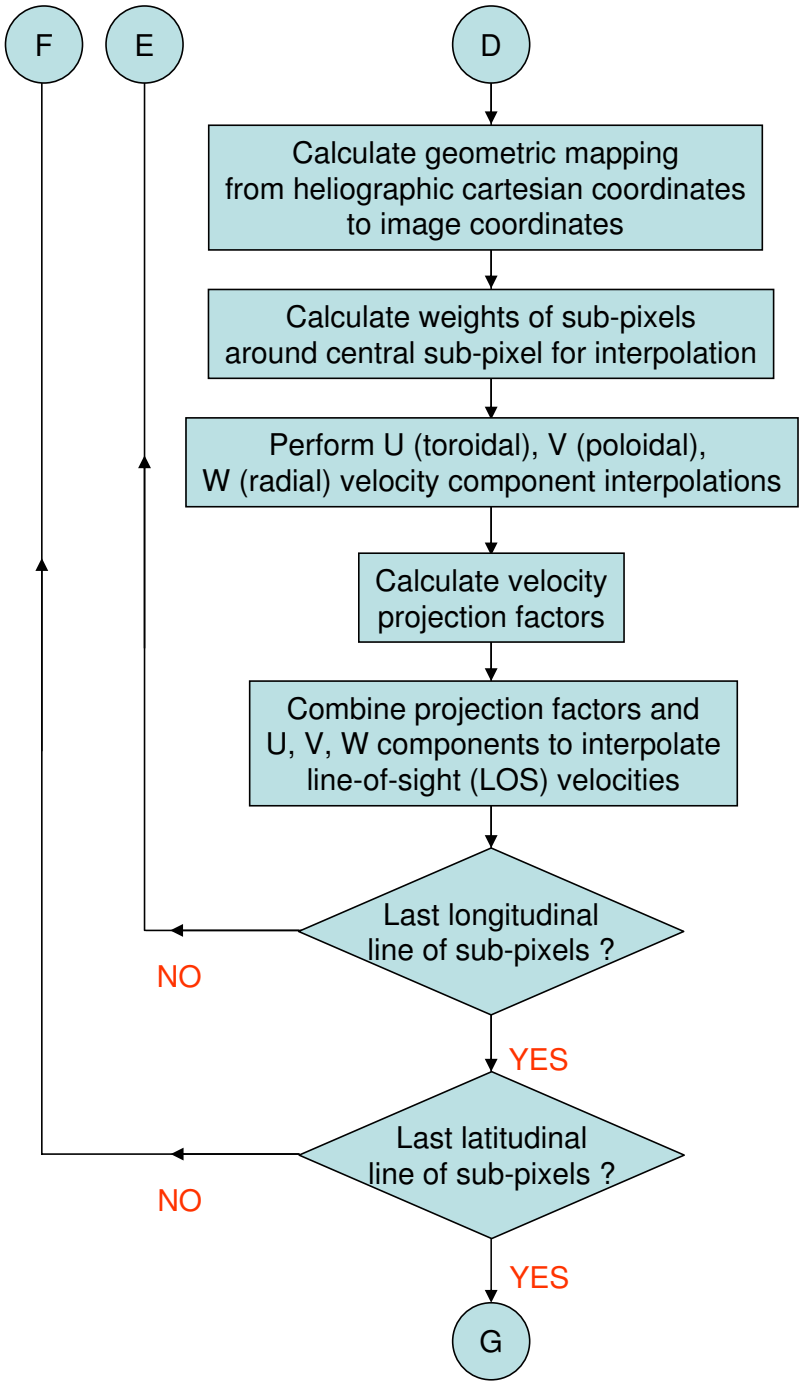
F
E
D
Calculate geometric mapping from heliographic cartesian coordinates to image coordinates
Calculate weights of sub-pixels around central sub-pixel for interpolation
Perform U (toroidal), V (poloidal), W (radial) velocity component interpolations
Calculate velocity projection factors
Combine projection factors and U, V, W components to interpolate line-of-sight (LOS) velocities
Last longitudinal line of sub-pixels ?
NO
YES
Last latitudinal line of sub-pixels ?
NO
YES
G

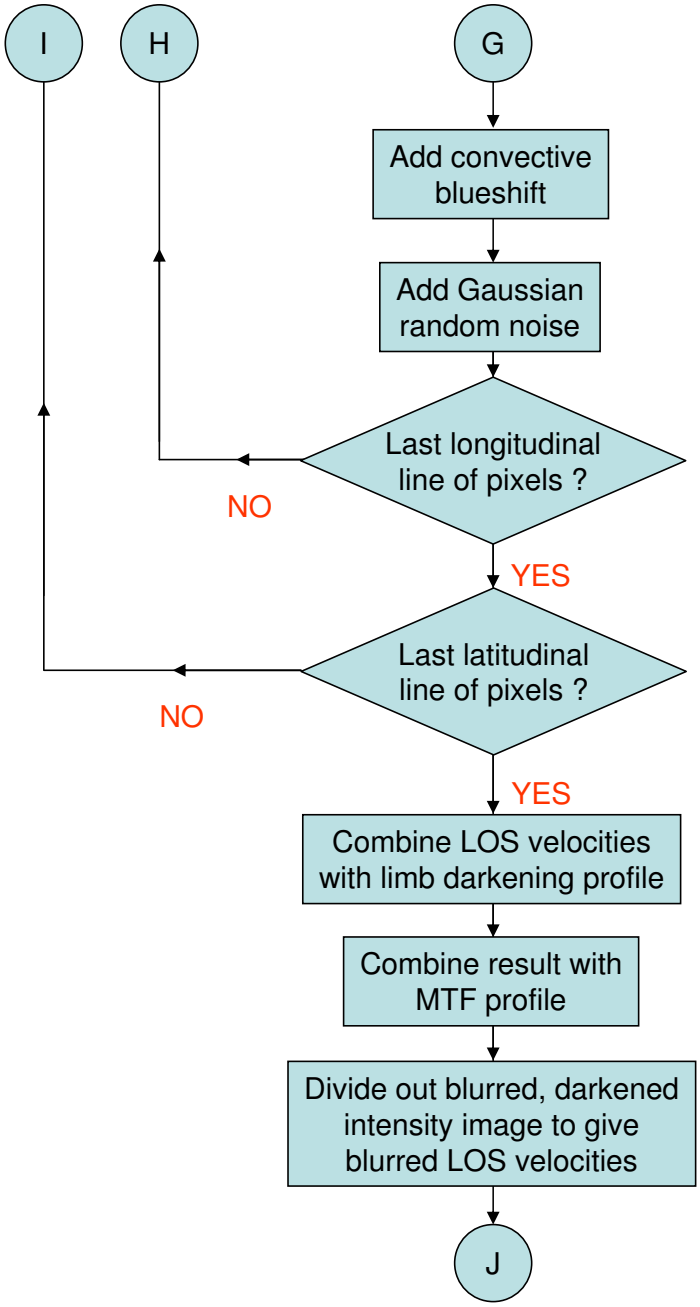
I
H
G
Add convective blueshift
Add Gaussian random noise
Last longitudinal line of pixels ?
NO
YES
Last latitudinal line of pixels ?
NO
YES
Combine LOS velocities with limb darkening profile
Combine result with MTF profile
Divide out blurred, darkened intensity image to give blurred LOS velocities
J

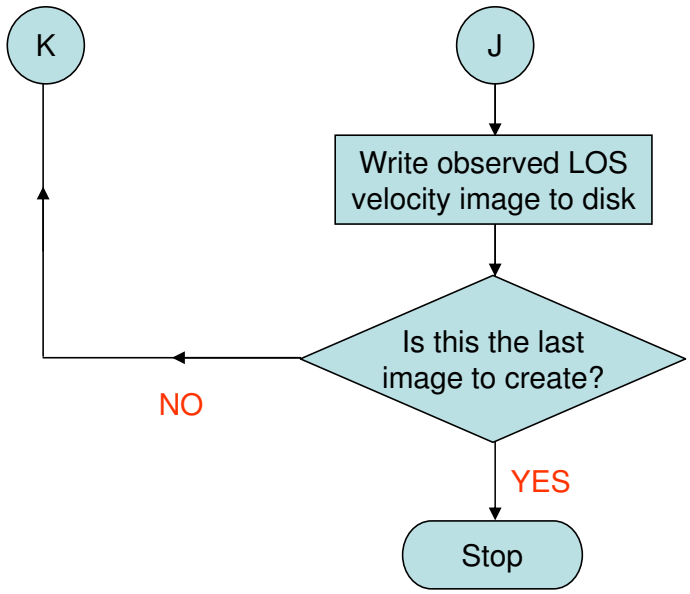
K
J
Write observed LOS velocity image to disk
Is this the last image to create?
NO
YES
Stop

MDI_analysis1.for

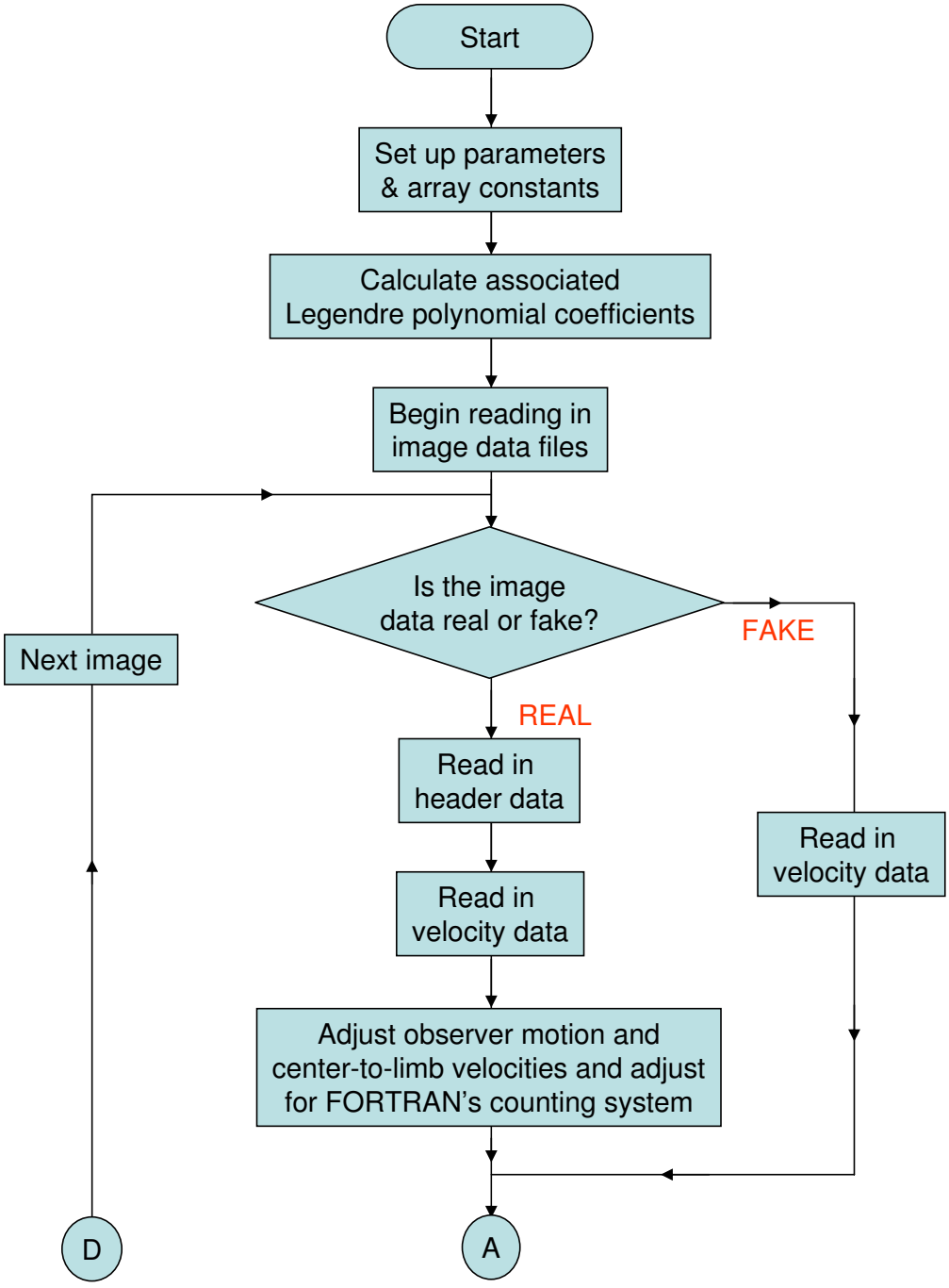

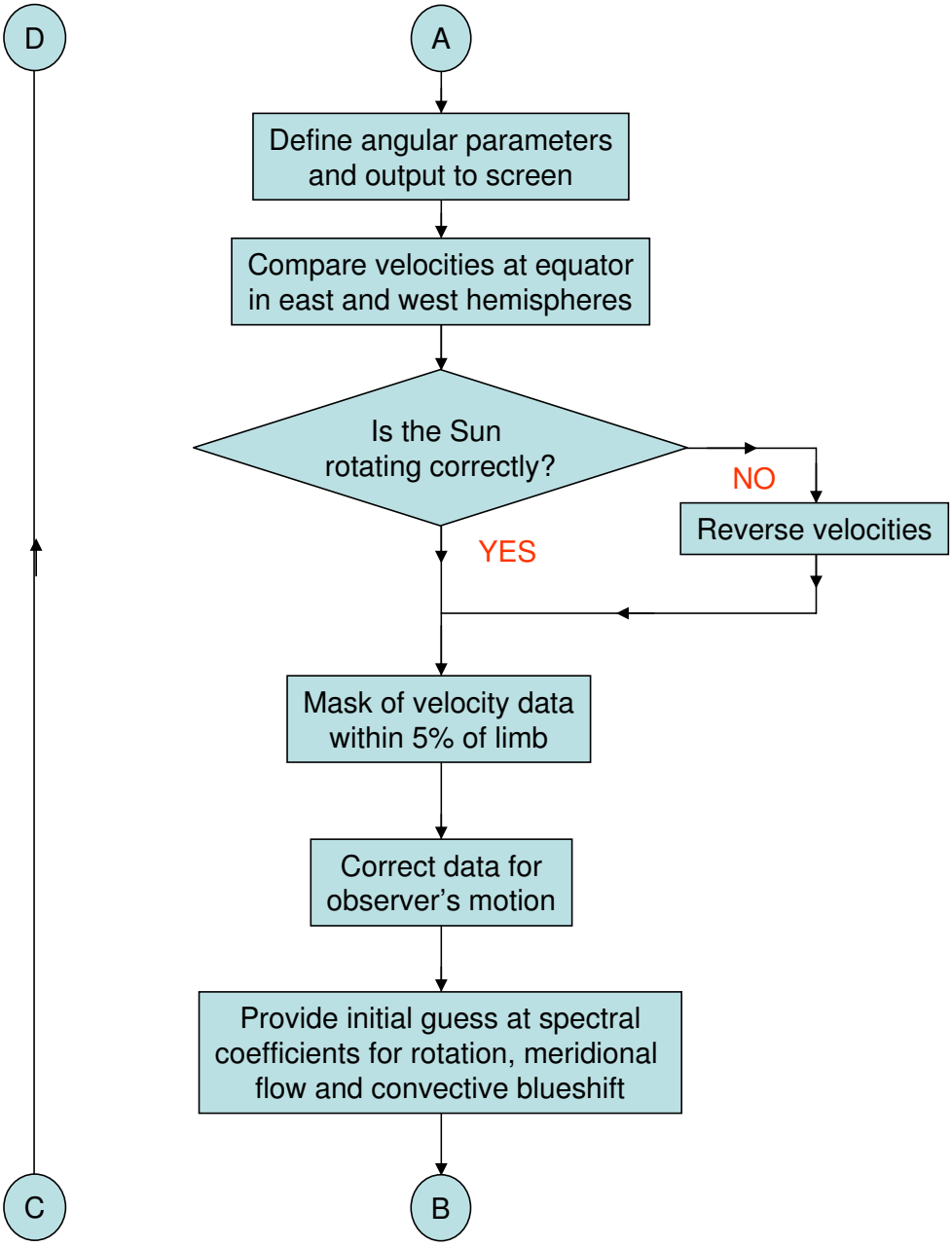
D
A
Define angular parameters and output to screen
Compare velocities at equator in east and west hemispheres
Is the Sun rotating correctly?
NO
Reverse velocities
YES
Mask of velocity data within 5% of limb
Correct data for observer's motion
Provide initial guess at spectral coefficients for rotation, meridional flow and convective blueshift
C
B

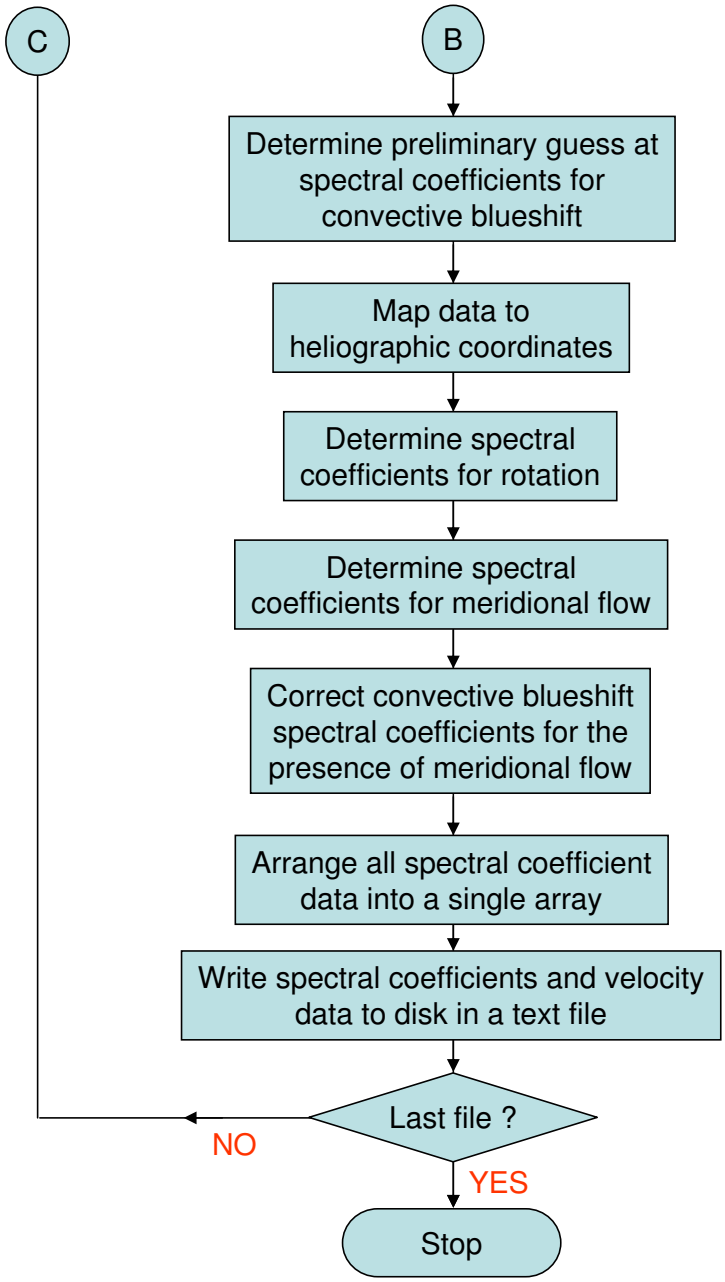
C
B
Determine preliminary guess at spectral coefficients for convective blueshift
Map data to heliographic coordinates
Determine spectral coefficients for rotation
Determine spectral coefficients for meridional flow
Correct convective blueshift spectral coefficients for the presence of meridional flow
Arrange all spectral coefficient data into a single array
Write spectral coefficients and velocity data to disk in a text file
Last file ?
NO
YES
Stop

MDI_analysis2.for

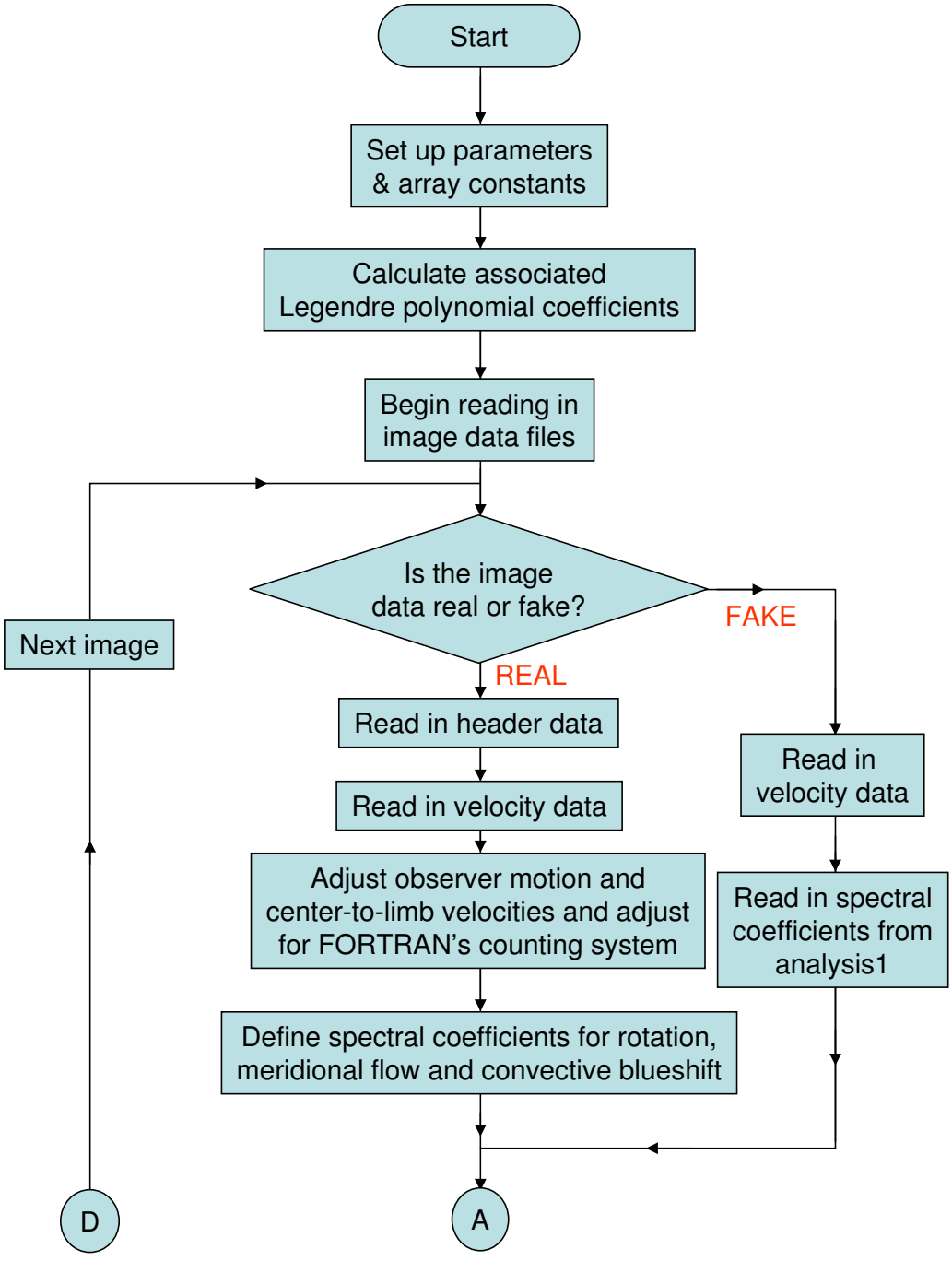

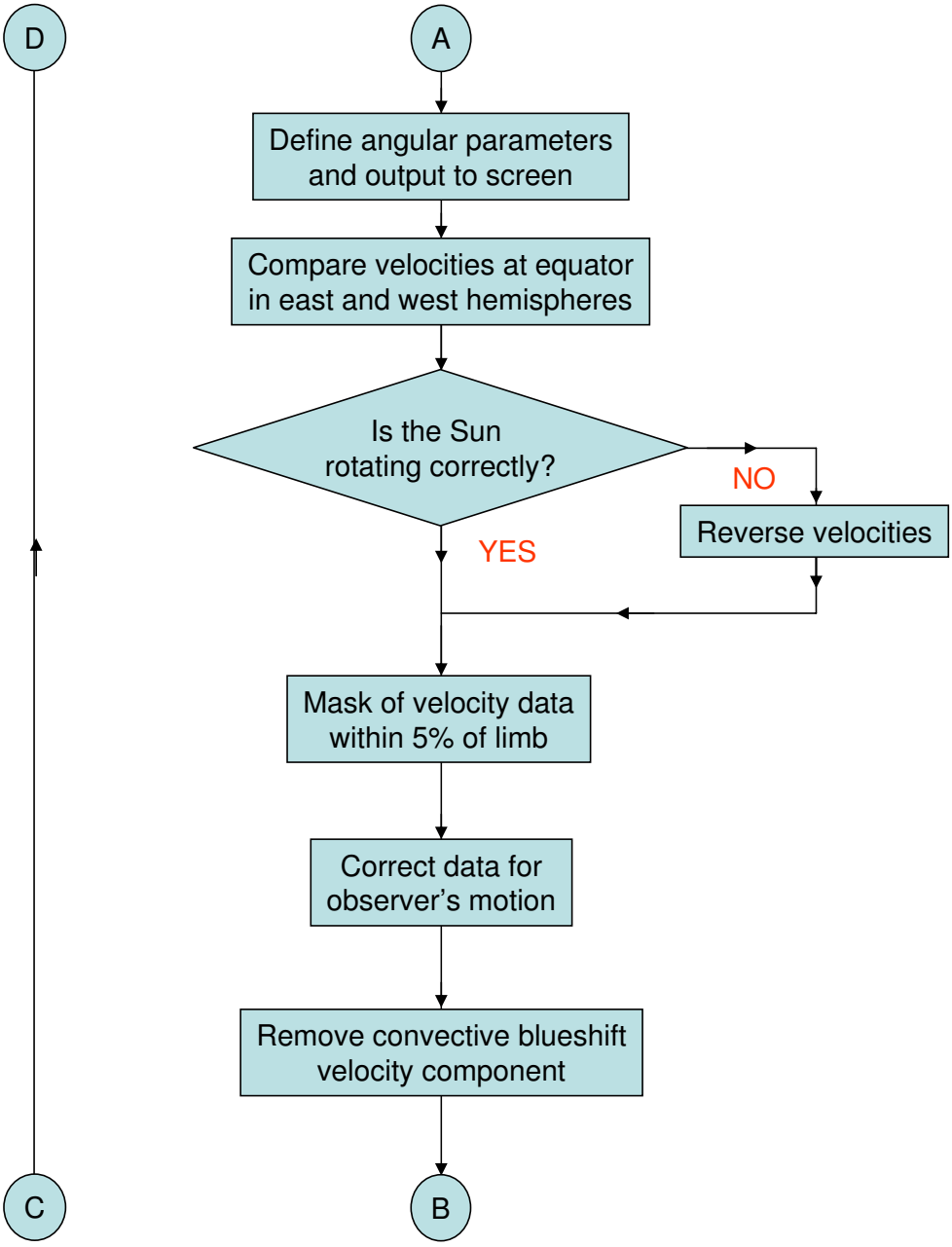
D
A
Define angular parameters and output to screen
Compare velocities at equator in east and west hemispheres
Is the Sun rotating correctly?
NO
Reverse velocities
YES
Mask of velocity data within 5% of limb
Correct data for observer's motion
Remove convective blueshift velocity component
C
B

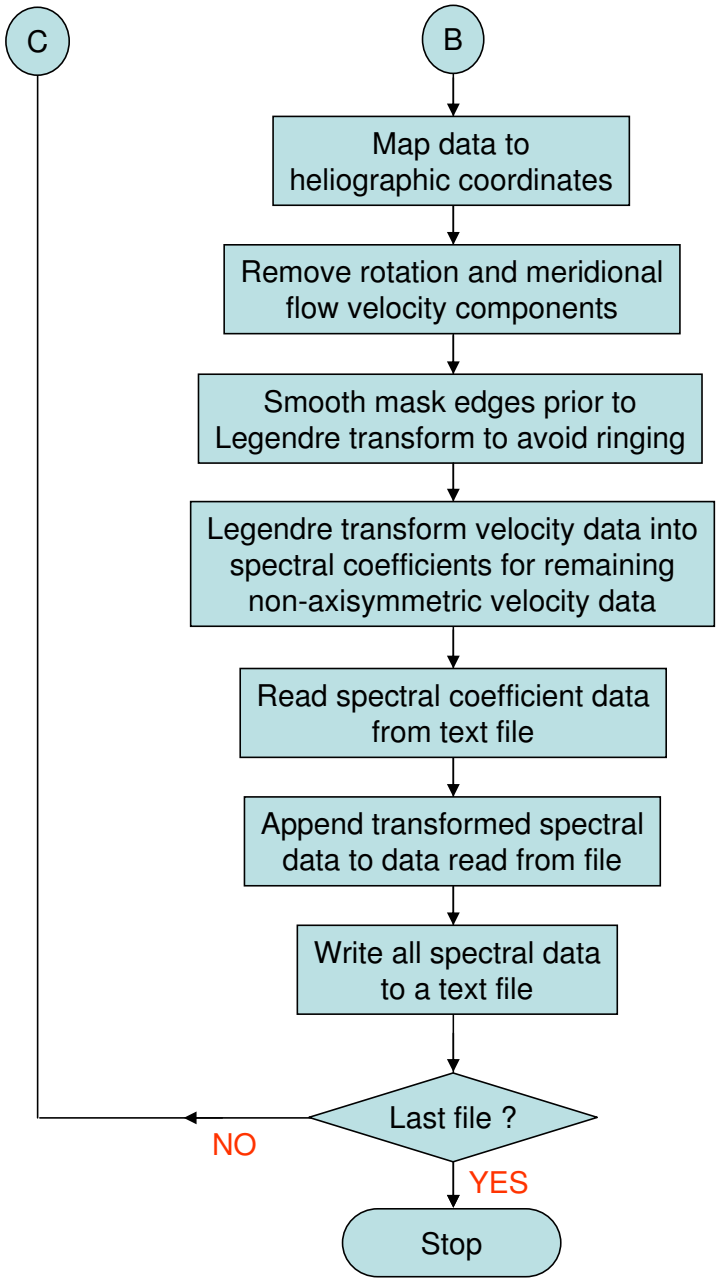
C
B
Map data to heliographic coordinates
Remove rotation and meridional flow velocity components
Smooth mask edges prior to Legendre transform to avoid ringing
Legendre transform velocity data into spectral coefficients for remaining non-axisymmetric velocity data
Read spectral coefficient data from text file
Append transformed spectral data to data read from file
Write all spectral data to a text file
Last file ?
NO
YES
Stop

APPENDIX B

COMPUTER CODE - PROGRAMS

MDI_fake.for

```
program mdi_fake
c**********************************************************************
c                                                                     *
c  file c:\MyProjects\mdi_fake\mdi_fake.for             11-03-05      *
c                                                                     *
c  This program creates 1024 by 1024 doppler velocity images of the   *
c  nearly steady photospheric flows. It constructs a spectrum of      *
c  spherical harmonic amplitudes  r(l,m), s(l,m) and  t(l,m), and     *
c  calculates the components of the velocity field at an array of     *
c  points in theta=colatitude and phi=longitude.                      *
c                                                                     *
c  The velocity vector (u,v,w) is in the (phi,theta,radius) direction. *
c                                                                     *
c  The vector velocities are then projected onto the line-of-sight    *
c  for a given B0, S0, X0, Y0, radius, and central meridian.          *
c                                                                     *
c  The line-of-sight velocities are then blurred and resampled at the  *
c  required resolution.                                               *
c                                                                     *
c  The data arrays are written to direct access disk files.           *
c                                                                     *
c                                                                     *
c**********************************************************************
parameter (nx=1024)
character fname*9,ext*5,path*16
complex*8 r(nx,nx),s(nx,nx),t(nx,nx)
complex*8 xi,arg,sum1,sum2,sum3,sum4,sum5,sum6
complex*8 unorth(2*nx),usouth(2*nx)
complex*8 vnorth(2*nx),vsouth(2*nx)
complex*8 wnorth(2*nx),wsouth(2*nx)
complex*8 fake(nx*nx),out(nx*nx)
real*4 u(2*nx+4,nx+4),v(2*nx+4,nx+4),w(2*nx+4,nx+4)
real*4 vobs(nx,nx),amp1(nx),amp2(nx),amp3(nx)
real*4 blur(7,7)
real*4 coef(nx,nx),p(nx)
real*4 mtfdata(nx*nx)
c
path='d:\soidata\fake\'
fname='datsim100'
ext='.data'
c
pi=4.*atan(1.0)
root3=sqrt(3.)
```

```
root5=sqrt(5.)
root7=sqrt(7.)
root9=sqrt(9.)
xi=(0.,1.)
c*************************************************************************
c                                                                        *
c  Differential rotation profile coefficients in radians/hour
c
c                                                                        *
c*************************************************************************
omega0=(15.0-1.)*pi/(24.*180.)
c omega2=-9.0*pi/(24.*180.)
omega2=0.
c omega4=4.0*pi/(24.*180.)
omega4=0
c*************************************************************************
c                                                                        *
c  Image size and position parameters .
c                                                                        *
c*************************************************************************
lmax=nx-2
nphi=2*nx
nxhalf=nx/2
nxsq=nx*nx
x0=512.5
y0=512.5
radius=502.0
write(*,*) 'Creating velocity images centered at '
write(*,*) 'X0 =',x0,' Y0 =',y0
write(*,*) 'With radius =',radius
c*************************************************************************
c                                                                        *
c Solar geometry parameters
c                                                                        *
c*************************************************************************
write(*,*) 'Solar parameters:'
c
c b0 = latitude in degrees at disk center
c
b0=0.0
c
c s0 = radius of solar disk in arcsec
c
s0 = 959.65/1.0019
write(*,*) 'B0=',b0,'  S0=',s0
br=b0*pi/180.
```

```
cosb0=cos(br)
sinb0=sin(br)
sr=s0*pi/(180.*3600.)
radsol=radius*cos(sr)
radsolsq=radsol*radsol
c
c scale = arc-radians per image pixel
c
scale=sr/radius
rsq=radius*radius
dphi=2.*pi/nphi
dtheta=pi/nx
c**********************************************************************
c                                                                     *
c  Read in modulation transfer function array                         *
c                                                                     *
c**********************************************************************
      open(unit=1, file='mtf.data', access='sequential',
     &    status='OLD',form='formatted')
        do j=1,nx
          read(1,*) (mtfdata(i+nx*(j-1)),i=1,nx)
        enddo
      close(1)
c**********************************************************************
c                                                                     *
c  Create spherical harmonic amplitudes for the nearly steady flows.  *
c                                                                     *
c**********************************************************************
call plmcoef(nx,coef)
write(*,*) 'Legendre recurrance coefficients calculated.'
c**********************************************************************
c                                                                     *
c  Read in the convection spectrum.                                   *
c                                                                     *
c**********************************************************************
open(unit=7,file='fakespec.txt',status='old')
  do l=1,lmax
    read(7,*) amp1(l),amp2(l),amp3(l)
    if (l .lt. 20) write(*,*) amp1(l),amp2(l),amp3(l)
  enddo
close(7)
c**********************************************************************
c
c Change idum to create different realization
c  Re-initialize random number sequence
c                                                                     *
```

```
c*********************************************************************
  idum=-1
c*********************************************************************
c                                                                     *
c  Create the spectrum for the rotation profile (toroidal flow).      *
c                                                                     *
c*********************************************************************
  write(*,*) 'calculating spectrum'
  m=0
  l=1
  t(l+1,m+1)=1483.
  l=3
  t(l+1,m+1)=-26.
  l=5
  t(l+1,m+1)=-4.
c*********************************************************************
c                                                                     *
c  Create the spectrum for the meridional circulation (poloidal flow). *
c                                                                     *
c*********************************************************************
  m=0
  l=2
  s(l+1,m+1)=17.
  l=4
  s(l+1,m+1)=-4.
c*********************************************************************
c                                                                     *
c  Construct the convection spectrum.                                 *
c                                                                     *
c*********************************************************************
    do l=1,lmax
c     do l=110,110
      l1=l+1
      el=float(l)
      do m=1,l
        m1=m+1
        phase=2.*pi*ran2(idum)
        arg=cos(phase)+xi*sin(phase)
c
c Use random amplitudes as well
c
    randamp=2.*ran2(idum)
    r(l1,m1)=-1.*randamp*amp1(l)*arg
    s(l1,m1)=randamp*amp2(l)*arg
    t(l1,m1)=randamp*amp3(l)*arg
      enddo
```

```
    enddo
  write(*,*) 'Velocity spectrum calculated'
c**********************************************************************
c                                                                      *
c  Calculate the vector velocity components at each latitude.
c  Equator is at jj=nx/2 + 2.5 due to wrap-around border
c  j=1 is centered 0.5*dtheta above and below the equator
c  j=nxhalf is centered 0.5*dtheta inside each pole
c                                                                      *
c**********************************************************************
do j=1,nxhalf
  write(*,*) ' line ',j,' of ',nxhalf,' started'
  jn=nxhalf+2+j
  js=nxhalf+3-j
  theta=0.5*pi-(j-0.5)*dtheta
  x=cos(theta)
  sintheta=sin(theta)
  rst=1.0/sintheta
c**********************************************************************
c                                                                      *
c  calculate the spectral coefficients for wavenumber m at all x.      *
c                                                                      *
c**********************************************************************
  m=0
  m1=m+1
  call plm(m,x,nx,coef,p)
  sum1=(0.,0.)
  sum2=(0.,0.)
  sum3=(0.,0.)
  sum4=(0.,0.)
  sum5=(0.,0.)
  sum6=(0.,0.)
  do l=1,lmax-1
    l1=l+1
    l2=l+2
    ieo=1-2*mod(l-m,2)
    v1=l*p(l2)/coef(l2,m1)-(l+1.)*p(l)/coef(l1,m1)
    sum1=sum1-t(l1,m1)*v1
    sum2=sum2+ieo*t(l1,m1)*v1
    sum3=sum3+s(l1,m1)*v1
    sum4=sum4-ieo*s(l1,m1)*v1
    sum5=sum5+r(l1,m1)*p(l1)
    sum6=sum6+ieo*r(l1,m1)*p(l1)
  enddo
  unorth(m1)=sum1*rst
  usouth(m1)=sum2*rst
```

```
  vnorth(m1)=sum3*rst
  vsouth(m1)=sum4*rst
  wnorth(m1)=sum5
  wsouth(m1)=sum6
c*********************************************************************
c                                                                    *
c  Split non-axisymmetric signal into equal positive and             *
c  negative freqencies.                                              *
c                                                                    *
c*********************************************************************
  do m=1,lmax-1
    m1=m+1
    m2=nphi+1-m
    call plm(m,x,nx,coef,p)
    sum1=(0.,0.)
    sum2=(0.,0.)
    sum3=(0.,0.)
    sum4=(0.,0.)
    sum5=(0.,0.)
    sum6=(0.,0.)
    do l=m,lmax-1
      l1=l+1
      l2=l+2
      ieo=1-2*mod(l-m,2)
      v1=l*p(l2)/coef(l2,m1)-(l+1.)*p(l)/coef(l1,m1)
      v2=-m*p(l1)
      sum1=sum1+xi*s(l1,m1)*v2-t(l1,m1)*v1
      sum2=sum2+ieo*(xi*s(l1,m1)*v2+t(l1,m1)*v1)
      sum3=sum3+s(l1,m1)*v1+xi*t(l1,m1)*v2
      sum4=sum4-ieo*(s(l1,m1)*v1-xi*t(l1,m1)*v2)
      sum5=sum5+r(l1,m1)*p(l1)
      sum6=sum6+ieo*r(l1,m1)*p(l1)
    enddo
    unorth(m1)=0.5*sum1*rst
    usouth(m1)=0.5*sum2*rst
    unorth(m2)=0.5*conjg(sum1)*rst
    usouth(m2)=0.5*conjg(sum2)*rst
    vnorth(m1)=0.5*sum3*rst
    vsouth(m1)=0.5*sum4*rst
    vnorth(m2)=0.5*conjg(sum3)*rst
    vsouth(m2)=0.5*conjg(sum4)*rst
    wnorth(m1)=0.5*sum5
    wsouth(m1)=0.5*sum6
    wnorth(m2)=0.5*conjg(sum5)
    wsouth(m2)=0.5*conjg(sum6)
  enddo
```

```
  do m=lmax,nphi-lmax
    m1=m+1
    unorth(m1)=0.
    usouth(m1)=0.
    vnorth(m1)=0.
    vsouth(m1)=0.
    wnorth(m1)=0.
    wsouth(m1)=0.
  enddo
c*********************************************************************
c                                                                    *
c  Calculate the vector velocity components at all phi positions.    *
c                                                                    *
c*********************************************************************
  call four1(unorth,nphi,-1)
  call four1(usouth,nphi,-1)
  call four1(vnorth,nphi,-1)
  call four1(vsouth,nphi,-1)
  call four1(wnorth,nphi,-1)
  call four1(wsouth,nphi,-1)
  do i=1,nphi
    u(i,jn)=real(unorth(i))
    u(i,js)=real(usouth(i))
    v(i,jn)=real(vnorth(i))
    v(i,js)=real(vsouth(i))
    w(i,jn)=real(wnorth(i))
    w(i,js)=real(wsouth(i))
  enddo
enddo
c*********************************************************************
c                                                                     *
c  Add 2-pixel wrap-around border to velocity arrays for interpolation  *
c                                                                     *
c*********************************************************************
np1=nphi+1
np2=nphi+2
np3=nphi+3
np4=nphi+4
do j=3,nx+2
  u(np1,j)=u(1,j)
  v(np1,j)=v(1,j)
  w(np1,j)=w(1,j)
  u(np2,j)=u(2,j)
  v(np2,j)=v(2,j)
  w(np2,j)=w(2,j)
  u(np3,j)=u(3,j)
```

```
  v(np3,j)=v(3,j)
  w(np3,j)=w(3,j)
  u(np4,j)=u(4,j)
  v(np4,j)=v(4,j)
  w(np4,j)=w(4,j)
enddo
np2=nphi/2+2
nx1=nx+1
nx2=nx+2
nx3=nx+3
nx4=nx+4
do i=1,np2
  i2=np2+i-1
  u(i,2)=u(i2,3)
  v(i,2)=v(i2,3)
  w(i,2)=w(i2,3)
  u(i,1)=u(i2,4)
  v(i,1)=v(i2,4)
  w(i,1)=w(i2,4)
  u(i2,2)=u(i,3)
  v(i2,2)=v(i,3)
  w(i2,2)=w(i,3)
  u(i2,1)=u(i,4)
  v(i2,1)=v(i,4)
  w(i2,1)=w(i,4)
  u(i,nx3)=u(i2,nx2)
  v(i,nx3)=v(i2,nx2)
  w(i,nx3)=w(i2,nx2)
  u(i,nx4)=u(i2,nx1)
  v(i,nx4)=v(i2,nx1)
  w(i,nx4)=w(i2,nx1)
  u(i2,nx3)=u(i,nx2)
  v(i2,nx3)=v(i,nx2)
  w(i2,nx3)=w(i,nx2)
  u(i2,nx4)=u(i,nx1)
  v(i2,nx4)=v(i,nx1)
  w(i2,nx4)=w(i,nx1)
enddo
write(*,*) 'Vector velocity arrays calculated.'
c**********************************************************************
c                                                                     *
c  Write radial velocity velocity to disk file.                       *
c                                                                     *
c**********************************************************************
  n1000=int(ifile/1000)
  n100=int((ifile-1000*n1000)/100)
```

```
  n10=int((ifile-1000*n1000-100*n100)/10)
  n1=ifile-1000*n1000-100*n100-10*n10
  fname='radial' // char(48+n100) // char(48+n10) //char(48+n1)
  open(unit=1,file=path // fname // ext,access='direct',
     &       status='unknown',recl=2*nx)
  do j=1,nx
    write(1,rec=j) (w(i+1,j+1),i=1,2*nx)
  enddo
  close(1)
umax=0.0
vmax=0.0
wmax=0.0
do j=3,nx+2
  do i=3,nphi+2
    utest=abs(u(i,j))
    if (utest .gt. umax) umax=utest
    vtest=abs(v(i,j))
    if (vtest .gt. vmax) vmax=vtest
    wtest=abs(w(i,j))
    if (wtest .gt. wmax) wmax=wtest
  enddo
enddo
write(*,*) 'Umax, Vmax, Wmax =',umax,vmax,wmax
c**********************************************************************
c                                                                     *
c  Construct blurring array.                                          *
c                                                                     *
c**********************************************************************
      btotal=0.0
      asq=2.0**2
      bsq=4.0**2
do j=1,7
  y=j-4.
  do i=1,7
    x=i-4.
    r2=x*x+y*y
c          blur(i,j) = exp(-r2/(2.*asq)) -
c     &      exp(-bsq/(2.*asq))*(1. + bsq/(2.*asq) - r2/(2.*asq))
 blur(i,j)=1./49.
    btotal=btotal+blur(i,j)
  enddo
enddo
do j=1,7
  do i=1,7
    blur(i,j)=blur(i,j)/btotal
  enddo
```

```
enddo
c*************************************************************************
c
c  Construct series of images with different central meridians
c
c*************************************************************************
do itime=1,30*24*4
  ifile=1000+(itime-1)
  hours=float(itime)/4.
  phi0=180.-13.5*hours/24.
  phi0r=phi0*pi/180.
c*************************************************************************
c                                                                        *
c  Calculate the line-of-sight velocity for a tilt angle b0 and central*
c  meridian longitude phi0.                                             *
c                                                                        *
c*************************************************************************
  jmin=int(y0-radius)+1
  jmax=int(y0+radius)
  do j=jmin,jmax
    yimg=(j-0.5)-y0
    hchord=0.
    arg1=rsq-yimg*yimg
    if (arg1 .gt. 0.) hchord=sqrt(arg1)
    imin=nint(x0-hchord)
    imax=nint(x0+hchord)
    do i=imin,imax
      ximg=(i-0.5)-x0
c*************************************************************************
c                                                                        *
c  Find the latitude and longitude at the center of 49 sub-pixels.      *
c                                                                        *
c*************************************************************************
      btotal=0.0
      vlos=0.0
      pwidth=0.7
      do jj=1,7
c
c Average over a 2x2 pixel area
c         y1=yimg+pwidth*(jj-4.)/3.
c
c Average over a 1x1 pixel area
        y1=yimg+pwidth*(jj-4.)/7.
        do ii=1,7
          blurry=blur(ii,jj)
c
```

```
c Average over a 2x2 pixel area
c           x1=ximg+pwidth*(ii-4.)/3.
c
c Average over a 1x1 pixel area
          x1=ximg+pwidth*(ii-4.)/7.
c
c Find radius from disk center in pixels
c
          risq=x1*x1 + y1*y1
          rho_i=sqrt(risq)
c
c Find radius from disk center in ard-radians
c  (scale = arc-radians per image pixel)
c
          rho1=scale*rho_i
          sinrho1=sin(rho1)
          cosrho1=cos(rho1)
c
c Test to see if pixel is on disk
c
          r_test=rho_i*cosrho1
          if (r_test .lt. radsol) then
          btotal=btotal+blurry
c
c Observed position angle clockwise from vertical (yi axis)
c
          pangle=0.
          if (risq .ne. 0.) pangle=atan2(-x1,y1)
c
c Heliographic cartesian coordinates
c
          factor1=sqrt(radsolsq-r_test*r_test)
          rho_p=rho_i*cosrho1*cosrho1-factor1*sinrho1

          xp=rho_p*sin(pangle)
          yp=rho_p*cos(pangle)
          rpsq=xp*xp + yp*yp
          zp=sqrt(radsolsq - rpsq)
c
c Rotated Heliographic cartesian coordinates with B-angle removed
c
          xs=xp
          ys=cosb0*yp + sinb0*zp
          zs=cosb0*zp - sinb0*yp
c
c Heliographic latitude and longitude in radians
```

```
c
          xlat=asin(ys/radsol)
          xlon=0.
          rssq=xs*xs+zs*zs
          if (rssq .ne. 0.) xlon=atan2(-xs,zs)
c
c Trigonometric factors
c
          sinb=sin(xlat)
          cosb=cos(xlat)
          sinphi=sin(xlon)
          cosphi=cos(xlon)
c
c  Bi-cubic interpolation from adjacent points.
c
          xlon=xlon+phi0r
          if (xlon .lt. 0.) xlon=2.*pi + xlon
          if (xlon .gt. 2.*pi) xlon=xlon - 2.*pi
          xm=2.5 + xlon/dphi
          ym=2.5 + nx/2. + xlat/dtheta
          ixm=int(xm)
          iym=int(ym)
          dx=xm-ixm
          dy=ym-iym
c
c Weights for bi-cubic interpolation
c
                  dx2=dx*dx
                  dx3=dx*dx2
                  dy2=dy*dy
                  dy3=dy*dy2
                  wx0=-0.5*dx + dx2 - 0.5*dx3
                  wy0=-0.5*dy + dy2 - 0.5*dy3
                  wx1=1.0 - 2.5*dx2 + 1.5*dx3
                  wy1=1.0 - 2.5*dy2 + 1.5*dy3
                  wx2=0.5*dx + 2.*dx2 - 1.5*dx3
                  wy2=0.5*dy + 2.*dy2 - 1.5*dy3
                  wx3=-0.5*dx2 + 0.5*dx3
                  wy3=-0.5*dy2 + 0.5*dy3
c
c U component interploation
c
                  f00=u(ixm-1,iym-1)
                  f10=u(ixm+0,iym-1)
                  f20=u(ixm+1,iym-1)
                  f30=u(ixm+2,iym-1)
```

```
                  f01=u(ixm-1,iym)
                  f11=u(ixm+0,iym)
                  f21=u(ixm+1,iym)
                  f31=u(ixm+2,iym)
                  f02=u(ixm-1,iym+1)
                  f12=u(ixm+0,iym+1)
                  f22=u(ixm+1,iym+1)
                  f32=u(ixm+2,iym+1)
                  f03=u(ixm-1,iym+2)
                  f13=u(ixm+0,iym+2)
                  f23=u(ixm+1,iym+2)
                  f33=u(ixm+2,iym+2)
                  utemp = wx0*wy0*f00 + wx1*wy0*f10 +
     &              wx2*wy0*f20 + wx3*wy0*f30 + wx0*wy1*f01 +
     &              wx1*wy1*f11 + wx2*wy1*f21 + wx3*wy1*f31 +
     &              wx0*wy2*f02 + wx1*wy2*f12 + wx2*wy2*f22 +
     &              wx3*wy2*f32 + wx0*wy3*f03 + wx1*wy3*f13 +
     &              wx2*wy3*f23 + wx3*wy3*f33

c
c V component interploation
c
                  f00=v(ixm-1,iym-1)
                  f10=v(ixm+0,iym-1)
                  f20=v(ixm+1,iym-1)
                  f30=v(ixm+2,iym-1)
                  f01=v(ixm-1,iym)
                  f11=v(ixm+0,iym)
                  f21=v(ixm+1,iym)
                  f31=v(ixm+2,iym)
                  f02=v(ixm-1,iym+1)
                  f12=v(ixm+0,iym+1)
                  f22=v(ixm+1,iym+1)
                  f32=v(ixm+2,iym+1)
                  f03=v(ixm-1,iym+2)
                  f13=v(ixm+0,iym+2)
                  f23=v(ixm+1,iym+2)
                  f33=v(ixm+2,iym+2)
                  vtemp = wx0*wy0*f00 + wx1*wy0*f10 +
     &              wx2*wy0*f20 + wx3*wy0*f30 + wx0*wy1*f01 +
     &              wx1*wy1*f11 + wx2*wy1*f21 + wx3*wy1*f31 +
     &              wx0*wy2*f02 + wx1*wy2*f12 + wx2*wy2*f22 +
     &              wx3*wy2*f32 + wx0*wy3*f03 + wx1*wy3*f13 +
     &              wx2*wy3*f23 + wx3*wy3*f33

c
```

```
c W component interploation
c
                  f00=w(ixm-1,iym-1)
                  f10=w(ixm+0,iym-1)
                  f20=w(ixm+1,iym-1)
                  f30=w(ixm+2,iym-1)
                  f01=w(ixm-1,iym)
                  f11=w(ixm+0,iym)
                  f21=w(ixm+1,iym)
                  f31=w(ixm+2,iym)
                  f02=w(ixm-1,iym+1)
                  f12=w(ixm+0,iym+1)
                  f22=w(ixm+1,iym+1)
                  f32=w(ixm+2,iym+1)
                  f03=w(ixm-1,iym+2)
                  f13=w(ixm+0,iym+2)
                  f23=w(ixm+1,iym+2)
                  f33=w(ixm+2,iym+2)
                  wtemp = wx0*wy0*f00 + wx1*wy0*f10 +
     &              wx2*wy0*f20 + wx3*wy0*f30 + wx0*wy1*f01 +
     &              wx1*wy1*f11 + wx2*wy1*f21 + wx3*wy1*f31 +
     &              wx0*wy2*f02 + wx1*wy2*f12 + wx2*wy2*f22 +
     &              wx3*wy2*f32 + wx0*wy3*f03 + wx1*wy3*f13 +
     &              wx2*wy3*f23 + wx3*wy3*f33

c**********************************************************************
c                                                                     *
c  Calculate velocity projection factors.      *
c                                                                     *
c**********************************************************************
          uproj=cosb0*sinphi
          vproj=sinb0*cosb-cosb0*sinb*cosphi
          wproj=sinb0*sinb+cosb0*cosb*cosphi
c**********************************************************************
c                                                                     *
c  Interpolate vlos from adjacent pixels.      *
c  Set npix=4 so these values are weighted more than integral pixels.  *
c                                                                     *
c**********************************************************************
          vlos=vlos+uproj*utemp*blurry
          vlos=vlos+vproj*vtemp*blurry
          vlos=vlos+wproj*wtemp*blurry
          endif
        enddo
      enddo
      vobs(i,j)=0.0
```

```
      if (btotal .ne. 0.0) vobs(i,j)=vlos/btotal
c**********************************************************************
c                                                                      *
c  Add convective blue shift.                                          *
c                                                                      *
c**********************************************************************
      rr=ximg*ximg+yimg*yimg
      xvar=1.
      if (rr .lt. rsq) xvar=1.-sqrt(1.-rr/rsq)
      pstar1=root3*(2.*xvar-1.)
      pstar2=root5*(6.*xvar**2-6.*xvar+1.)
      pstar3=root7*(20.*xvar**3-30.*xvar**2+12.*xvar-1.)
      vobs(i,j)=vobs(i,j)+161.*pstar1+85.*pstar2+11.*pstar3
c**********************************************************************
c                                                                      *
c  Add Noise                                                           *
c                                                                      *
c**********************************************************************
c noise=0.0
c vobs(i,j)=vobs(i,j)+noise*gasdev(idum)
    enddo
  enddo
c**********************************************************************
c                                                                      *
c  Blur data                                                           *
c                                                                      *
c**********************************************************************
  do j=1,nx
    do i=1,nx
      fake(i+nx*(j-1))=cmplx(vobs(i,j))
    enddo
  enddo


  call four1(fake,nxsq,1)

  do j=1,nxsq
    out(j)=fake(j)*mtfdata(j)/nxsq
  enddo

  call four1(out,nxsq,-1)

  do j=1,nx
    do i=1,nx
      vobs(i,j) = real(out(i+nx*(j-1)))
    enddo
```

```
  enddo
c*********************************************************************
c                                                                     *
c  Write observed velocity to disk file.                              *
c                                                                     *
c*********************************************************************
  n1000=int(ifile/1000)
  n100=int((ifile-1000*n1000)/100)
  n10=int((ifile-1000*n1000-100*n100)/10)
  n1=ifile-1000*n1000-100*n100-10*n10
  fname='blur_' // char(48+n1000) // char(48+n100) //
     &    char(48+n10) //char(48+n1)
  write(*,*) 'Completed file ',fname
  open(unit=1,file=path // fname // ext,access='direct',
     &       status='unknown',recl=nx)
  do j=1,nx
    write(1,rec=j) (vobs(i,j),i=1,nx)
  enddo
  close(1)
enddo
end
```

```
FUNCTION RAN2(IDUM)
C*********************************************************************
C                                                                     *
C  THIS IS THE RANDOM NUMBER GENERATOR FROM "NUMERICAL RECIPES"       *
C                                                                     *
C*********************************************************************
PARAMETER (M=714025,IA=1366,IC=150889,RM=1./M)
DIMENSION IR(97)
DATA IFF /0/
IF(IDUM.LT.0.OR.IFF.EQ.0)THEN
    IFF=1
    IDUM=MOD(IC-IDUM,M)
    DO J=1,97
IDUM=MOD(IA*IDUM+IC,M)
IR(J)=IDUM
    ENDDO
    IY=IDUM
ENDIF
J=1+(97*IY)/M
IF(J.GT.97.OR.J.LT.1)PAUSE
IY=IR(J)
```

```
RAN2=IY*RM
IDUM=MOD(IA*IDUM+IC,M)
IR(J)=IDUM
RETURN
END
FUNCTION GASDEV(IDUM)
C**********************************************************************
C                                                                     *
C  Returns a normally distributed deviate with zero mean and unit     *
C  variance. Uses RAN2(IDUM) as the source of uniform deviates.       *
C                                                                     *
c**********************************************************************
DATA ISET/0/
IF (ISET .EQ. 0) THEN
1           V1=2.*RAN2(IDUM)-1.
    V2=2.*RAN2(IDUM)-1.
    R=V1**2+V2**2
    IF (R .GT. 1.) GOTO 1
    FAC=SQRT(-2.*LOG(R)/R)
    GSET=V1*FAC
    GASDEV=V2*FAC
    ISET=1
ELSE
    GASDEV=GSET
    ISET=0
ENDIF
RETURN
END
```

MDI_analysis1.for

```
      program mdi_analysis1
c**********************************************************************
c                                                                     *
c Analyzes Doppler velocity data to extract spectral coefficients     *
c and velocity profiles. Input files include velocity and             *
c intensity images and NSO magnetogram synoptic maps. Intensity is    *
c used to determine image parameters (center coordinates x0 and y0,   *
c radius, ellipticity, and orientation of elliptical figure for limb). *
c The magnetograms are used to produce a data mask which covers active *
c regions.                                                            *
c                                                                     *
c Output includes a formatted file containing spectral coefficients   *
c                                                                     *
c**********************************************************************

c     dtype=1: Real data; dtype=0: Fake data
c      parameter (nx=1024, lmaxp=1024, dtype=1)
      parameter (nx=1024, lmaxp=1024, dtype=0)

      complex*8 work1(2*nx),work2(lmaxp,nx)
      real*4 v(nx,nx),vmap(nx,nx),vtemp(nx,nx)
c      real*4 bimage(nx,nx)
      real*4 vls(nx),vphi(nx),vtheta(nx),spcoef(nx)
      real*4 mask1(nx,nx),mask2(nx,nx)
      real*4 p(lmaxp),coef(lmaxp,lmaxp)
      real*4 t(15),s(15),cls(6)
      real*4 c(15),angles(6)
      real*4 rbuffer(720)
character mday*4,mhour*2
c character magnum*4
      byte buffer(2880)
      character filename*4,ext*5,hdr*2880,hdrrec*80
c character path*27
c      path='d:\soidata\1996DynamicsRun\'
c character path*16
c      path='d:\soidata\sim5\'

      pi=4.0*atan(1.0)
      root3=sqrt(3.)
      root5=sqrt(5.)
      root7=sqrt(7.)
      datamask=-32768.
```

```
c*********************************************************************
c                                                                     *
c Calculate matrix of coefficients for Associated Legendre polynomials.*
c                                                                     *
c*********************************************************************
      call plmcoef(lmaxp,coef)
      write(*,*) 'Coefficients for Legendre polynomials calculated.'

c*********************************************************************
c                                                                     *
c  Fractional radius for limits of data analysis.                     *
c                                                                     *
c*********************************************************************
      sinrho = 0.99

c*********************************************************************
c                                                                     *
c  List of data files for analysis.                                   *
c                                                                     *
c*********************************************************************
      open(unit=7,name='analysis.inp',status='old')

10    continue
      read(7,1001,END=9999) filename
1001    format(a4)

      if (dtype .eq. 1) then
c   mday=filename(1:4)
c       Change mday to the directory number
  mday='1240'
  mhour=filename(3:4)
  time = 1000.*(ichar(mday(1:1))-48.) - 1239. +
     &    100.*(ichar(mday(2:2))-48.) +
     &    10.*(ichar(mday(3:3))-48.) +
     &    1.*(ichar(mday(4:4))-48.) +
     &    (10.*(ichar(mhour(1:1))-48.)+1.*(ichar(mhour(2:2))-48.))/96.
  write(*,*) 'Time in days = ',time
        ext = '.fits'
        write(*,*) 'Processing ',filename,ext
c*********************************************************************
c                                                                     *
c Read in Doppler velocity array.                                     *
c                                                                     *
c*********************************************************************
        open(unit=8,name='temp.txt',status='old')
```

```
 1003   format(a19)
 1004   format(g19.12)
        open(unit=9,name=filename // ext,status='OLD',
     &       access='direct',recl=4*720)
c*************************************************************************
c                                                                        *
c Read in header information.                                            *
c                                                                        *
c*************************************************************************
        do nrec=1,5
          read(9,rec=nrec) hdr
          do i=1,36
       hdrrec=hdr((i-1)*80+1:i*80)
       rewind(8)
       if (hdrrec(1:8) .eq. 'OBS_DIST') then
         write(8,1003) hdrrec(12:30)
         rewind(8)
         read(8,1004) rdist_au
       endif
       if (hdrrec(1:6) .eq. 'OBS_B0') then
         write(8,1003) hdrrec(12:30)
         rewind(8)
               read(8,1004) b0
       endif
       if (hdrrec(1:6) .eq. 'OBS_L0') then
         write(8,1003) hdrrec(12:30)
         rewind(8)
               read(8,1004) clon
       endif
       if (hdrrec(1:6) .eq. 'OBS_VR') then
         write(8,1003) hdrrec(12:30)
         rewind(8)
               read(8,1004) c0
       endif
       if (hdrrec(1:6) .eq. 'OBS_VN') then
         write(8,1003) hdrrec(12:30)
         rewind(8)
               read(8,1004) cy
       endif
       if (hdrrec(1:6) .eq. 'OBS_VW') then
         write(8,1003) hdrrec(12:30)
         rewind(8)
               read(8,1004) cx
       endif
       if (hdrrec(1:8) .eq. 'MAP_RSUN') then
         write(8,1003) hdrrec(12:30)
```

```
        rewind(8)
              read(8,1004) radius
      endif
      if (hdrrec(1:6) .eq. 'MAP_X0') then
        write(8,1003) hdrrec(12:30)
        rewind(8)
              read(8,1004) x0
      endif
      if (hdrrec(1:6) .eq. 'MAP_Y0') then
        write(8,1003) hdrrec(12:30)
        rewind(8)
              read(8,1004) y0
      endif
      if (hdrrec(1:6) .eq. 'BSCALE') then
        write(8,1003) hdrrec(12:30)
        rewind(8)
              read(8,1004) bscale
      endif
      if (hdrrec(1:5) .eq. 'BZERO') then
        write(8,1003) hdrrec(12:30)
        rewind(8)
              read(8,1004) bzero
      endif
            if (hdrrec(1:3) .eq. 'END') goto 20
          enddo
        enddo
 20     nskip=nrec
        close(8)
c**************************************************************************
c                                                                         *
c Read in velocity array.                                                 *
c                                                                         *
c**************************************************************************
        vmax=-1.0e+30
        vmin=1.0e+30
c**************************************************************************
c                                                                         *
c Integer data                                                            *
c                                                                         *
c**************************************************************************
        nrec=int((1024.*1024.)/1440.)
        do jrec=1,nrec
          read(9,rec=nskip+jrec) (buffer(icol),icol=1,2880)
          do k=1,1440
            nelem=(jrec-1)*1440 + k
            j=1+(nelem-1)/1024
```

```
            i=nelem-(j-1)*1024
            value=float(buffer(2*k)) + 256.*float(buffer(2*k-1))
            if (buffer(2*k) .lt. 0) value=value+256.
            v(i,j)=bzero+bscale*value
            if(v(i,j) .gt. vmax) vmax=v(i,j)
            if(v(i,j) .lt. vmin) vmin=v(i,j)
          enddo
        enddo
        close(9)
        s0 = 959.65/rdist_au
        cy = -cy*sin(s0*pi/(180.*3600.))
        cx = -cx*sin(s0*pi/(180.*3600.))
        datamask = -32768.*bscale + bzero
c*************************************************************************
c                                                                        *
c Real*4 data                                                            *
c                                                                        *
c*************************************************************************
c      nrec=int((1024.*1024.)/720.)
c      do jrec=1,nrec
c  read(9,rec=nskip+jrec) (rbuffer(icol),icol=1,720)
c do k=1,720
c   nelem=(jrec-1)*720 + k
c   j=1+(nelem-1)/1024
c   i=nelem-(j-1)*1024
c   v(i,j)=rbuffer(k)
c          if(v(i,j) .gt. vmax) vmax=v(i,j)
c          if(v(i,j) .lt. vmin) vmin=v(i,j)
c enddo
c      enddo
c      close(9)
c*************************************************************************
c                                                                        *
c Change observer's motion to reflect observed values.                   *
c                                                                        *
c*************************************************************************
  c0=c0-4.57*time
  cx=cx-0.37*time
  cy=cy+18.4-0.16*time
c*************************************************************************
c                                                                        *
c Correct (x0,y0) for FORTRAN counting system ((1.,1.) at lower left).   *
c                                                                        *
c*************************************************************************
  x0 = x0 + 1.0
  y0 = y0 + 1.0
```

```
  rsq=radius*radius
c*************************************************************************
c                                                                        *
c  Correct velocity signal for center-to-limb line variation.            *
c                                                                        *
c*************************************************************************
        jmin0=int(y0+1.-radius)
        jmax0=int(y0+radius)
        do j=jmin0,jmax0
          yp=(j-0.5)-y0
          hchord=sqrt(rsq-yp*yp)
          imin=int(x0+1.0-hchord)
          imax=int(x0+hchord)
          do i=imin,imax
            xp=(i-0.5)-x0
            rp=xp*xp+yp*yp
            r2=rp/rsq
      x=sqrt(r2)
      v(i,j)=(1.00+0.10*x*x*x)*v(i,j)
    enddo
  enddo
endif
c*************************************************************************
c                                                                         *
c fakedata                                                                *
c                                                                         *
c*************************************************************************
      if (dtype .eq. 0) then
        ext='.data'
        b0=0.0
        s0=959.65/1.0019
        c0=0.0
        c2=0.0
        cx=0.0
        cy=0.0
        radius=502.0
        rsq=radius*radius
        x0=512.5
        y0=512.5
        ellips=1.0
        eangle=0.0
        pangle=0.0
        open(unit=3,file=filename // ext,status='OLD',
     &    access='direct',recl=4*nx)
        vmax=-1.0e+30
        vmin=1.0e+30
```

```
      do j=1,nx
        read(3,rec=j) (v(i,j),i=1,nx)
        do i=1,nx
          if(v(i,j) .gt. vmax) vmax=v(i,j)
          if(v(i,j) .lt. vmin) vmin=v(i,j)
        enddo
      enddo
      close(3)
    endif

    sins0=sin(s0*pi/(180.*3600.))
    ellips=1.0
    eangle=0.0
    pangle=0.0

    angles(1)=s0
    angles(2)=b0
    angles(3)=pangle
    angles(4)=eangle
    angles(5)=ellips
    angles(6)=sinrho

    write(*,*) 'Semi-diameter, s0, in arc-seconds, is ',s0
    write(*,*) 'Rotation axis tilt, b0, in degrees, is ',b0
    write(*,*) '************ observer motion *************'
    write(*,*) '             c0=',c0
    write(*,*) '             cx=',cx
    write(*,*) '             cy=',cy


    fov=nx*s0/radius
    write(*,*) '************ image parameters *************'
    write(*,*) '                x0=',x0
    write(*,*) '                y0=',y0
    write(*,*) '            radius=',radius
    write(*,*) '            pangle=',pangle
    write(*,*) '            ellips=',ellips
    write(*,*) '            eangle=',eangle
    write(*,*) 'Velocity max and min = ',vmax,vmin

    if (v(512-400,512) .gt. v(512+400,512)) then
do j=1,nx
  do i=1,nx
    v(i,j)=-1.*v(i,j)
  enddo
enddo
```

```
      endif

c*************************************************************************
c                                                                        *
c Construct initial data mask.                                           *
c                                                                        *
c*************************************************************************
total=0
do j=1,nx
  y=(j-0.5)-y0
  do i=1,nx
    x=(i-0.5)-x0
    mask1(i,j)=1.
    r2=x*x+y*y
    if (r2 .gt. sinrho*sinrho*rsq) mask1(i,j)=0.
    if (v(i,j) .eq. datamask) mask1(i,j)=0.
    total=total+mask1(i,j)
    mask2(i,j)=mask1(i,j)
  enddo
enddo
      write(*,*) 'Total unmasked pixels = ',total

c*************************************************************************
c                                                                        *
c  Produce active region mask from magnetograms.                         *
c                                                                        *
c*************************************************************************
c      if (mhour .eq. '00') magnum='0000'
c      if (mhour .eq. '01') magnum='0001'
c      if (mhour .eq. '02') magnum='0001'
c      if (mhour .eq. '03') magnum='0002'
c      if (mhour .eq. '04') magnum='0002'
c      if (mhour .eq. '05') magnum='0003'
c      if (mhour .eq. '06') magnum='0004'
c      if (mhour .eq. '07') magnum='0004'
c      if (mhour .eq. '08') magnum='0005'
c      if (mhour .eq. '09') magnum='0006'
c      if (mhour .eq. '10') magnum='0006'
c      if (mhour .eq. '11') magnum='0007'
c      if (mhour .eq. '12') magnum='0008'
c      if (mhour .eq. '13') magnum='0008'
c      if (mhour .eq. '14') magnum='0009'
c      if (mhour .eq. '15') magnum='0009'
c      if (mhour .eq. '16') magnum='0010'
c      if (mhour .eq. '17') magnum='0011'
c      if (mhour .eq. '18') magnum='0011'
```

```
c      if (mhour .eq. '19') magnum='0012'
c      if (mhour .eq. '20') magnum='0012'
c      if (mhour .eq. '21') magnum='0013'
c      if (mhour .eq. '22') magnum='0014'
c      if (mhour .eq. '23') magnum='0014'
c
c      call mdi_mag(nx,mday,magnum,bimage)
c
c      bmask=50.
c      call magmask(nx,bmask,bimage,mask2)
c
c      call moremask(nx,mask2)

       do j=1,nx
         do i=1,nx
           mask1(i,j)= mask1(i,j)*mask2(i,j)
         enddo
       enddo

       write(*,*) 'Data masks constructed.'

       vmax=-1.0e+30
       vmin=1.0e+30
       do j=1,nx
         do i=1,nx
           vtest=mask1(i,j)*v(i,j)
     mask2(i,j)=0.
           if (vtest .gt. vmax) vmax=vtest
           if (vtest .lt. vmin) vmin=vtest
         enddo
       enddo
       write(*,*) 'maximum velocity =',vmax,' minimum =',vmin

c**********************************************************************
c                                                                     *
c Remove velocity signal due to observer's motion.                    *
c                                                                     *
c**********************************************************************
       call vfix(nx,v,x0,y0,rsq,angles,c0,cx,cy)
       write(*,*) 'Data corrected for observers motion.'

       vmax=-1.0e+30
       vmin=1.0e+30
       do j=1,nx
         do i=1,nx
           vtest=mask1(i,j)*v(i,j)
```

```
          if (vtest .gt. vmax) vmax=vtest
          if (vtest .lt. vmin) vmin=vtest
        enddo
      enddo
      write(*,*) 'maximum velocity =',vmax,' minimum =',vmin

c**********************************************************************
c                                                                     *
c Initial guess at spectral coefficients.                             *
c                                                                     *
c**********************************************************************
      t(1) = 1598.
      t(2) = 10.2
      t(3) = -24.8
      t(4) =  0.0
      t(5) = -4.4
      s(1) =  0.0
      s(2) = 14.0
      s(3) = -4.0
      s(4) = -5.0
      s(5) = -1.0
      cls(1) = 380.
      cls(2) = 197.
      cls(3) = 90.
      cls(4) = 11.
      cls(5) = 2.6

c**********************************************************************
c                                                                     *
c Loop through determinations of spectral coefficients until they     *
c converge so that values used in masked out areas agree with the rest *
c of the data.                                                        *
c                                                                     *
c**********************************************************************
      do j = 1, nx
  do i = 1, nx
    vtemp(i,j) = v(i,j)
  enddo
      enddo

      do loop=1,1
  write(*,*) 'loop',loop

  do j = 1, nx
    do i = 1, nx
      v(i,j) = vtemp(i,j)
```

```
    enddo
  enddo

  do i=1,5
    c(i)=t(i)
    c(5+i)=s(i)
    c(10+i)=cls(i)
  enddo

c**************************************************************************
c                                                                         *
c Determine spectral coefficients for Limb Shift.                         *
c                                                                         *
c**************************************************************************
  call lshft(nx,v,mask1,x0,y0,rsq,angles,c,vls,cls)
  write(*,*) 'Preliminary Limb Shift analysis completed.'

c**************************************************************************
c                                                                         *
c Map data to heliographic coordinates.                                   *
c                                                                         *
c**************************************************************************
  call heliomap(nx,v,mask1,x0,y0,rsq,angles,vmap,mask2)
  write(*,*) 'Data mapped to heliographic coordinates.'

  vmax=-1.0e30
  vmin=1.0e30
  do j=1,nx
    do i=1,nx
      vtest=vmap(i,j)*mask2(i,j)
      if (vtest .gt. vmax) vmax=vtest
      if (vtest .lt. vmin) vmin=vtest
    enddo
  enddo
  write(*,*) 'maximum residual =',vmax,' minimum =',vmin

c**************************************************************************
c                                                                         *
c Determine spectral coefficients for Rotation.                           *
c                                                                         *
c**************************************************************************
  call rotation(nx,vmap,mask2,angles,c,vphi,t)
  write(*,*) 'Rotation analysis completed.'
  do l=1,15
    write(*,*) 't(',l,',0)=',t(l)
  enddo
```

```
  vmax=-1.0e30
  vmin=1.0e30
  do j=1,nx
    do i=1,nx
      vtest=vmap(i,j)*mask2(i,j)
      if (vtest .gt. vmax) vmax=vtest
      if (vtest .lt. vmin) vmin=vtest
    enddo
  enddo
  write(*,*) 'maximum residual =',vmax,' minimum =',vmin

c**********************************************************************
c                                                                     *
c Determine spectral coefficients for Meridional Circulation.       *
c                                                                     *
c**********************************************************************
  call mcirc(nx,vmap,mask2,angles,c,vtheta,s)
  write(*,*) 'Meridional Circulation analysis completed.'
  do l=1,15
    write(*,*) 's(',l,',0)=',s(l)
  enddo
  vmax=-1.0e30
  vmin=1.0e30
  do j=1,nx
    do i=1,nx
      vtest=vmap(i,j)*mask2(i,j)
      if (vtest .gt. vmax) vmax=vtest
      if (vtest .lt. vmin) vmin=vtest
    enddo
  enddo
  write(*,*) 'maximum residual =',vmax,' minimum =',vmin

c**********************************************************************
c                                                                     *
c Correct Limb Shift coefficients for presence of Meridional        *
c Circulation.                                                      *
c                                                                     *
c**********************************************************************
  call lshftc(nx,vmap,angles,s,vls,cls)
  write(*,*) 'Final Limb Shift analysis completed.'
  do n=1,6
    nm=n-1
    write(*,*) 'cls(',nm,')=',cls(n)
  enddo
  vmax=-1.0e30
  vmin=1.0e30
```

```
  do j=1,nx
    do i=1,nx
      vtest=vmap(i,j)*mask2(i,j)
      if (vtest .gt. vmax) vmax=vtest
      if (vtest .lt. vmin) vmin=vtest
    enddo
  enddo
  write(*,*) 'maximum residual =',vmax,' minimum =',vmin

      enddo


      do n=1,nx
        spcoef(n)=0.0
      enddo
      do n=1,15
        spcoef(n)=t(n)
      enddo
      do n=1,15
        spcoef(15+n)=s(n)
      enddo
      do n=1,6
        spcoef(30+n)=cls(n)
      enddo

c**********************************************************************
c                                                                     *
c Write spectral coefficients to disk.                                *
c                                                                     *
c**********************************************************************
      ext = '.txt1'
      write(*,*) 'Writing output coefficients to ',path,filename,ext
      open(unit=3,file=filename // ext,
     &  status='UNKNOWN',access='SEQUENTIAL',form='FORMATTED')
      do j=1,nx
        write(3,101) spcoef(j),vphi(j),vls(j)
      enddo
      close(3)
101   format(1x,e13.6,1x,e13.6,1x,e13.6)

      goto 10

9999  end
```

MDI_analysis2.for

```
      program mdi_analysis2
c**********************************************************************
c                                                                     *
c Analyzes Doppler velocity data to extract spectral coefficients     *
c and velocity profiles. Input files include velocity and             *
c intensity images and NSO magnetogram synoptic maps. Intensity is    *
c used to determine image parameters (center coordinates x0 and y0,   *
c radius, ellipticity, and orientation of elliptical figure for limb). *
c The magnetograms are used to produce a data mask which covers active *
c regions.                                                            *
c                                                                     *
c Output includes a formatted file containing spectral coefficients   *
c and a direct access file containing the individual spectral         *
c components for reconstructing the velocity image.                   *
c                                                                     *
c**********************************************************************

c     dtype=1: Real; dtype=0: Fake
c      parameter (nx=1024, lmaxp=1024, dtype=1)
      parameter (nx=1024, lmaxp=1024, dtype=0)

      complex*8 work1(2*nx),work2(lmaxp,nx)
      real*4 v(nx,nx),vmap(nx,nx),vtemp(nx,nx)
      real*4 vls(nx),vphi(nx),vtheta(nx),spcoef(nx)
      real*4 mask1(nx,nx),mask2(nx,nx)
      real*4 p(lmaxp),coef(lmaxp,lmaxp),spectrum(lmaxp,lmaxp)
      real*4 t(8),s(8),cls(5)
      real*4 pstar(5,nx)
      real*4 c(15),angles(6)
      character mday*4,mhour*4,magnum*4
      byte buffer(2880)
c      character path*16,filename*9,ext*5,hdr*2880,hdrrec*80
      character path*1,filename*4,ext*5,hdr*2880,hdrrec*80
c      path='_'
c      path='d:\soidata\fake\'

      pi=4.0*atan(1.0)
      pihalf=pi/2.
      dtheta=pi/nx
      dphi=pi/nx
      root3=sqrt(3.)
      root5=sqrt(5.)
      root7=sqrt(7.)
```

```
      datamask=-32768.


c**********************************************************************
c                                                                      *
c Calculate matrix of coefficients for Associated Legendre polynomials.*
c                                                                      *
c**********************************************************************
      call plmcoef(lmaxp,coef)
      write(*,*) 'Coefficients for Legendre polynomials calculated.'

c**********************************************************************
c                                                                      *
c  Fractional radius for limits of data analysis.                      *
c                                                                      *
c**********************************************************************
      sinrho = 0.99

c**********************************************************************
c                                                                      *
c  List of data files for analysis.                                    *
c                                                                      *
c**********************************************************************
      open(unit=7,name='analysis.inp',status='old')

10    continue
      read(7,1001,END=9999) filename
1001    format(a4)

c      if (dtype .eq. 1) then
c   mday=filename(1:4)
c   mhour=filename(6:9)
c   time = 1000.*(ichar(mday(1:1))-48.) - 1239. +
c     &    100.*(ichar(mday(2:2))-48.) +
c     &    10.*(ichar(mday(3:3))-48.) +
c     &    1.*(ichar(mday(4:4))-48.) +
c     &    (10.*(ichar(mhour(3:3))-48.)+1.*(ichar(mhour(4:4))-48.))/96.
c   write(*,*) 'Time in days = ',time
c        ext = '.fits'
c        write(*,*) 'Processing ',path,filename,ext
cc**********************************************************************
c                                                                      *
c Read in Doppler velocity array.                                      *
c                                                                      *
c**********************************************************************
```

```
c        open(unit=8,name='temp.txt',status='old')
c 1003   format(a19)
c 1004   format(g19.12)
c        open(unit=9,name=path // filename // ext,status='OLD',
c     &       access='direct',recl=720)
c*************************************************************************
c                                                                        *
c Read in header information.                                            *
c                                                                        *
c*************************************************************************
c        do nrec=1,5
c          read(9,rec=nrec) hdr
c          do i=1,36
c       hdrrec=hdr((i-1)*80+1:i*80)
c       rewind(8)
c       if (hdrrec(1:8) .eq. 'OBS_DIST') then
c         write(8,1003) hdrrec(12:30)
c         rewind(8)
c         read(8,1004) rdist_au
c       endif
c       if (hdrrec(1:6) .eq. 'OBS_B0') then
c         write(8,1003) hdrrec(12:30)
c         rewind(8)
c              read(8,1004) b0
c       endif
c       if (hdrrec(1:6) .eq. 'OBS_L0') then
c         write(8,1003) hdrrec(12:30)
c         rewind(8)
c              read(8,1004) clon
c       endif
c       if (hdrrec(1:6) .eq. 'OBS_VR') then
c         write(8,1003) hdrrec(12:30)
c         rewind(8)
c              read(8,1004) c0
c       endif
c       if (hdrrec(1:6) .eq. 'OBS_VN') then
c         write(8,1003) hdrrec(12:30)
c         rewind(8)
c              read(8,1004) cy
c       endif
c       if (hdrrec(1:6) .eq. 'OBS_VW') then
c         write(8,1003) hdrrec(12:30)
c         rewind(8)
c              read(8,1004) cx
c       endif
c       if (hdrrec(1:8) .eq. 'MAP_RSUN') then
```

```
c         write(8,1003) hdrrec(12:30)
c         rewind(8)
c              read(8,1004) radius
c       endif
c       if (hdrrec(1:6) .eq. 'MAP_X0') then
c         write(8,1003) hdrrec(12:30)
c         rewind(8)
c              read(8,1004) x0
c       endif
c       if (hdrrec(1:6) .eq. 'MAP_Y0') then
c         write(8,1003) hdrrec(12:30)
c         rewind(8)
c              read(8,1004) y0
c       endif
c       if (hdrrec(1:6) .eq. 'BSCALE') then
c         write(8,1003) hdrrec(12:30)
c         rewind(8)
c              read(8,1004) bscale
c       endif
c       if (hdrrec(1:5) .eq. 'BZERO') then
c         write(8,1003) hdrrec(12:30)
c         rewind(8)
c              read(8,1004) bzero
c       endif
c            if (hdrrec(1:3) .eq. 'END') goto 20
c          enddo
c        enddo
c 20     nskip=nrec
c        close(8)
c*************************************************************************
c                                                                        *
c Read in velocity array.                                                *
c                                                                        *
c*************************************************************************
c        vmax=-1.0e+30
c        vmin=1.0e+30
c*************************************************************************
c                                                                        *
c Integer data                                                           *
c                                                                        *
c*************************************************************************
c        nrec=int((1024.*1024.)/1440.)
c        do jrec=1,nrec
c      read(9,rec=nskip+jrec) (buffer(icol),icol=1,2880)
c     do k=1,1440
c       nelem=(jrec-1)*1440 + k
```

```
c       j=1+(nelem-1)/1024
c       i=nelem-(j-1)*1024
c       value=float(buffer(2*k)) + 256.*float(buffer(2*k-1))
c            if (buffer(2*k) .lt. 0) value=value+256.
c       v(i,j)=bzero+bscale*value
c            if(v(i,j) .gt. vmax) vmax=v(i,j)
c            if(v(i,j) .lt. vmin) vmin=v(i,j)
c     enddo
c        enddo
c        close(9)
c   s0 = 959.65/rdist_au
c        cy = -cy*sin(s0*pi/(180.*3600.))
c        cx = -cx*sin(s0*pi/(180.*3600.))
c   datamask = -32768.*bscale + bzero
c*********************************************************************
c                                                                    *
c Real*4 data                                                        *
c                                                                    *
c*********************************************************************
c      nrec=int((1024.*1024.)/720.)
c      do jrec=1,nrec
c  read(9,rec=nskip+jrec) (rbuffer(icol),icol=1,720)
c do k=1,720
c   nelem=(jrec-1)*720 + k
c   j=1+(nelem-1)/1024
c   i=nelem-(j-1)*1024
c   v(i,j)=rbuffer(k)
c          if(v(i,j) .gt. vmax) vmax=v(i,j)
c          if(v(i,j) .lt. vmin) vmin=v(i,j)
c enddo
c      enddo
c      close(9)
c*********************************************************************
c                                                                    *
c Extrapolate c0, cx, and cy from data prior to day 1285.            *
c                                                                    *
c*********************************************************************
c        if (time .ge. 1285.-1239.) then
c          c0=242.36-2.607*time-0.03365*time*time
c     cx=-135.028+0.03374*time-0.0002366*time*time
c     cy=-16.6418-0.06437*time+0.002330*time*time
c   endif
c*********************************************************************
c                                                                    *
c Correct (x0,y0) for FORTRAN counting system ((1.,1.) at lower left). *
c                                                                    *
```

```
c*************************************************************************
c   x0 = x0 + 1.0
c   y0 = y0 + 1.0
c   rsq=radius*radius
c*************************************************************************
c                                                                        *
c  Correct velocity signal for center-to-limb line variation.            *
c                                                                        *
c*************************************************************************
c        jmin0=int(y0+1.-radius)
c        jmax0=int(y0+radius)
c        do j=jmin0,jmax0
c          yp=(j-0.5)-y0
c          hchord=sqrt(rsq-yp*yp)
c          imin=int(x0+1.0-hchord)
c          imax=int(x0+hchord)
c          do i=imin,imax
c            xp=(i-0.5)-x0
c            rp=xp*xp+yp*yp
c            r2=rp/rsq
c       x=sqrt(r2)
c       v(i,j)=(1.00+0.10*x*x*x)*v(i,j)
c     enddo
c   enddo
c*************************************************************************
c                                                                         *
c Average spectral coefficients from analysis1.                           *
c                                                                         *
c*************************************************************************
c        t(1) = 1598.41-0.3140*time
c        t(2) =   11.39-0.0983*time
c        t(3) =  -24.48-0.0042*time
c        t(4) =   -0.81+0.0005*time
c        t(5) =   -4.20-0.0012*time
c   t(6) =   -0.37-0.0067*time
c   t(7) =   -1.05-0.0052*time
c   t(8) =   -0.09+0.0044*time

c        s(1) =   21.74-0.1850*time
c        s(2) =   13.85-0.1060*time
c        s(3) =   -4.09+0.0515*time
c        s(4) =   -5.32+0.0898*time
c        s(5) =   -0.77-0.0225*time
c   s(6) =    0.22-0.0258*time
c   s(7) =   -0.34+0.0030*time
c   s(8) =   -0.93+0.0107*time
```

```
c        cls(1) = 379.50-4.571*time
c        cls(2) = 196.50-0.278*time
c        cls(3) =  90.05+0.027*time
c        cls(4) =  11.41+0.057*time
c        cls(5) =   2.59-0.014*time

c endif
c*************************************************************************
c                                                                        *
c fakedata                                                               *
c                                                                        *
c*************************************************************************
if (dtype .eq. 0) then
  ext='.data'
c   b0=-1.62895
  b0=0.0
  s0=959.65/1.0019
        c0=0.0
        c2=0.0
        cx=0.0
        cy=0.0
        radius=502.0
        rsq=radius*radius
        x0=512.5
        y0=512.5
        ellips=1.0
        eangle=0.0
        pangle=0.0
        open(unit=3,file= filename // ext,status='OLD',
     &    access='direct',recl=4*nx)
        vmax=-1.0e+30
        vmin=1.0e+30
        do j=1,nx
          read(3,rec=j) (v(i,j),i=1,nx)
          do i=1,nx
            if(v(i,j) .gt. vmax) vmax=v(i,j)
            if(v(i,j) .lt. vmin) vmin=v(i,j)
          enddo
        enddo
        close(3)
c*************************************************************************
c                                                                        *
c Spectral coefficients from analysis1.                          *
c                                                                        *
c*************************************************************************
```

```
c*********************************************************************
c                                                                     *
c Read spectral coefficients from disk.                               *
c                                                                     *
c*********************************************************************
        ext = '.txt1'
        write(*,*) 'Reading output coefficients from ',path,filename,ext
        open(unit=3,file= filename // ext,
     &    status='OLD',access='SEQUENTIAL',form='FORMATTED')
          do j=1,8
       read(3,101) const1,const2,const3
       t(j)=const1
          enddo
          do j=1,7
       read(3,101) const1,const2,const3
          enddo
          do j=1,8
       read(3,101) const1,const2,const3
       s(j)=const1
          enddo
          do j=1,7
       read(3,101) const1,const2,const3
          enddo
          do j=1,5
       read(3,101) const1,const2,const3
       cls(j)=const1
          enddo
        close(3)
endif

       sins0=sin(s0*pi/(180.*3600.))
       ellips=1.0
       eangle=0.0
       pangle=0.0

       angles(1)=s0
       angles(2)=b0
       angles(3)=pangle
       angles(4)=eangle
       angles(5)=ellips
       angles(6)=sinrho

       write(*,*) 'Semi-diameter, s0, in arc-seconds, is ',s0
       write(*,*) 'Rotation axis tilt, b0, in degrees, is ',b0
       write(*,*) '************ observer motion *************'
       write(*,*) '             c0=',c0
```

```
      write(*,*) '             cx=',cx
      write(*,*) '             cy=',cy


      fov=nx*s0/radius
      write(*,*) '************ image parameters *************'
      write(*,*) '                x0=',x0
      write(*,*) '                y0=',y0
      write(*,*) '            radius=',radius
      write(*,*) '            pangle=',pangle
      write(*,*) '            ellips=',ellips
      write(*,*) '            eangle=',eangle
      write(*,*) 'Velocity max and min = ',vmax,vmin

      if (v(512-400,512) .gt. v(512+400,512)) then
        do j=1,nx
          do i=1,nx
            v(i,j)=-1.*v(i,j)
          enddo
        enddo
      endif

c**********************************************************************
c                                                                     *
c Construct initial data mask.                                        *
c                                                                     *
c**********************************************************************
total=0
do j=1,nx
  y=(j-0.5)-y0
  do i=1,nx
    x=(i-0.5)-x0
    mask1(i,j)=1.
    r2=x*x+y*y
    if (r2 .gt. sinrho*sinrho*rsq) mask1(i,j)=0.
    if (v(i,j) .eq. datamask) mask1(i,j)=0.
    total=total+mask1(i,j)
    mask2(i,j)=mask1(i,j)
  enddo
enddo
write(*,*) 'Total unmasked pixels = ',total

c**********************************************************************
c                                                                     *
c  Produce active region mask from magnetograms.                      *
c                                                                     *
```

```
c**********************************************************************
c      if (mhour .eq. '00') magnum='0000'
c      if (mhour .eq. '01') magnum='0001'
c      if (mhour .eq. '02') magnum='0001'
c      if (mhour .eq. '03') magnum='0002'
c      if (mhour .eq. '04') magnum='0002'
c      if (mhour .eq. '05') magnum='0003'
c      if (mhour .eq. '06') magnum='0004'
c      if (mhour .eq. '07') magnum='0004'
c      if (mhour .eq. '08') magnum='0005'
c      if (mhour .eq. '09') magnum='0006'
c      if (mhour .eq. '10') magnum='0006'
c      if (mhour .eq. '11') magnum='0007'
c      if (mhour .eq. '12') magnum='0008'
c      if (mhour .eq. '13') magnum='0008'
c      if (mhour .eq. '14') magnum='0009'
c      if (mhour .eq. '15') magnum='0009'
c      if (mhour .eq. '16') magnum='0010'
c      if (mhour .eq. '17') magnum='0011'
c      if (mhour .eq. '18') magnum='0011'
c      if (mhour .eq. '19') magnum='0012'
c      if (mhour .eq. '20') magnum='0012'
c      if (mhour .eq. '21') magnum='0013'
c      if (mhour .eq. '22') magnum='0014'
c      if (mhour .eq. '23') magnum='0014'
c
c      call mdi_mag(nx,mday,magnum,bimage)
c
c      bmask=50.
c      call magmask(nx,bmask,bimage,mask2)
c
c      call moremask(nx,mask2)

      do j=1,nx
        do i=1,nx
          mask1(i,j)= mask1(i,j)*mask2(i,j)
        enddo
      enddo

      write(*,*) 'Data masks constructed.'

      vmax=-1.0e+30
      vmin=1.0e+30
      do j=1,nx
        do i=1,nx
          vtest=mask1(i,j)*v(i,j)
```

```
          mask2(i,j)=0.
          if (vtest .gt. vmax) vmax=vtest
          if (vtest .lt. vmin) vmin=vtest
        enddo
      enddo
      write(*,*) 'maximum velocity =',vmax,' minimum =',vmin

c*********************************************************************
c                                                                     *
c Remove velocity signal due to observer's motion.                    *
c                                                                     *
c*********************************************************************
      call vfix(nx,v,x0,y0,rsq,angles,c0,cx,cy)
      write(*,*) 'Data corrected for observers motion.'

      vmax=-1.0e+30
      vmin=1.0e+30
      do j=1,nx
        do i=1,nx
          vtest=mask1(i,j)*v(i,j)
          if (vtest .gt. vmax) vmax=vtest
          if (vtest .lt. vmin) vmin=vtest
        enddo
      enddo
      write(*,*) 'maximum velocity =',vmax,' minimum =',vmin

c*********************************************************************
c                                                                     *
c Remove convective blue shift
c                                                                     *
c*********************************************************************
cosea=cos(eangle*pi/180.)
sinea=sin(eangle*pi/180.)
dxx=1./(nx-1.)
jmin0=y0+1.-radius
jmax0=y0+radius
do k=1,nx
  xx=(k-1.)*dxx
  pstar(1,k)=1.
  pstar(2,k)=root3*(2.*xx-1.)
  pstar(3,k)=root5*(6.*xx**2-6.*xx+1.)
  pstar(4,k)=root7*(20.*xx**3-30.*xx**2+12.*xx-1.)
  pstar(5,k)=3.*(70.*xx**4-140.*xx**3+90.*xx**2.-20.*xx+1.)
enddo
do j=jmin0,jmax0
  hchord=sqrt(rsq-(j-0.5-y0)*(j-0.5-y0))
```

```
  imin=x0+1.0-hchord
  imax=x0+hchord
  do i=imin,imax
    x=(i-0.5-x0)*cosea+(j-0.5-y0)*sinea
    y=((j-0.5-y0)*cosea-(i-0.5-x0)*sinea)/ellips
    xx=(x*x+y*y)/rsq
    if(xx .le. 1.)then
      xvar=1.-sqrt(1.-xx)
      k=1.5+xvar*(nx-1.)
      do n=1,5
        v(i,j)=v(i,j)-cls(n)*pstar(n,k)
      enddo
    endif
  enddo
enddo
write(*,*) 'Convective Blue Shift removed.'

c**********************************************************************
c                                                                     *
c Map data to heliographic coordinates.                               *
c                                                                     *
c**********************************************************************
call heliomap(nx,v,mask1,x0,y0,rsq,angles,vmap,mask2)
write(*,*) 'Data mapped to heliographic coordinates.'

vmax=-1.0e30
vmin=1.0e30
do j=1,nx
  do i=1,nx
    vtest=vmap(i,j)*mask2(i,j)
    if (vtest .gt. vmax) vmax=vtest
    if (vtest .lt. vmin) vmin=vtest
  enddo
enddo
write(*,*) 'maximum residual =',vmax,' minimum =',vmin

c**********************************************************************
c                                                                     *
c Remove Rotation and meridional circulation signals
c                                                                     *
c**********************************************************************
      cosrho=sqrt(1.-sinrho*sinrho)
      sr=s0*pi/(180.*3600.)
      cosb0=cos(b0*pi/180.)
      sinb0=sin(b0*pi/180.)
      rho=asin(sinrho)
```

```
      bmax=b0*pi/180.+rho
      if (bmax .gt. pi/2.) bmax=pi/2.
      bmin=b0*pi/180.-rho
      if (bmin .lt. -pi/2.) bmin=-pi/2.
      jmin=nx*((pi/2.+bmin)/pi)+1
      jmax=nx*((pi/2.+bmax)/pi)
      jmin=nx*((pihalf+bmin)/pi)+1
      jmax=nx*((pihalf+bmax)/pi)

do j=jmin,jmax
  theta=pi-(j-0.5)*dtheta
  sinb=cos(theta)
  cosb=sin(theta)
  cosphi=(cosrho-sinb0*sinb)/(cosb*cosb0)
        if (cosphi .lt. 0.) cosphi=0.0
        if (cosphi .gt. 1.) cosphi=1.0
  phimax=acos(cosphi)
  i1=nint(nx/2.+0.5-nx*phimax/pi)
  i2=nint(nx/2.+0.5+nx*phimax/pi)
  call plm16(1,sinb,p)
  utemp1=0.
  utemp2=0.
  do l=1,8
    utemp1=utemp1+t(l)*sqrt(l*(l+1.))*p(l+1)
    utemp2=utemp2-s(l)*sqrt(l*(l+1.))*p(l+1)
  enddo
  do i=i1,i2
    phi=(i-0.5)*dphi-pihalf
    vmap(i,j)=vmap(i,j)-utemp1*cosb0*sin(phi)
    vmap(i,j)=vmap(i,j)-utemp2*(sinb0*cosb-cosb0*sinb*cos(phi))
  enddo
enddo

vmax=-1.0e30
vmin=1.0e30
do j=1,nx
  do i=1,nx
    vtest=vmap(i,j)*mask2(i,j)
    if (vtest .gt. vmax) vmax=vtest
    if (vtest .lt. vmin) vmin=vtest
  enddo
enddo
write(*,*) 'maximum residual =',vmax,' minimum =',vmin

c**********************************************************************
c                                                                     *
```

```
c Smooth mask edges prior to Legendre transform.                      *
c                                                                     *
c*********************************************************************
      call smthmask(nx,mask2,mask1)
      write(*,*) 'Data mask smoothed for Legendre transform.'

c*********************************************************************
c                                                                     *
c Determine spectral coefficients for non-axisymmetric components up  *
c to maximum degree l=lmaxp-1.                                        *
c                                                                     *
c*********************************************************************
      call plmxform(nx,vmap,mask2,lmaxp,p,coef,angles,work1,work2,
     &              spectrum)
      write(*,*) 'Legendre transform completed.'

c*********************************************************************
c                                                                     *
c Write spectral coefficients to disk.                                *
c                                                                     *
c*********************************************************************
      ext = '.spec'
      write(*,*) 'Writing spectrum to ',path,filename,ext
      open(unit=2,file= filename // ext,
     &  status='unknown',access='direct',recl=4*lmaxp)
      do j=1,lmaxp
        write(2,rec=j) (spectrum(i,j),i=1,lmaxp)
      enddo
      close(2)
c*********************************************************************
c                                                                     *
c Write spectral coefficients to disk.                                *
c                                                                     *
c*********************************************************************
      ext = '.txt1'
      write(*,*) 'Reading output coefficients from ',path,filename,ext
      open(unit=3,file= filename // ext,
     &  status='OLD',access='SEQUENTIAL',form='FORMATTED')
      do j=1,nx
        read(3,101) spcoef(j),vphi(j),vls(j)
      enddo
      close(3)

      do l=0,nx-22
        spcoef(l+22)=0.
        do m=0,l
```

```
          spcoef(l+22)=spcoef(l+22)+spectrum(l+1,m+1)*spectrum(l+1,m+1)
        enddo
      enddo

      ext = '.text'
      write(*,*) 'Writing output coefficients to ',path,filename,ext
      open(unit=3,file= filename // ext,
     &  status='UNKNOWN',access='SEQUENTIAL',form='FORMATTED')
      do j=1,nx
        write(3,101) spcoef(j),vphi(j),vls(j)
      enddo
      close(3)
101   format(1x,e13.6,1x,e13.6,1x,e13.6)

      goto 10

9999  end
```

APPENDIX C

PROJECT FLOWCHARTS

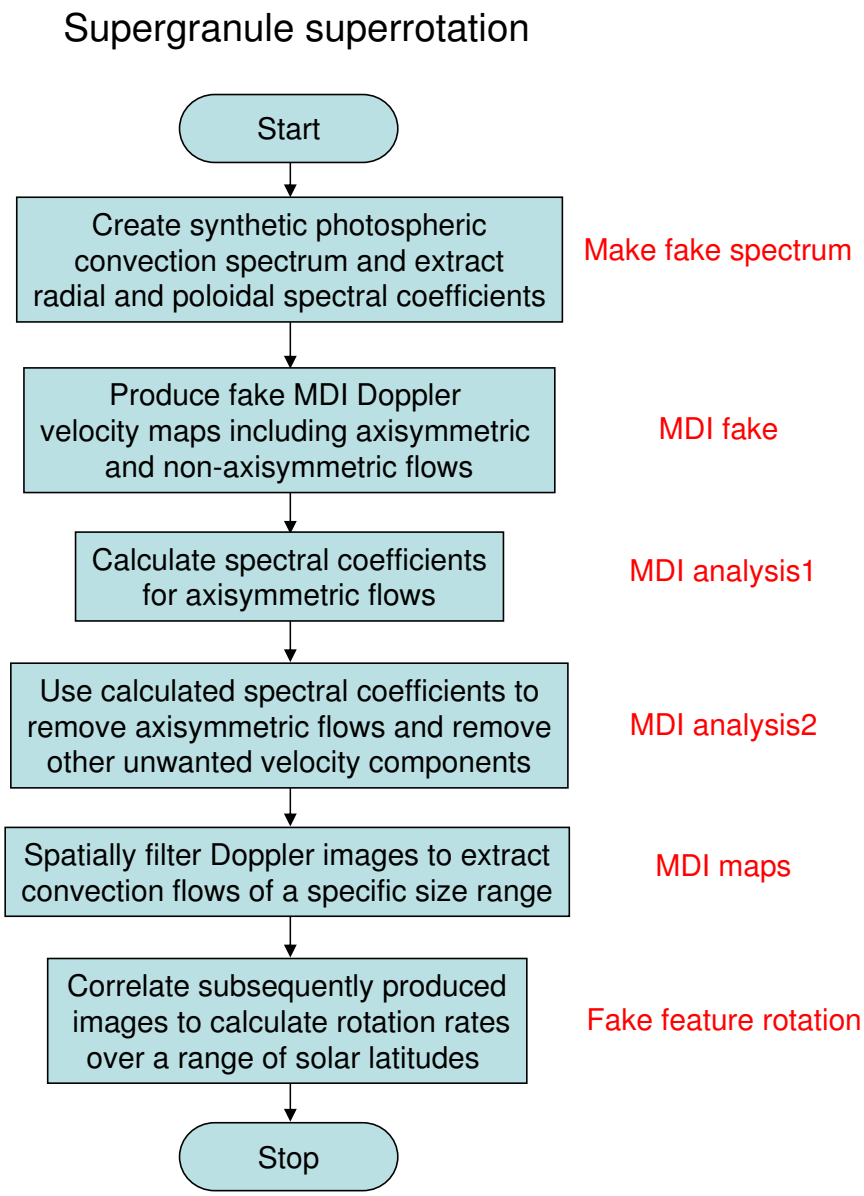
Supergranule superrotation
Start
Create synthetic photospheric convection spectrum and extract radial and poloidal spectral coefficients
Make fake spectrum
Produce fake MDI Doppler velocity maps including axisymmetric and non-axisymmetric flows
MDI fake
Calculate spectral coefficients for axisymmetric flows
MDI analysis1
Use calculated spectral coefficients to remove axisymmetric flows and remove other unwanted velocity components
MDI analysis2
Spatially filter Doppler images to extract convection flows of a specific size range
MDI maps
Correlate subsequently produced images to calculate rotation rates over a range of solar latitudes
Fake feature rotation
Stop

Rossby Hills Identified as Supergranules

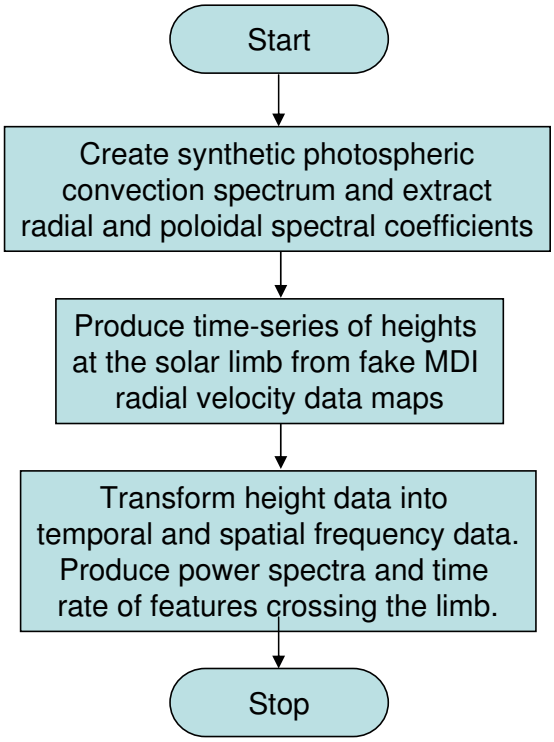

REFERENCES

[1] R. Kippenhahn and A. Weigert, *Stellar Structure and Evolution.* Berlin, Germany: Springer-Verlag, 1990.

[2] D. N. C. Lin, "The Nebular Origin of the Solar System," in *The Solar System: Observation and Interpretations*, M. G. Kivelson, ED. New Jersey, USA: Prentice-Hall, 1986, pp. 29–77.

[3] M. Zelik and P. Smith, *Introductory Astronomy and Astrophysics.* Philadelphia, USA: Saunders College Publishing, 1987.

[4] E. Böhm-Vitense, *Introduction to Stellar Astrophysics, Volume 3: Stellar Structure and Evolution.* Cambridge, UK: Cambridge University Press, 1992.

[5] M. Schwarzschild, *Structure and Evolution of the Stars.* Cambridge, UK: Cambridge University Press, 1958.

[6] G. O. Abell, D. Morrison, and S. C. Wolff, *Realm of the Universe (Fifth Edition).* Philadelphia, USA: Saunders College Publishing, 1994.

[7] (2007, June) Eso Press Releases - Hertzsprung-Russell diagram. [Online]. Available: http://www.eso.org/public/outreach/press-rel/pr-2007/phot-28-07.html

[8] I. J. Sackmann, A. I. Boothroyd, and K. E. Kraemer, "Our Sun. III. Present and Future," *Astrophysical Journal*, vol. 418, pp. 457–468, 1993.

[9] K. P. Schröder and R. C. Smith, "Distant Future of the Sun and Earth Revisited," *Monthly Notices of the Royal Astronomical Society*, vol. 386, pp. 155–163, 2008.

[10] R. Bowers and T. Deeming, *Astrophysics, I: Stars.* London, UK: Jones and Bartlett, 1984.

[11] B. W. Carroll and D. A. Ostlie, *An Introduction to Modern Astrophysics.* London, UK: Pearson Addison-Wesley, 1995.

[12] H. Habold and A. M. Mathai. (1997) Internal structure of the Sun. [Online]. Available: http://www.columbia.edu/ ah297/unesa/sun/sun-chapter1.html

[13] C. J. Hansen and S. D. Kawaler, *Stellar Interiors*. Berlin, Germany: Springer-Verlag, 1994.

[14] J. Schou, H. M. Antia, S. Basu, R. S. Bogart, R. I. Bush, S. M. Chitre, J. Christensen-Dalsgaard, M. P. di Mauro, W. A. Dziembowski, A. Eff-Darwich, D. O. Gough, D. A. Haber, J. T. Hoeksema, R. Howe, S. G. Korzennik, A. G. Kosovichev, R. M. Larsen, F. P. Pijpers, P. H. Scherrer, T. Sekii, T. D. Tarbell, A. M. Title, M. J. Thompson, and J. Toomre, "Helioseismic Studies of Differential Rotation in the Solar Envelope by the Solar Oscillations Investigation Using the Michelson Doppler Imager," *Astrophysical Journal*, vol. 505, pp. 390–417, 1998.

[15] M. Stix, *The Sun*. Berlin, Germany: Springer, 2002.

[16] H. W. Babcock and H. D. Babcock, "The Sun's Magnetic Field," *Astrophysical Journal*, vol. 121, pp. 349–366, 1955.

[17] H. D. Babcock, "The Sun's Polar Magnetic Field," *Astrophysical Journal*, vol. 130, pp. 364–380, 1959.

[18] R. Howard, "Studies of Solar Magnetic Fields - I. The Average Field Strengths," *Solar Physics*, vol. 38, pp. 283–299, 1974.

[19] E. N. Parker, "The Formation of Sunspots from the Solar Toroidal Field," *Astrophysical Journal*, vol. 121, pp. 491–507, 1955.

[20] ——, "Hydromagnetic Dynamo Models," *Astrophysical Journal*, vol. 122, pp. 293–314, 1955.

[21] M. Dikpati, G. de Toma, P. A. Gilman, C. N. Arge, and O. R. White, "Diagnostics of Polar Field Reversal in Solar Cycle 23 Using a Flux Transport Dynamo Model," *Astrophysical Journal*, vol. 601, pp. 1136–1151, 2004.

[22] M. Dikpati and P. A. Gilman, "Simulating and Predicting Solar Cycles Using a Flux-Transport Dynamo," *Astrophysical Journal*, vol. 649, pp. 498–514, 2006.

[23] A. R. Choudhuri, P. Chatterjee, and J. Jiang, "Predicting Solar Cycle 24 with a Solar Dynamo Model," *Physical Review Letters*, vol. 98, p. 131103, 2007.

[24] D. H. Hathaway and M. Adams. (2007, Jan.) Chromospheric features of the Sun. [Online]. Available: http://solarscience.msfc.nasa.gov/feature2.shtml

[25] B. E. Goldstein, "The Solar Wind," in *From the Sun*, S. T. Suess and B. T. Tsurutani, EDS. Washington DC, USA: Amercian Geophysical Union, 1998, pp. 73–80.

[26] W. I. Axford and S. T. Suess, "The Outer Heliosphere," in *From the Sun*, S. T. Suess and B. T. Tsurutani, EDS. Washington DC, USA: Amercian Geophysical Union, 1998, pp. 143–152.

[27] S. I. H. Cowley, "The Earth's Magnetosphere," in *From the Sun*, S. T. Suess and B. T. Tsurutani, EDS. Washington DC, USA: Amercian Geophysical Union, 1998, pp. 13–22.

[28] S.-I. Akasofu, "Aurora," in *From the Sun*, S. T. Suess and B. T. Tsurutani, EDS. Washington DC, USA: Amercian Geophysical Union, 1998, pp. 1–12.

[29] H. Zirin, *Astrophysics of the Sun*. Cambridge, UK: Cambridge University Press, 1988.

[30] M. Schwarzschild, "Photographs of the Solar Granulation Taken from the Stratosphere," *Astrophysical Journal*, vol. 130, pp. 345–363, 1959.

[31] R. F. Stein and A. Nordlund, "Simulations of Solar Granulation. I. General Properties," *Astrophysical Journal*, vol. 499, pp. 914–933, 1998.

[32] ——, "Realistic Solar Convection Simulations," *Solar Physics*, vol. 192, pp. 91–108, 2000.

[33] L. J. November, J. Toomre, K. B. Gebbie, and G. W. Simon, "The Detection of Mesogranulation on the Sun," *Astrophysical Journal*, vol. 245, pp. L123–L126, 1981.

[34] M. Rieutord, T. Roudier, J. M. Malherbe, and F. Rincon, "On Mesogranulation, Network Formation and Supergranulation," *Astronomy and Astrophysics*, vol. 357, pp. 1063–1072, 2000.

[35] D. H. Hathaway, J. G. Beck, R. S. Bogart, K. T. Bachmann, G. Khatari, J. M. Petitto, S. Han, and J. Raymond, "The Photospheric Convection Spectrum," *Solar Physics*, vol. 193, pp. 299–312, 2000.

[36] R. B. Leighton, R. W. Noyes, and G. W. Simon, "Velocity Fields in the Solar Atmosphere. I. Preliminary Report," *Astrophysical Journal*, vol. 135, pp. 474–499, 1962.

[37] J. Lisle, M. DeRosa, and J. Toomre, "New Approach to Study Extended Evolution of Supergranular Flows and Their Advection of Magnetic Elements," *Solar Physics*, vol. 197, pp. 21–30, 2000.

[38] M. P. Rast, "Supergranulation: New Observation and Possible Explanation," in *Local and Global Helioseismology: The Present and Future*, Big Bear Lake, California, USA, Oct. 2002, pp. 163–172.

[39] G. W. Simon and N. O. Weiss, "Supergranules and the Hydrogen Convection Zone," *Zeitschrift für Astrophysik*, vol. 69, pp. 435–450, 1968.

[40] J. G. Beck and T. L. D.-J. and P. H. Scherrer, "Long-lived Giant Cells Detected at the Surface of the Sun," *Nature*, vol. 394, pp. 653–655, 1998.

[41] H. Schwan and H. Wöhl, "On Possible Giant Cell Circulations of the Solar Ca^{+}-Network," *Astronomy and Astrophysics*, vol. 70, pp. 297–302, 1978.

[42] G. Küveler, "Velocity Fields of Individual Supergranules," *Solar Physics*, vol. 88, pp. 13–29, 1978.

[43] A. Kubicela, "Some Details of the Supergranular Motion," in *Solar Activity and Related Interplanetary and Terrestrial Phenomena*, J. Xanthakis, ED. Berlin, Germany: Springer-Verlag, 1973, pp. 123–130.

[44] D. H. Hathaway, "Nonlinear Simulations of Solar Rotation Effects in Supergranules," *Solar Physics*, vol. 77, pp. 341–356, 1982.

[45] ——, "The Solar Dynamo," in *From the Sun*, S. T. Suess and B. T. Tsurutani, EDS. Washington DC, USA: Amercian Geophysical Union, 1998, pp. 113–122.

[46] D. J. Galloway and M. R. E. Proctor, "The Kinematics of Hexagonal Magneto-convection," *Geophysical and Astrophysical Fluid Dynamics*, vol. 24, pp. 109–136, 1983.

[47] R. J. Defouw, "Wave Propagation Along a Magnetic Tube," *Astrophysical Journal*, vol. 209, pp. 266–269, 1976.

[48] S. Routh, Z. E. Musielak, and R. Hammer, "Conditions for Propagation of Torsional Waves in Solar Magnetic Flux Tubes," *Solar Physics*, vol. 246, pp. 133–143, 2007.

[49] F. Cattaneo, "On the Origin of Magnetic Fields in the Quiet Photosphere," *Astrophysical Journal*, vol. 515, pp. L39–L42, 1999.

[50] A. D. Gilbert, "Fast Dynamo Action in a Steady Chaotic Flow," *Nature*, vol. 350, pp. 483–485, 1991.

[51] R. F. Stein, private communication, 2008.

[52] H. D. Köhler, "The Solar Dynamo and Estimate of the Magnetic Diffusivity and the Alpha-effect," *Astronomy and Astrohphysics*, vol. 25, pp. 467–476, 1973.

[53] T. L. Duvall-Jr, "The Equatorial Rotation Rate Of Supergranulation Cells," *Solar Physics*, vol. 66, pp. 213–221, 1980.

[54] E. Nesme-Ribes, E. N. Ferriera, and P. Mein, "Solar Dynamics Over Solar Cycle 21 Using Sunspots as Tracers. I. Sunspot Rotation," *Astronomy and Astrohphysics*, vol. 274, pp. 563–570, 1973.

[55] J. G. Beck, T. L. Duvall-Jr, and J. Schou, "Wave-like Properties of Solar Supergranulation," *Nature*, vol. 421, pp. 43–45, 2003.

[56] S. Sofia, W. Heaps, and L. W. Twigg, "The Solar Diameter and Oblateness Measured by the Solar Disk Sextant on the 1992 September 30 Balloon Flight," *Astrophysical Journal*, vol. 427, pp. 1048–1052, 1994.

[57] J. R. Kuhn, R. I. Bush, X. Scheick, and P. H. Scherrer, "The Sun's Shape and Brightness," *Nature*, vol. 392, pp. 155–157, 1998.

[58] J. R. Kuhn, J. D. Armstrong, R. I. Bush, and P. H. Scherrer, "Rossby Waves on the Sun as Revealed by Solar 'Hills'," *Nature*, vol. 405, pp. 544–546, 2000.

[59] J. Schou, "Wavelike Properties of Solar Supergranulation Detected in Doppler Shift Data," *Astrophysical Journal Letters*, vol. 193, pp. L259–L262, 2003.

[60] E. Fossat, G. Grec, and M. Pomerantz, "Solar Pulsations Observed From the Geographic South Pole - Initial Results," *Solar Physics*, vol. 74, pp. 53–69, 1981.

[61] P. F. Moretti and G. Severino, "CASTEL: Capodimonte Antarctic Solar TELescope," *Memorie della Societa Astronomica Italiana Supplement*, vol. 2, pp. 186–189, 2003.

[62] J. W. Harvey, F. Hill, R. P. Hubbard, J. R. Kennedy, J. W. Leibacher, J. A. Pintar, P. A. Gilman, R. W. Noyes, A. M. Title, J. Toomre, R. K. Ulrich, A. Bhatnagar, J. A. Kennewell, W. Marquette, J. Patron, O. Saa, and E. Yasukawa, "The Global Oscillation Network Group (GONG) Project," *Science*, vol. 272, pp. 1284–1286, 1996.

[63] F. Hill, P. B. Stark, R. T. Stebbins, E. R. Anderson, H. M. Antia, T. M. Brown, T. L. Duvall-Jr, D. A. Haber, J. W. Harvey, D. H. Hathaway, R. Howe, R. P. Hubbard, H. P. Jones, J. R. Kennedy, S. G. Korzennik, A. G. Kosovichev, J. W. Leibacher, K. G. Libbrecht, J. A. Pintar, E. J. R.-J. and J. Schou, M. J. Thompson, S. Tomczyk, C. G. Toner, R. Toussaint, and W. E. Williams, "The Solar Acoustic Spectrum and Eigenmode Parameters," *Science*, vol. 272, pp. 1292–1295, 1996.

[64] D. O. Gough, A. G. Kosovichev, J. Toomre, E. Anderson, H. M. Antia, S. Basu, B. Chaboyer, S. M. Chitre, J. Christensen-Dalsgaard, W. A. Dziembowski, A. Eff-Darwich, J. R. Elliott, P. M. Giles, P. R. Goode, J. A. Guzik, J. W. Harvey, F. Hill, J. W. Leibacher, M. J. P. F. G. Monteiro, O. Richard, T. Sekii, H. Shibahashi, M. Takata, M. J. Thompson, S. Vauclair, and S. V. Vorontsov, "The Seismic Structure of the Sun," *Science*, vol. 272, pp. 1296–1300, 1996.

[65] M. J. Thompson, J. Toomre, E. R. Anderson, H. M. Antia, G. Berthomieu, D. Burtonclay, S. M. Chitre, J. Christensen-Dalsgaard, T. Corbard, M. DeRosa, C. R. Genovese, D. O. Gough, D. A. Haber, J. W. Harvey, F. Hill, R. Howe, S. G. Korzennik, A. G. Kosovichev, J. W. Leibacher, F. P. Pijpers, J. Provost, E. J. Rhodes-

Jr, J. Schou, T. Sekii, P. B. Stark, and P. R. Wilson, "Differential Rotation and Dynamics of the Solar Interior," *Science*, vol. 272, pp. 1300–1305, 1996.

[66] D. H. Hathaway, P. A. Gilman, J. W. Harvey, F. Hill, R. F. Howard, H. P. Jones, J. C. Kasher, J. W. Leibacher, J. A. Pintar, and G. W. Simon, "GONG Observations of Solar Surface Flows," *Science*, vol. 272, pp. 1306–1309, 1996.

[67] V. D. B. Fleck and A. I. Poland, "The SOHO Mission: an Overview," *Solar Physics*, vol. 162, pp. 1–37, 1995.

[68] P. H. Scherrer, R. S. Bogart, R. I. Bush, J. T. Hoeksema, A. G. Kosovichev, J. Schou, W. Rosenberg, L. Springer, T. D. Tarbell, A. M. Title, C. J. Wolfson, and I. Zayer, "The Solar Oscillations Investigation - Michelson Doppler Imager," *Solar Physics*, vol. 162, pp. 129–188, 1995.

[69] L. Delbouille, G. Roland, and L. Neven, *Atlas photometrique DU spectre solaire de λ=3000 a λ=10000.* Institut d'Astrophysique, Liege, Belgium: Universite de Liege, 1973.

[70] J. Bland-Hawthorn, "Tunable Imaging Filters," in *Encyclopedia of Astronomy and Astrophysics, Vol. III*, P. Murdin, ED. Bristol, UK: Institute of Physics Publishing, 2000, pp. 3360–3367.

[71] A. M. Title and H. E. Ramsey, "Improvements in Birefringent Filters: Analog Birefringent Elements," *Applied Optics*, vol. 19, pp. 2046–2058, 1980.

[72] G. Grec. (2001, Aug.) Short introduction to Astroseismology. [Online]. Available: http://www.oca.eu/grec/astrosismologie.html

[73] D. H. Hathaway, "Doppler Measurements of the Sun's Meridional Flow," *Astrophysical Journal*, vol. 460, pp. 1027–1033, 1996.

[74] J. M. Beckers and G. D. Nelson, "Some Comments on the Limb Shift of Solar Lines. II: The Effect of Granular Motions," *Solar Physics*, vol. 58, pp. 243–261, 1978.

[75] J. C. Lopresto, R. D. Chapman, and E. A. Sturgis, "Solar Gravitational Redshift," *Solar Physics*, vol. 66, pp. 245–249, 1979.

[76] D. H. Hathaway, "Spherical Harmonic Analysis of Steady Photospheric Flows, II," *Solar Physics*, vol. 137, pp. 15–32, 1992.

[77] ——, "Temporal Filters For Isolating Steady Photospheric Flows," *Solar Physics*, vol. 117, pp. 1–12, 1988.

[78] H. Balthasar, D. Stark, and H. Woehl, "The Solar Rotation Elements i and Omega Derived From Recurrent Single Sunspots," *Astronomy and Astrophysics*, vol. 174, pp. 359–360, 1987.

[79] D. H. Hathaway, "Simulating Photospheric Doppler Velocity Fields," *Solar Physics*, vol. 117, pp. 329–341, 1988.

[80] R. C. Carrington, *Observations of the Spots on the Sun from November 9, 1853 to March 24, 1861 Made at Redhill.* London, UK: Williams and Norgate, 1863.

[81] H. B. Snodgrass, "Separation of Large-Scale Photospheric Doppler Patterns," *Solar Physics*, vol. 94, pp. 13–31, 1984.

[82] R. W. Komm, R. F. Howard, and J. W. Harvey, "Rotation Rates of Small Magnetic Features from Two- and One-Dimensional Cross-Correlation Analyses," *Solar Physics*, vol. 145, pp. 1–10, 1993.

[83] A. R. Choudhuri, M. Schüssler, and M. Dikpati, "The Solar Dynamo With Meridional Circulation," *Astronomy and Astrophysics*, vol. 303, pp. L29–L32, 1995.

[84] D. H. Hathaway, D. Nandy, R. M. Wilson, and E. J. Reichmann, "Evidence that a Deep Meridional Flow Sets the Sunspot Cycle Period," *Astrophysical Journal*, vol. 589, pp. 665–670, 2003.

[85] D. Nandy, "Meridional Circulation and the Solar Magnetic Cycle," in *Proceedings of the SOHO 14/GONG 2004 Workshop*, New Haven, Connecticut, USA, July 2004, pp. 241–250.

[86] D. H. Hathaway, J. G. Beck, S. Han, and J. Raymond, "Radial Flows in Supergranules," *Solar Physics*, vol. 205, pp. 25–38, 2002.

[87] T. L. Duvall-Jr and L. Gizon, "Time-Distance Helioseismology with f Modes as a Method for Measurement of Near-Surface Flows," *Solar Physics*, vol. 192, pp. 177–191, 2000.

[88] S. Chandrasekhar, *Hydrodynamic and Hydromagnetic Stability.* New York, USA: Dover, 1961.

[89] E. O. Brigham, *Fast Fourier transform and its Applications.* New Jersey, USA: Prentice Hall, 1988.

[90] P. A. Gilman and P. V. Foukal, "Angular Velocity Gradients in the Solar Convection Zone," *Astrophysical Journal*, vol. 229, pp. 1179–1185, 1979.

[91] P. V. Foukal and R. Jokipii, "On the Rotation of Gas and Magnetic Fields at the Solar Photosphere," *Astrophysical Journal Letters*, vol. 199, pp. L71–L73, 1975.

[92] P. V. Foukal, "Supergranulation and the Dynamics of Gas and Magnetic Field Below the Solar Photosphere," *Astrophysical Journal*, vol. 218, pp. 539–546, 1977.

[93] H. B. Snodgrass and R. K. Ulrich, "Rotation of Doppler Features in the Solar Photosphere," *Astrophysical Journal*, vol. 351, pp. 309–316, 1990.

[94] J. G. Beck and J. Schou, "Supergranulation Rotation," *Solar Physics*, vol. 193, pp. 333–343, 2000.

[95] T. L. Duvall-Jr, S. M. Jeffferies, J. W. Harvey, and M. A. Pomerantz, "Time-Distance Helioseismology," *Nature*, vol. 362, pp. 430–432, 1993.

[96] D. H. Hathaway, P. E. Williams, and M. Cuntz, "Supergranule Superrotation Identified as a Projection Effect," *Astrophysical Journal*, vol. 644, pp. 598–602, 2006.

[97] R. P. Lin, B. R. Dennis, G. J. Hurford, D. M. Smith, A. Zehnder, P. R. Harvey, D. W. Curtis, D. Pankow, P. Turin, M. Bester, A. Csillaghy, M. Lewis, N. Madden, H. F. van Beek, M. Appleby, T. Raudorf, J. McTiernan, R. Ramaty, E. Schmahl, R. Schwartz, S. Krucker, R. Abiad, T. Quinn, P. Berg, M. Hashii, R. Sterling, R. Jackson, R. Pratt, R. D. Campbell, D. Malone, D. Landis, C. P. Barrington-Leigh, S. Slassi-Sennou, C. Cork, D. Clark, D. Amato, L. Orwig, R. Boyle, I. S. Banks, K. Shirey, A. K. Tolbert, D. Zarro, F. Snow, K. Thomsen, R. Henneck,

A. Mchedlishvili, P. Ming, M. Fivian, J. Jordan, R. Wanner, J. Crubb, J. Preble, M. Matranga, A. Benz, H. Hudson, R. C. Canfield, G. D. Holman, C. Crannell, T. Kosugi, A. G. Emslie, N. Vilmer, J. C. Brown, C. Johns-Krull, M. Aschwanden, T. Metcalf, and A. Conway, "The Reuven Ramaty High-Energy Solar Spectroscopic Imager (RHESSI)," *Solar Physics*, vol. 210, pp. 3–32, 2002.

[98] G. W. Platzman, "The Rossby Wave," *Quarterly Journal of the Royal Meteorological Society*, vol. 94, pp. 225–248, 1968.

[99] R. E. Dickinson, "Rossby Waves - Long-Period Oscillations of Oceans and Atmospheres," *Annual Review of Fluid Mechanics*, vol. 10, pp. 159–195, 1978.

[100] P. A. Gilman, "A Rossby-Wave Dynamo for the Sun, I," *Solar Physics*, vol. 8, pp. 316–330, 1969.

[101] ——, "A Rossby-Wave Dynamo for the Sun, II," *Solar Physics*, vol. 9, pp. 3–18, 1969.

[102] S. Kato and Y. Nakagawa, "The Solar Differential Rotation and 'Rossby-Type' Waves," *Solar Physics*, vol. 10, pp. 476–493, 1969.

[103] E. Tikhomolov, "Forcing of Differential Rotation and Rossby Waves at the Interface between the Convectively Stable and Unstable Layers," *Astrophysical Journal*, vol. 499, pp. 905–913, 1998.

[104] C. L. Wolff, "Linear r-Mode Oscillations in a Differentially Rotating Star," *Astrophysical Journal*, vol. 502, pp. 961–967, 1998.

[105] J. Papaloizou and J. E. Pringle, "Non-radial Oscillations of Rotating Stars and Their Relevance to the Short-Period Oscillations of Cataclysmic Variables," *MNRAS*, vol. 182, pp. 423–442, 1978.

[106] N. Schaeffer and P. Cardin, "Rossby-wave Turbulence in a Rapidly Rotating Sphere," *Nonlinear Processes in Geophysics*, vol. 12, pp. 947–953, 2005.

[107] D. B. Chelton and M. G. Schlax, "Global Observations of Oceanic Rossby Waves," *Science*, vol. 272, pp. 234–238, 1996.

[108] P. Cipollini, D. Cromwell, P. G. Challenor, and S. Raffaglio, "Rossby Waves Detected in Global Ocean Color Data," *Geophysical Research Letters*, vol. 28, pp. 323–326, 2001.

[109] E. R. Kursinski, G. A. Hajj, W. I. Bertiger, S. S. Leroy, T. K. Meehan, L. J. Romans, J. T. Schofield, D. J. McCleese, W. G. Melbourne, C. L. Thornton, T. P. Yunck, J. R. Eyre, and R. N. Nagatani, "Initial Results of Radio Occultation Observations of Earth's Atmosphere Using the Global Positioning System," *Science*, vol. 271, pp. 1107–1110, 1996.

[110] P. E. Williams, D. H. Hathaway, and M. Cuntz, "Solar Rossby Wave "Hills" Identified as Supergranules," *Astrophysical Journal Letters*, vol. 662, pp. L135–L138, 2007.

[111] J. S. Turner, *Buoyancy Effects in Fluids*. Cambridge, UK: Cambridge University Press, 1973.

[112] T. D. Kaladze and D. J. Wu, "Nonlinear Rossby Wave Dynamics in the Solar Photosphere," *Astrophysical Journal Letters*, vol. 638, pp. L49–L50, 2006.

[113] M. D. Fivian, H. S. Hudson, and R. P. Lin, *The Dynamic Sun: Challenges for Theory and Obsverations (CD-ROM 4.1)*, D. D. et al., ED. Noordwijk, Netherlands: ESA SP-600, 2005.

[114] J. Christensen-Dalsgaard, J. Schou, and M. J. Thompson, "A Comparison of Methods for Inverting Helioseismic Data," *Monthly Notices of the Royal Astronomical Society*, vol. 242, pp. 353–369, 1990.

[115] M. J. Thompson, J. Christensen-Dalsgaard, M. S. Miesch, and J. Toomre, "The Internal Rotation of the Sun," *Annual Review of Astronomy and Astrophysics*, vol. 41, pp. 599–643, 2003.

[116] T. M. Brown and P. A. Gilman, "Techniques for Detecting Giant Cells Using Spatially Resolved Solar Velocity Data," *Astrophysical Journal*, vol. 286, pp. 804–809, 1984.

[117] W. H. Chiang, L. D. Petro, and P. V. Foukal, "A Photometric Search for Solar Giant Convection Cells," *Solar Physics*, vol. 110, pp. 129–138, 1987.

[118] L. H. Strous and G. W. Simon, "62 Days Around the Sun: A Search for Supergranular Evolution and Giant Cells," *ASP Conference Series: Synoptic Solar Physics*, vol. 140, pp. 161–169, 1998.

[119] R. Kitai, H. Kurokawa, Y. Funakoshi, K. Ishiura, G. Kimura, and T. Shinkawa, "An Observational Search for Giant Cells in the Sun," *Advanced Space Research*, vol. 24, pp. 237–239, 1999.

[120] R. K. Ulrich, "Very Long Lived Wave Patterns Detected in the Solar Surface Velocity Signal," *Astrophysical Journal*, vol. 560, pp. 466–475, 2001.

[121] P. E. Williams, D. H. Hathaway, and M. Cuntz, "Advection of Supergranules by Giant Cells: A Numerical Experiment," *Astrophysical Journal Letters*, in preparation, 2008.

BIOGRAPHICAL STATEMENT

Peter E. Williams was born in Swansea, Wales, United Kingdom in 1969. He worked in the field of computer-operations for Clarks International between 1989-1994 before beginning his move into higher education. In 1999, he received his MSci. Astrophysics degree with first class honours from Queen Mary and Westfield College, University of London where his thesis topic of study was 'Circumstellar Outflows Around Carbon Stars', mentored by Dr. Peter G. Williams. In 2001, he moved to the United States and continued his education culminating in achieving his M.S. in Physics from The University of Tennessee Space Institute in 2003 with research work culminating in the thesis, 'Monte Carlo Simulations and Analysis of Single-Molecule Detection and Imaging' under the supervision of Dr. Lloyd Davis. In 2004, he moved to The University of Texas at Arlington (UTA). Here he worked in collaboration with Dr. David Hathaway at NASA Marshall Space Flight Center in Huntsville, Alabama, and his advisor, Dr. Manfred Cuntz at UTA on research presented in this dissertation for his PhD. in Applied Physics.